UCTEA Turkish Chamber of Civil Engineers

Teknik Dergi

Technical Journal

Volume 31 Issue 6 November 2020

TEKNİK DERGİ PUBLICATION PRINCIPLES

Teknik Dergi is a scientific and technical journal indexed by the Science Citation Index Expanded. Annually six issues are published, three in Turkish in the months of January, May and September, three in English in March, July and November. Its main principles of publication are summarized below:

1. Articles reporting original scientific research and those reflecting interesting engineering applications are accepted for publication. To be classified as original, the work should either produce new scientific knowledge or add a genuinely new dimension to the existing knowledge or develop a totally new method or substantially improve an existing method.
2. Articles reporting preliminary results of scientific studies and those which do not qualify as full articles but provide useful information for the reader can be considered for publication as technical notes.
3. Discussions received from the readers of the published articles within three months from publication are reviewed by the Editorial Board and then published together with the closing remarks of the author.
4. Manuscripts submitted for publication are evaluated by two or three reviewers unknown to the authors. In the light of their reports, final decision to accept or decline is taken by the Editorial Board. General policy of the Board is to get the insufficient manuscripts improved in line with the reviewers' proposals. Articles that fail to reach the desired level are declined. Reasons behind decisions are not declared.
5. A signed statement is taken from the authors, declaring that the article has not been published as a "journal article or book chapter". In case the Editorial Board is in the opinion that the article has already been published elsewhere with minor changes or suspects plagiarism or a similar violation of ethics, then not only that article, but none of the articles of the same authors are published.
6. Papers reporting works presented as conference papers and developed further may be considered for publication. The conference it was presented to is given as a footnote in the first page.
7. Additionally, a document signed by all authors, transferring the copyright to UCTEA Chamber of Civil Engineers is submitted together with the manuscript.

UCTEA Turkish Chamber of Civil Engineers

Teknik Dergi

Technical Journal

Volume 31 Issue 6 November 2020

UCTEA *(TMMOB)*
Turkish Chamber of Civil Engineers *(İnşaat Mühendisleri Odası)*
Necatibey St. No: 57, Kızılay 06440 Ankara, Turkey
Tel: +90.312.294 30 00 - Faks: +90.312.294 30 88
E-mail: imo@imo.org.tr - www.imo.org.tr

Publisher *(Sahibi)*:
Taner YÜZGEÇ
On behalf of UCTEA Turkish Chamber of Civil Engineers

Administrative Officer *(Yazı İşleri Müdürü)*:
Özer AKKUŞ

Volume 31 - Issue 6 - November 2020 *(Cilt 31 - Sayı 6 - Kasım 2020)*

Published bi-monthly. Local periodical. *(İki ayda bir yayınlanır, yerel süreli yayın)*

Date of Print: 1 November 2020 *(Baskı Tarihi: 1 Kasım 2020)*

Number of copies: 1.000 *(1.000 adet basılmıştır)*

ISSN: 1300-3453

Printed by *(Baskı)*:
Yorum Basın Yayın Sanati Ltd. Şti.
Başkent Organize Sanayi Bölgesi Recep Tayyip Erdoğan Bulvarı No: 12
Malıköy - Sincan /Ankara - Tel: 0.312.395 21 12

UCTEA Turkish Chamber of Civil Engineers

Teknik Dergi

Teknik Dergi is indexed by
- Science Citation Index Expanded
- Scopus
- Journal Citation Reports / Science Edition
- Engineering Index
- Concrete Abstracts (American Concrete Institute)
- National Technical Information Service (US NTIS)
- CITIS
- Ulrich's International Periodical's Directory
- TÜBİTAK / ULAKBİM

Teknik Dergi is a peer reviewed open access periodical publishing papers of original research and interesting practice cases. It addresses both the research community and the practicing engineers.

Reviewers:

This list is renewed each year and includes reviewers who served in the last two years of publication.

Ayda Şafak AĞAR
ÖZBEK
Perviz AHMEDZADE
Ragıp AKBAŞ
Sami Oğuzhan AKBAŞ
Rıfat AKBIYIKLI
Özge AKBOĞA KALE
Burcu AKÇAY
ALDANMAZ
Cihan Taylan AKDAĞ
Cem AKGÜNER
Adem AKPINAR
Muhammet Vefa
AKPINAR
Atakan AKSOY
Hafzullah AKSOY
Güzin AKYILDIZ
ALÇURA
Zuhal AKYÜREK
Fatih ALEMDAR
Pelin ALPKÖKİN
Sinan ALTIN
Selim ALTUN
Adlen ALTUNBAŞ
Ahmet Can
ALTUNIŞIK
Egemen ARAS
Fuat ARAS
Davit ARDITI
Ergin ARIOĞLU
Deniz ARTAN İLTER
Ali Osman ATAHAN
Hakan Nuri ATAHAN
Shady ATTIA
Abdullah AVEY
İsmail AYDIN
Mustafa Tamer AYVAZ
Ela BABALIK
Can Elmar BALAS
Lale BALAS
Selim BARADAN
Türkay BARAN
Bekir Oğuz BARTIN
Cemal BAŞARAN
Zeynep BAŞARAN
BUNDUR
Özgür BAŞKAN
Cüneyt BAYKAL
İdris
BEDİRHANOĞLU
Mehmet BERİLGEN
Saadet Arzu
BERİLGEN
Niyazi Özgür BEZGİN
Selçuk BİLDİK
Senem BİLİR
MAHÇİÇEK
Barış BİNİCİ
Ahmet BİRİNCİ
İlknur BOZBEY
Zafer BOZKUŞ
Burcu BURAK BAKIR
Halil İbrahim
BURGAN
Yusuf CALAYIR
Erdem CANBAY
Zekai CELEP
Cihan CENGİZ
Halim CEYLAN
Ömer CİVALEK
Mustafa CÖMERT
Ali Fırat ÇABALAR
Barlas Özden
ÇAĞLAYAN
Özgür ÇAKIR
Melih ÇALAMAK
Gülben ÇALIŞ
Erkan ÇELEBİ
Kutay ÇELEBİOĞLU
Ahmet Ozan ÇELİK
Oğuz Cem ÇELİK
Osman Nuri ÇELİK
Semet ÇELİK
Hilmi Berk
ÇELİKOĞLU
Kemal Önder ÇETİN
Mecit ÇETİN
Reha ÇETİNKAYA
Gökhan ÇEVİKBİLEN
Mesut ÇİMEN
Safiye Feyza
ÇİNİCİOĞLU
Erdal ÇOKÇA
Şevket ÇOKGÖR
Atilla DAMCI
Yakup DARAMA
Kutlu DARILMAZ
Cem DEMİR
Uğur DEMİR
Ender DEMİREL
Mehmet Cüneyd
DEMİREL
Fatih DİKBAŞ
Seyyit Ümit DİKMEN
İrem DİKMEN TOKER
Ali Ersin DİNÇER
Ahmet Anıl DİNDAR
Emrah DOĞAN
Nurhan ECEMİŞ
ZEREN
Özgür EKİNCİOĞLU
Alper ELÇİ
Şebnem ELÇİ
Murat Altuğ ERBERİK
Saffet ERDOĞAN
Esin ERGEN
PEHLEVAN
Ayşen ERGİN
Gökmen ERGÜN
Ebru ERİŞ
Esra Ece ESELLER
BAYAT
Tuğba ESKİŞAR
TEFÇİ
Burak FELEKOĞLU
Okan FISTIKOĞLU
Antonio FORMISANO
Nuray GEDİK
Abdullah GEDİKLİ
Ergun GEDİZLİOĞLU
Mohammad Ali
GHORBANİ
Konuralp GİRGİN
Zehra Canan GİRGİN
Ilgın GÖKAŞAR
Çağlar GÖKSU
Burcu GÜLDÜR
ERKAL
Fazlı Erol GÜLER
Hakan GÜLER
Ilgın GÜLER
Zeynep GÜLERCE
Taylan GÜNAY
Necmettin GÜNDÜZ
Abdurrahman GÜNER
Samet GÜNER
Ülker GÜNER
BACANLI
Mehmet Şükrü GÜNEY
Tuba GÜRBÜZ
BÜYÜKKAYIKÇI
Gürkan Emre
GÜRCANLI
Aslı Pelin GÜRGÜN
İpek GÜRSEL DİNO
Gürşans GÜVEN IŞIN
Soner HALDENBİLEN
Murat HAMDERİ
Ufuk HANCILAR
Ingo A. HANSEN
Abdul HAYIR
Nejan HUVAJ
SARIHAN
Metin HÜSEM
Zeynep IŞIK
Sabriye Banu İKİZLER
Eren İNCİ
Pınar İNCİ KOÇAK
Erdal İRTEM
Nihat KABAY
Sedat KABDAŞLI
Volkan KAHYA
Mehmet Rifat
KAHYAOĞLU
Volkan KALPAKÇI
Alper KANYILMAZ
Murat KARACASU
Tanay KARADEMİR
Erhan KARAESMEN
Ali KARAİPEKLİ
Himmet KARAMAN
Mustafa KARAŞAHİN
Zülküf KAYA
İlker KAZAZ
Cevza Melek
KAZEZYILMAZ
ALHAN
Mustafa Kubilay
KELEŞOĞLU
Elçin KENTEL
Mustafa Erol KESKİN
Havvanur KILIÇ
İsmail Emrah KILIÇ
Sami And KILIÇ
Fahriye KILINÇKALE
Ufuk KIRBAŞ
Veysel Şadan Özgür
KIRCA
Gökhan KİRKİL
Niyazi Uğur KOÇKAL
Önder KOÇYİĞİT
Baha Vural KÖK
Mete KÖKEN
Fuat KÖKSAL
Ali Ümran
KÖMÜŞÇÜ
Şerife Yurdagül
KUMCU
Akif KUTLU
Semih
KÜÇÜKARSLAN
Abdullah KÜRKÇÜ
Hilmi LUŞ
Kasım MERMERTAŞ
Mehmet Murat
MONKUL
Yetiş Şazi MURAT
Elif OĞUZ
Didem OKTAY
Volkan OKUR
Mehmet Hakkı
OMURTAG
Sema ONURLU
Engin ORAKDÖĞEN
Şeref ORUÇ
Okan ÖNAL
Akın ÖNALP
Halil ÖNDER
Aybike ÖNGEL
Bihrat ÖNÖZ
Ali Hakan ÖREN
Bergüzar ÖZBAHÇECİ
Ceyhun ÖZÇELİK
İlker ÖZDEMİR
Murat ÖZEN
Pelin ÖZENER
Abdullah Tolga ÖZER
Eren Arman
ÖZGÜVEN
Hakkı Oral ÖZHAN
Yener ÖZKAN
M. Hulusi ÖZKUL
Zeynep Huri ÖZKUL
BİRGÖREN
Beliz ÖZORHON
ORAKÇAL
Sadık ÖZTOPRAK
Turan ÖZTURAN
Baki ÖZTÜRK
Hasan Tahsin ÖZTÜRK
Mustafa ÖZUYSAL
Tolga Yılmaz
ÖZÜDOĞRU
Polat ÖZYİĞİT
Gülizar ÖZYURT
TARAKÇIOĞLU
Nilüfer ÖZYURT
ZİHNİOĞLU
Onur PEKCAN
Bekir Yılmaz
PEKMEZCİ
Cengiz POLAT
Şamil Şeref POLAT
Gül POLAT TATAR
Selim PUL
Selçuk SAATÇİ
Selman SAĞLAM
Mehmet SALTAN
Altuğ SAYGILI
Neslihan SEÇKİN
Serdar SELAMET
Alper SEZER
Faiz Uddin Ahmed
SHAİKH
Osman SİVRİKAYA
Serdar SOYÖZ
Aleksandar
STEVANOVİC
Ayşe Filiz SUNAR
Erol ŞADOĞLU
Remzi ŞAHİN
Yuşa ŞAHİN
Mustafa ŞAHMARAN
Nermin ŞARLAK
Burak ŞENGÖZ
Aynur ŞENSOY
ŞORMAN
Ali Arda ŞORMAN
Ali Ünal ŞORMAN
Özcan TAN
Ali Hamza
TANRIKULU
Kürşat TANRIÖVEN
Serhan TANYEL
Taha TAŞKIRAN
Gökmen TAYFUR
İlker TEKİN
Beytullah TEMEL
Berrak TEYMUR
H. Onur TEZCAN
Mesut TIĞDEMİR
Şahnaz TİĞREK
Vedat TOĞAN
Nabi Kartal TOKER
Nuray TOKYAY
Ali TOPAL
Cem TOPKAYA
Selçuk TOPRAK
Ahmet TORTUM
Gökçe TÖNÜK
Nursu TUNALIOĞLU
Kağan TUNCAY
Eda TURAN
Gürsoy TURAN
Kaan TÜRKER
Cüneyt TÜZÜN
Eren UÇKAN
Latif Onur UĞUR
Mehmet Fevzi
UĞURYOL
Berna UNUTMAZ
Volkan Emre UZ
Deniz ÜLGEN
Aslı ÜLKE KESKİN
Cüneyt VATANSEVER
Syed Tanvir WASTI
Nazmiye YAHNİOĞLU
Ahmet YAKUT
Cem YALÇIN
Aslı YALÇIN
DAYIOOĞLU
İsmail Özgür YAMAN
A. Melih YANMAZ
Mert Yücel YARDIMCI
Ufuk YAZGAN
Anıl YAZICI
Halit YAZICI
Kasım YENİGÜN
İrem Zeynep
YILDIRIM
Mehmet
YILDIRIMOĞLU
Osman YILDIZ
Çetin YILMAZ
Fatih YILMAZ
Koray Kamil YILMAZ
M. Tuğrul YILMAZ
Mehmet YILMAZ
Murat YILMAZ
Veysel YILMAZ
Yüksel YILMAZ
Fatih YONAR
Recep YURTAL
İsmail YÜCEL
Ercan YÜKSEL
Yeliz YÜKSELEN
AKSOY
Nabi YÜZER
Ahmet Şahin
ZAİMOĞLU

UCTEA Turkish Chamber of Civil Engineers

Teknik Dergi

Volume: 31 Issue: 6 November 2020

CONTENTS

Teknik Dergi, 2020 10291-10313, Paper 591

Lightweight Cellular Hollow Concrete Blocks Containing Volcanic Tuff Powder, Expanded Clay and Diatomite for Non-Load Bearing Walls

Lütfullah GÜNDÜZ[1]
Şevket Onur KALKAN[2]

ABSTRACT

Lightweight cellular hollow concrete (LCHC) block is a type of masonry unit manufactured by precast technique. LCHC blocks are produced by the mixing of Portland cement, volcanic tuff, expanded clay and diatomite for building applications. LCHC blocks are lightweight, and the frequent cellular holes provide excellent thermal and acoustic performance, fire resistance and resistance to harsh environmental conditions. In this research work, LCHC blocks with 28 different mix proportions were cast into a mould with vibro-compacting, de-moulded immediately and transferred to a storage area for curing up to 120 days in standard air condition at room temperature. The blocks were designed with 21 cellular spaces of 10 mm width. For each mixture, twenty four block specimens were prepared and tested in the air dry condition for compressive strength and water absorption in accordance with BS 1881: Part 116. This paper initially examines how volcanic tuff powder affects the characteristics of lightweight concrete masonry mixtures and investigates the use of quaternary blends containing volcanic tuff, expanded clay, diatomite and Portland cement to produce LCHC blocks for partitioning walls.

Keywords: Lightweight concrete, volcanic tuff, expanded clay, diatomite, masonry block.

1. INTRODUCTION

The production of lightweight concrete masonry units transformed from a hand cast process to a highly automated one during the past 100 years. Single moulds compacted by hand gave way to ganged moulds that travel on assembly lines in high-tech manufacturing facilities. These changes have also led to excellent quality control and uniformity of units [1]. Concrete masonry units are manufactured with very dry, stiff concrete mixtures. The “no-slump” or

Note:
- This paper has been received on May 22, 2018 and accepted for publication by the Editorial Board on July 17, 2019.
- Discussions on this paper will be accepted by January 31, 2021.
- https://dx.doi.org/10.18400/tekderg.426034

1 İzmir Kâtip Çelebi University, Department of Civil Engineering, İzmir, Turkey - lutfullah.gunduz@ikc.edu.tr - https://orcid.org/0000-0003-2487-467X

2 İzmir Kâtip Çelebi University, Department of Civil Engineering, İzmir, Turkey - sevketonur.kalkan@ikc.edu.tr - https://orcid.org/0000-0003-0250-8134

"low-slump" material is placed into moulds, vibrated and compacted, and demoulded quickly. The demoulded units are stiff enough to hold their shape as they enter the curing chamber. Afterwards, they are palletized and readied for shipping [1]. They could be manufactured, adding to local economies and meeting sustainability criteria.

Lightweight concrete masonry blocks are primarily used as building materials in the construction of walls. Concrete blocks are one of several precast concrete products used in construction. Most concrete blocks have one or more hollow cavities, and their sides may be cast smooth or with a design. In use, concrete blocks are stacked one at a time and jointed with fresh cementitious mortar to form the desired length and height of the wall.

The concrete mixtures commonly used to make normal weight concrete masonry blocks is a mixture of Portland cement, water, sand, and gravel. This produces a light grey block with a fine surface texture and a sufficiently high compressive strength. This type of blocks is generally used for building load-bearing walls and partitions. Typical mass of this type of concrete block ranges from 16 kg to 27 kg. In general, the concrete mixture used for blocks has a higher percentage of sand and a lower percentage of gravel and water than the concrete mixtures used for general construction purposes. If lightweight aggregates are used instead of normal weight sand and gravel, the resulting block is commonly called a lightweight concrete masonry block. This produces more porous and lighter blocks with a medium-to-coarse surface texture, good strength, good sound-deadening properties, and a higher thermal insulating value than a normal weight concrete block. LCHC blocks made of different lightweight aggregates, cement and water are used in construction of non-load bearing infill walls and slabs. Lightweight blocks can be manufactured with densities ranging from 400 kg/m^3 to 1100 kg/m^3 effecting an average reduction in dead load of 40 % to 50 % as compared to those of buildings with conventional concrete walls [2, 3, 4]. A typical lightweight concrete masonry block has a mass of 5 kg to 14 kg depending on the mineralogical composition, the particle shape and grading of the aggregate.

In general, units with lower density will not only reduce the dead load of a structure, but will also have better thermal insulating properties and provide increased mason productivity during installation. These factors can result in significant overall cost savings. LCHC blocks allow increased productivity in production, delivery, handling, and installation. The fire resistance rating of a lightweight concrete masonry unit depends on its equivalent thickness and the types of aggregate used in its manufacture.

Aggregate size and gradation are the most important factors when selecting aggregate in lightweight masonry mixtures. Aggregate particle sizes range from coarse-sized granulates to fine-sized powder [6]. As a general rule, the largest aggregate should be no greater in size than one-third the depth of the slab, or one-fifth the smallest dimension of the form. Since the mortar samples to be produced are poured into the moulds and the mould openings are 22 mm wide, maximum fine aggregate grain size is selected as 1 mm. Well-graded aggregates may be used to reduce the amount of cement paste required and thus, decrease the amount of shrinkage that could occur.

The volumetric majority of the low slump masonry concrete consists of lightweight aggregates. It is a basic objective that the cement paste coats and binds together the aggregate particles. The composition, shape, porosity, size and type of the aggregate all have significant effect on the workability, durability, strength, unit weight, and shrinkage of the lightweight

concrete. Aggregate can also influence the texture and appearance of the cast surface, which is an especially important consideration in concrete masonry block making mixes.

Lightweight aggregates have maximum dry loose bulk densities of about 880 kg/m^3 for the coarse fractions and 1040 kg/m^3 for all-in aggregates [7]. Lightweight aggregates are also classified as natural and artificial depending on the final source they are obtained. The main natural lightweight aggregates are diatomite, pumice, scoria, volcanic slug, and volcanic tuff. Except for diatomite, all are volcanic in origin. Pumice and scoria are more widely used for hollow and solid concrete block production in Turkey [8,9]. However, using the expanded clay in masonry block productions is a relatively new experience in Turkey.

Due to the low aggregate strength characterizations, diatomite aggregates alone are not generally preferred for use in production of lightweight masonry blocks. However, diatomite aggregates could be used with strength enhancer materials to ensure a sufficient strength requirement for lightweight masonry blocks. Volcanic tuff powders are one of the well-known strength enhancer natural materials due to their pozzolanic properties. Also expanded clay aggregates are used in concrete masonry blocks to improve the strength.

Although many lightweight aggregates are suitable for use in lightweight masonry blocks, inclusion of volcanic tuff powder as a strength enhancer material in the mixture does not appear as a widespread practice in literature. In this respect, a research work was carried out to optimize the lightweight masonry blocks according to the related standards by using volcanic tuff as a strength enhancer material. This research work presents the technical results of a comprehensive experimental study on optimizing the lightweight masonry blocks for non-load bearing walls.

2. EXPERIMENTAL STUDY

2.1. Experimental Scope

The experimental work was carried out in order to determine the suitability for use of quaternary blends containing volcanic tuff, expanded clay aggregate, diatomite and cement to produce LCHC blocks for non-load bearing walls and partitions. Initially, the aim of the work was to evaluate the use of volcanic tuff and expanded clay aggregate as strength enhancers to improve the lightweight concrete properties. A series of comprehensive tests were carried out to analyse the effects of volcanic tuff and expanded clay aggregate on the constituent material composition, unit weight, compressive strength and water absorption properties. The effects of use of fine and coarse diatomite aggregates in production of lightweight masonry blocks were also determined.

2.2. Materials Used in the Research

The lightweight concrete masonry hollow blocks with dimensions of 185 mm height, 390 mm length and 190 mm width, in general use in Turkey, were used throughout the experimental work. The web and shell thicknesses of the hollow lightweight units were 22 mm. In total, each block contained 21 cellular spaces of 10 mm width. The model of masonry unit is shown in Fig. 1

Portland cement (CEM I 42.5) which is comparable to ASTM Type 1 (42.5 N/mm^2) was used throughout this research. The chemical composition and physical properties of the cement used in this research are given in Tables 1 and 2.

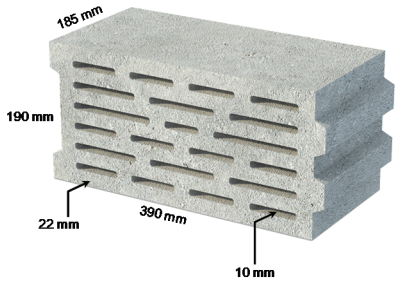

Figure 1 - The model of masonry unit

Table 1 - Chemical compositions of CEM I, VTP, ECA, FDA and CDA (mass%)

Major element	CEM I	VTP	ECA	FDA and CDA
SiO_2	20.92	61.44	51.60	68.74
Al_2O_3	5.18	12.48	14.80	8.94
Fe_2O_3	3.87	4.34	11.75	14.23
CaO	62.44	5.10	8.40	0.69
Na_2O	0.19	1.65	1.13	0.34
K_2O	0.78	1.38	1.24	1.58
MgO	2.45	6.40	5.60	0.61
LOI	1.51	1.80	3.20	7.80

CEM I : Portland cement TS EN 197-1
VTP : volcanic tuff powder
ECA : expanded clay aggregate
FDA : fine diatomite aggregate
CDA : coarse diatomite aggregate

Table 2 - Mechanical and physical properties of CEM I

Specific gravity	3.10
Blaine specific surface (m^2/kg)	324.5
Initial setting time (min)	250
Final setting time (min)	360
Volume expansion (mm/m)	0.87
Compressive strength (MPa)	
2 days	14.7
7 days	26.9
14 days	34.7
28 days	43.0

As strength enhancer materials, two different aggregate types namely volcanic tuff and expanded clay aggregate were used. Volcanic tuff aggregate used in this experimental study was obtained from the location of ignimbrite Mining Quarry in Aksaray Region, Central Anatolia. Volcanic tuff obtained from the quarry was only crushed by a primer crusher and then screened to obtain the 0/1 mm filler fraction (VTP) The tuff was found to be composed of rounded particles when optically analysed using a microscope. Because, it was observed in the microscope analysis that rounded shape tuff particles have an ability to do a well filling affect in the matrix structure. Optical microscopic analysis showed that the tuff contained well-rounded particles which enhance workability, filling effect, and, thus strength.

Natural pozzolans constitute a part of the lightweight aggregate group that could increase the strength and durability of concrete in the production of block making mixtures. Tuff aggregate in powder form is one of the well-known pozzolans used in concrete applications.

The expanded clay aggregates were obtained from the clay mining quarries at Kalecik Region in Ankara, Central Turkey. The clay aggregates obtained from the quarry were first crushed and then grounded into a powder form. Clay pellets were made with potable water without using any admixture in laboratory conditions. Then all pellets were expanded in a kiln at 1050 °C to produce expanded clay aggregate (ECA). After expanding, they were screened into 4/8 mm size fractions. Diatomite aggregates were obtained from the diatomite mining quarries at Kazan Region in Ankara, Central Turkey. Diatomite aggregates were used in their natural state (as mined), without any calcination. Similar to VTP, the diatomite aggregates were also first crushed by a primer crusher, and then screened into 0/4 mm and 4/8 mm size fractions as fine diatomite aggregate (FDA) and coarse diatomite aggregate (CDA), respectively. The chemical compositions of these materials are given in Table 1. Dry bulk density, water absorption and compressive strength values of VTP, ECA, FDA and CDA, given in Table 3, were determined according to the BS 812:P2 [10], BS 812:P110 [11], ASTM C127 [12] and ASTM C128 [13].

Table 3 - Physical properties of VTP, ECA, FDA and CDA

Material	Specific Gravity	Dry bulk density (kg/m^3)	Water Absorption (wt%)
VTP	2.21	1240	33.8
ECA	2.48	976	35.7
FDA	2.33	413	60.8
CDA	2.33	326	71.4

Tuff, a pyroclastic rock of consolidated volcanic ash origin, is sometimes called tufa or ashstone, particularly when used as construction material, although tufa also refers to a quite different rock. Rock that contains greater than 50 % tuff is considered tuffaceous [14, 15, 16, 17]. Its highly vesicular but compacted and consolidated structure gives it a higher strength.

The volcanic tuff aggregate in its natural form has been used to increase the compressive strength and decrease the density of masonry blocks. Initial and final setting times increase when the quantity of tuff increases, resulting in a slower compressive strength development.

The advantages of tuff include its highly porous structure, high surface area, and low density. It is available in different types, sizes, and colours, and can reduce the concrete self-weight. Similar to other pozzolanic materials, such as silica fume and fly ash, substitution with zeolite can improve the strength of concrete via the pozzolanic reaction with $Ca(OH)_2$. It can reduce the bleeding, segregation, and delamination of fresh concrete, facilitate pumping processes, decrease the permeability of hardened concrete, enhance durability (especially alkali-aggregate reactivity), increase concrete strength, and minimize the cracking in concrete caused by autogenous-shrinkage.

Expanded clays are made of clays that may expand up to 5–6 folds, by volume as a result of gas release when they are treated with heat. A hard sintered crust is formed on the outer surface, while quite light and highly durable aggregate with a porous clinker-like structure may be produced inside it [18]. Expanded clay aggregates are a new topic for Turkey and detailed studies on their production have begun recently [19]. Expanded clay aggregates are used in many different industries due to their useful technical features and numerous advantages when compared to many other industrial raw materials [19]. One of the materials that yield the greatest concrete compressive strength among lightweight aggregates is expanded clay aggregate. This gives it a significant position in the construction industry. Because LCHC reduces walls dead load comparing with conventional masonry elements, reductions up to 20 % in reinforcing steel weight may be gained while up to 50 % may be saved in heating–cooling expenses in buildings containing components made with expanded clay aggregates in Turkey [18, 20]. They have high porosity and low density. The bubbly nature of expanded clay aggregate is due to liberation of gases during calcination. They are typically brown and reddish in colour due to their high iron contents. The surface of some expanded clay aggregates may have a yellowish iridescent colour based on the pellet admixture materials.

Diatomite is a biochemical sedimentary white-or cream-colored, friable, porous rock mainly composed of the fossilized remains of unicellular fresh water plants known as diatoms. Diatoms are tiny plants that float near the ocean surface. Their skeletons are composed of silica, a very durable substance. Since diatom skeletons are highly porous, diatomite has extremely low density, and pure samples make excellent water filters. Chemically inert and having a rough texture and other unusual physical properties, it is suitable for many scientific and industrial purposes, including use as a filtering agent; building material; heat, cold, and sound insulator; catalyst carrier; filler absorbent; abrasive; and ingredient in pharmaceutical preparations [21, 22, 23].

2.3. Mix Design and Sample Preparation

In order to analyse the use of quaternary blends containing volcanic tuff, expanded clay aggregate, diatomite and cement to produce LCHC blocks for walls and partitions, initially 28 different mixture proportions (M1–M28) by mass and cement contents of 94.5, 121.5 and 162.5 kg/m^3 were adopted for the concrete mixture batches, respectively. Drying shrinkage and wetting expansion are major weaknesses in volcanic tuff powder based blocks. In low slump lightweight masonry hollow blocks, drying shrinkage cracking can be minimized by keeping the water/binder ratio as low as possible [2]. Hence, in the present study, 30 mm slump value was used as the limit for the dry consistency mixture.

Table 4 - Proportions of trial mixtures (% by apparent volume, av%)*

Mix	CEM I	VTP	ECA	FDA	CDA
M1	9.00	1.00	90.00	-	-
M2	9.00	3.00	88.00	-	-
M3	9.00	5.00	86.00	-	-
M4	7.00	-	15.00	39.00	39.00
M5	7.00	-	20.00	36.50	36.50
M6	7.00	-	25.00	34.00	34.00
M7	9.00	-	15.00	38.00	38.00
M8	9.00	-	20.00	35.50	35.50
M9	9.00	-	25.00	33.00	33.00
M10	12.00	-	15.00	36.50	36.50
M11	12.00	-	20.00	34.00	34.00
M12	12.00	-	25.00	31.50	31.50
M13	7.00	1.00	20.00	36.00	3600
M14	7.00	3.00	20.00	35.00	35.00
M15	7.00	5.00	20.00	34.00	34.00
M16	12.00	1.00	20.00	33.50	33.50
M17	12.00	3.00	20.00	32.50	32.50
M18	12.00	5.00	20.00	31.50	31.50
M19	7.00	3.00	15.00	22.50	52.50
M20	7.00	3.00	20.00	21.00	49.00
M21	7.00	3.00	25.00	19.50	45.50
M22	9.00	3.00	15.00	21.90	51.10
M23	9.00	3.00	20.00	20.40	47.60
M24	9.00	3.00	25.00	18.90	44.10
M25	12.00	3.00	15.00	21.00	49.00
M26	12.00	3.00	20.00	19.50	45.50
M27	12.00	3.00	25.00	18.00	42.00
M28	9.00	-	91.00	-	-

** Apparent volume is defined as the ratio mass to the dry particle density.*

The first three trial batches were undertaken to determine mean strength and unit mass values of concrete mixtures containing VTP and ECA aggregate. To this effect, basically the first three preliminary batches were designed with aggregate/cement (A/C) ratios of 7:1 to 7.5:1 by mass with 9 % CEM I content by volume in a range of 12.4–62.0 kg/m^3 VTP contents without any diatomite aggregates. These batches were used as the control mixtures throughout the research. In order to evaluate the density, water absorption and strength requirement for lightweight concrete design in masonry block production, the effect of diatomite aggregates as ingredients was also analysed by a series of trial batches. For this purpose, additional preliminary batches were designed with aggregate/cement ratios of 2.5:1

to 5.5:1 by mass in a range of 94.5–162.0 kg/m^3 CEM I contents using fine and coarse diatomite aggregates at different percentages by apparent volume. The mixtures proportions for trial batches are given in Table 4 in terms of dry masses of the ingredients. Concrete design methodology was constructed according to TS EN 771-3 standard. Information and results derived from these trial mixtures were used to produce main relationship; linking various parameters to both A/C ratio and cement content. Test results of these trial batches are given in Table 5. All trials were conducted using CEM I of local manufacture, complying with the requirements of ASTM Type I (42.5 N/mm^2) cement.

Table 5 - Physical characteristics of the 100 mm-cube specimens

Mix	Dry density (kg/m^3)	Compressive strength (N/mm^2)	Water absorption (% by weight)
M1	1114	3.82	17.23
M2	1119	4.53	16.82
M3	1125	5.36	15.37
M4	582	1.74	31.71
M5	615	1.80	30.40
M6	649	1.87	29.26
M7	604	2.29	26.97
M8	637	2.37	25.37
M9	670	2.46	23.12
M10	636	3.16	21.47
M11	669	3.27	21.58
M12	703	3.39	21.47
M13	625	2.09	29.86
M14	644	2.38	28.45
M15	663	2.67	26.29
M16	679	3.59	19.93
M17	698	3.92	19.02
M18	717	4.26	15.02
M19	596	2.22	28.04
M20	631	2.35	27.66
M21	665	2.47	25.69
M22	618	2.79	23.93
M23	653	2.94	23.28
M24	687	3.08	23.20
M25	651	3.69	20.49
M26	686	3.87	20.16
M27	720	4.05	18.52
M28	1111	3.66	17.85

BS 1881: Part 125 [24] was followed for mixing and sampling the fresh concrete in laboratory and BS 1881: Part 114 [25] was followed for measuring the density of hardened concrete. According to the preliminary trial batch results, the fines content for optimum plastic properties in the fresh concrete and the final mixture compositions for the concrete work were determined. Cube specimens of 100 mm size were used for testing the mixture strengths and the effectiveness of fines content in the preliminary trials. A cellular hollow block form conforming the specifications of BS 6073: Part 1 [26] standard was used for preparation of LCHC specimens. The ratio of solid area and the total solid volume of the hollow block form are the same (77.65 %) due to the blocks' being open sub-section type. The web and shell thicknesses of the block are 22 mm and the block dimensions are 195 mm in height, 390 mm in length and 190 mm in width. For each mixture, 24 block specimens were cast and compacted on a vibration machine. The specimens were then air cured at 22±3°C temperature and 50±5 % relative humidity up to 28 days until the time of testing. The samples were then tested in air dry condition for compressive strength in accordance with BS 6073: Part 1 [26].

3. RESULTS AND DISCUSSIONS

Tuff and diatomite have an ability of high water absorption due to their high porosity and particle size distribution, therefore, the experience of block making machine operator is of critical importance in controlling the water content of lightweight concrete during mixing, unless a sufficiently accurate automatic control system and procedure is available. Any variation in water content and effective water/binder ratio will result in variations in the rate of strength gain and final strength. On the other hand, due to their low water absorption capacity, expanded clay aggregates are more suitable as compared to tuff and diatomite aggregates for concrete mixing for block making.

3.1. The Effect of VTP as a Natural Pozzolan

Many recent studies have examined the feasibility of using volcanic tuff as lightweight aggregate, building stone, and pozzolans in cements and concretes [3, 4, 27, 28].

The natural pozzolan used in this study was obtained from the location of ignimbrite Mining Quarry in Aksaray Region, Central Turkey. It is a highly porous, lightweight, finely divided mineral material containing large quantities of amorphous SiO_2 and Al_2O_3. Although the bulk density of VTP as a natural aggregate is in the range of 850 – 1200 kg/m^3, the bulk density of fine grade VTP is in the range of 1200 – 1300 kg/m^3, which is a typical lightweight aggregate block density range and the relevant mineralogical properties. In practice, VTP is used in ratios from 1 % to 7 % by apparent volume of lightweight concrete mixtures as a strength enhancer material. However, more than 7 % of VTP by apparent volume in LCHC is known to reduce the compressive strength. Therefore, in this research work, the VTP content was set lower than 7 % by apparent volume. Table 6 gives the limits of VTP and lightweight aggregate contents for use in LCHC. It has been shown experimentally that lightweight concretes containing expanded clay aggregate and natural pozzolan have relatively higher sulphate resistance, higher strength and durability. On the other hand, addition of a large quantity of the natural pozzolan decreases the compressive strength of concrete; therefore, an optimum quantity is necessary to achieve the maximum compressive

strength. Finely grounded VTP is mostly used with another porous aggregate. The basic effect of finely grounded VTP on fresh concrete is to improve cohesion, which prevents segregation, enhances mould filling, compaction, eases demoulding and modifies the texture improving the finish of fine quality blocks.

Table 6 - Standard requirements for lightweight aggregates for masonry and structural concrete

BS 3797 requirements	Maximum Limits
Loss on ignition-masonry units	25 %
Reinforced and high durability concrete	10 %

The use of tuff as natural pozzolan in lightweight concrete can also reduce the expenses if early strength is not important. BS 6073:Part 1 [26] requires a minimum strength of 2.8 N/mm^2 at 28 days with no individual block strength lower than 80 % of that value.

A series of LCHC blocks were produced with different proportions of tuff powder, expanded clay aggregate, diatomite and cement. The results of a comprehensive experimental research work carried out are presented in Figures 2 – 9 and Table 7 showing the mean values of each mixture.

Concretes containing tuff powders are generally expected to exhibit less bleeding and segregation than plain concretes. This effect makes the use of tuff powder particularly valuable in concrete mixtures made with aggregates that are deficient in fines. The reduction in bleed water could be primarily due to the reduced water demand in powder tuff concretes.

Table 7 - Mixture proportions and physical properties of hollow blocks (mean values of 24 specimens for each mix)

Mix	A/C	CEM I (kg/m^3)	VTP (kg/m^3)	ECA (kg/m^3)	FDA (kg/m^3)	CDA (kg/m^3)	W/C	Dry block mass (kg)	Dry density of hollow block (kg/m^3)	Water absorption of hollow block (kg/m^3)	Compressive strength of hollow block (N/mm^2)
M1	7.3	121.5	12.4	878.40	-	-	3.97	11.86	865	161.94	2.96
M2	7.4	121.5	37.2	858.88	-	-	3.95	11.91	869	158.67	3.52
M3	7.4	121.5	62.0	839.36	-	-	3.91	11.98	874	145.63	4.16
M4	4.6	94.5	-	146.40	161.07	127.14	3.25	6.20	452	167.31	1.35
M5	4.9	94.5	-	195.20	150.75	118.99	3.21	6.55	478	167.43	1.40
M6	5.2	94.5	-	244.00	140.42	110.84	3.26	6.91	504	168.22	1.45
M7	3.5	121.5	-	146.40	156.94	123.88	2.08	6.43	469	156.14	1.78
M8	3.8	121.5	-	195.20	146.62	115.73	2.63	6.78	495	152.55	1.84
M9	4.0	121.5	-	244.00	136.29	107.58	2.68	7.13	520	144.22	1.91
M10	2.6	162.0	-	146.40	150.75	118.99	2.18	6.77	494	142.04	2.45
M11	2.8	162.0	-	195.20	140.42	110.84	2.13	7.12	519	147.17	2.54
M12	2.9	162.0	-	244.00	130.10	102.69	2.16	7.48	546	151.16	2.63

Table 7 - Mixture proportions and physical properties of hollow blocks (mean values of 24 specimens for each mix) (continue)

Mix	A/C	CEM I (kg/m³)	VTP (kg/m³)	ECA (kg/m³)	FDA (kg/m³)	CDA (kg/m³)	W/C	Dry block mass (kg)	Dry density of hollow block (kg/m³)	Water absorption of hollow block (kg/m³)	Compressive strength of hollow block (N/mm²)
M13	5.0	94.5	12.4	195.20	148.68	117.36	3.23	6.65	485	166.61	1.62
M14	5.2	94.5	37.2	195.20	144.55	114.10	3.35	6.86	500	162.53	1.85
M15	5.4	94.5	62.0	195.20	140.42	110.84	3.48	7.06	515	153.73	2.08
M16	2.8	162.0	12.4	195.20	138.36	109.21	2.03	7.23	527	137.25	2.79
M17	2.9	162.0	37.2	195.20	134.23	105.95	2.11	7.43	542	133.28	3.04
M18	3.0	162.0	62.0	195.20	130.10	102.69	2.18	7.63	557	107.07	3.31
M19	4.7	94.5	37.2	146.40	92.93	171.15	3.40	6.34	463	150.69	1.73
M20	5.1	94.5	37.2	195.20	86.73	159.74	3.39	6.72	490	155.47	1.82
M21	5.4	94.5	37.2	244.00	80.54	148.33	3.44	7.08	516	150.58	1.92
M22	3.6	121.5	37.2	146.40	90.45	166.59	2.72	6.58	480	140.75	2.17
M23	3.9	121.5	37.2	195.20	84.25	155.18	2.65	6.95	507	142.54	2.28
M24	4.1	121.5	37.2	244.00	78.06	143.77	2.67	7.31	533	147.45	2.39
M25	2.7	162.0	37.2	146.40	86.73	159.74	2.12	6.93	506	137.45	2.87
M26	2.8	162.0	37.2	195.20	80.54	148.33	2.06	7.30	533	139.73	3.01
M27	3.0	162.0	37.2	244.00	74.34	136.92	2.07	7.66	559	132.39	3.15
M28	7.3	121.5	-	886.16	-	-	4.02	11.83	863	167.45	2.84

3.2. Compressive Strength and LCHC Unit Density

Filling and partitioning, non-load bearing walls seem to be the main building domain of application of lightweight concrete masonry units made of LCHC. Therefore, lightness, material integrity, adequate durability, good thermal and acoustic insulation ability, cost and sustainability, are some expected material properties [29]. LCHC blocks are a non-structural element and the blocks for non-load bearing applications. However, it is important that this type of masonry unit presents a certain compressive strength. For instance, it has to be able to support the weight of the overlying portion of the wall. Additionally, an adequate compressive strength also indicates that the concrete masonry unit presents an acceptable material integrity and therefore, it can be shipped, stored and applied in the building site [29]. BS EN 771-3:2011 sets the range for the compressive strengths of concrete masonry units (with dense and/or lightweight aggregates) from 2.9 N/mm^2 to 10.4 N/mm^2 [30]. It is well-known that, in general, strength increases with increasing un density. On the other hand, regardless of unit density, all non-load bearing concrete masonry units meeting the physical properties required by BS 6073: Part 1 [26] are required to have a minimum average compressive strength of 2.8 N/mm^2 with no individual block lower than 80 % of that value, as noted in Section 3.1 above, for minimum building and service functionality. Concrete strength is affected by many factors, such as properties of constituent materials, water/cement ratio, coarse/fine aggregate ratio, age of concrete, compaction of concrete, temperature, relative humidity and curing of concrete. In addition to these, some factors affecting the compressive strength of a lightweight masonry blocks are shape and dimension of the unit,

and aggregate types used in mixtures. Some of these parameters are evaluated for analysing the compressive strength properties of lightweight masonry blocks.

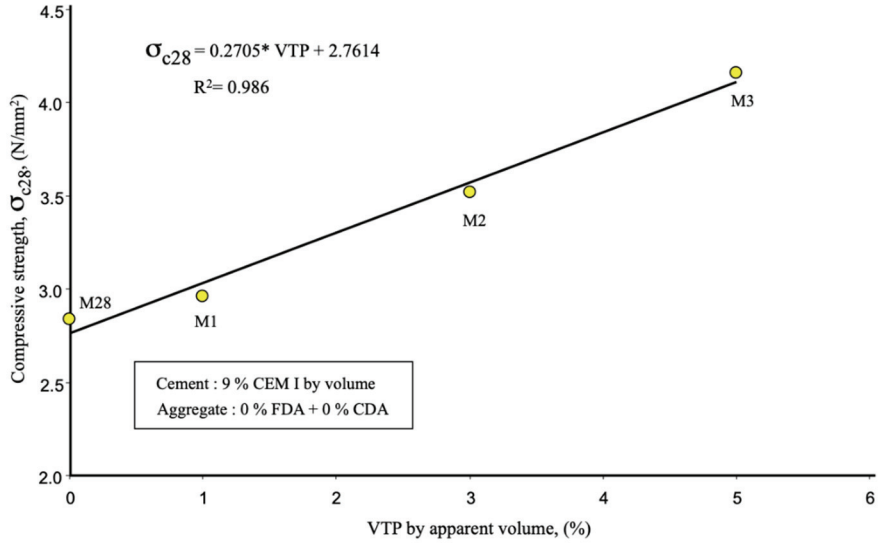

Figure 2 - The 28-day compressive strength versus VTP content of hollow blocks

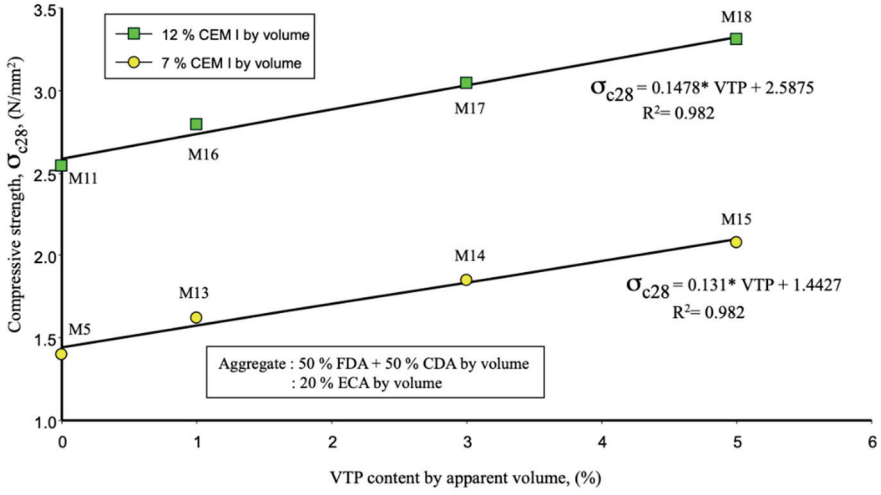

Figure 3 - The 28-day compressive strength versus VTP content of hollow blocks

Figure 2 shows the mean values of 28-day compressive strengths of LCHC blocks with a constant CEM I content of 9 % by volume with only VTP and ECA. As represented in Fig.

2, the compressive strength of LCHC blocks shows a linearly increasing trend with increasing VTP content. An increase of 2 % VTP content provides approximately 18.5 - 19.0 % strength increase in blocks containing ECA. However, the density of LCHC blocks increase by approximately 0.5 % due to the increase in VTP content, which could be considered negligible for lightweight masonry blocks. All the mixtures with 9 % CEM I content by volume produced with only VTP and ECA aggregates comply with the strength requirement of BS 6073.

Figure 3, shows the compressive strengths of LCHC blocks with 7 % and 12 % CEM I, constant 20 % VTP contents by apparent volume, and the remaining 73 % to 68 % by apparent volume being completed by adding a 50 % FDA + 50 % CDA mixture. Addition of FDA and CDA in the lightweight concrete mixtures reduces the strength of masonry blocks compared to those with only VTP and ECA. The results show that the cement content is an important factor affecting the required strength in mixtures. As represented in Fig.3, for the mix with 7 % CEM I content, the compressive strength of LCHC blocks increases with increasing VTP content of 1 %, 3 % and 5 % by apparent volume. However, not all the mixtures with 7 % CEM I comply with the average strength requirement of BS 6073. On the other hand, the mean compressive strength values of LCHC blocks with a constant CEM I content of 12 % are higher than those of 7 % CEM I mixtures and the use of VTP equal to or more than 1 % by apparent volume seems to be sufficient to meet the minimum average strength requirement of BS 6073: Part 1 for masonry blocks. Although using more VTP increases the strength, dry densities of the blocks also increase, as given in Table 7.

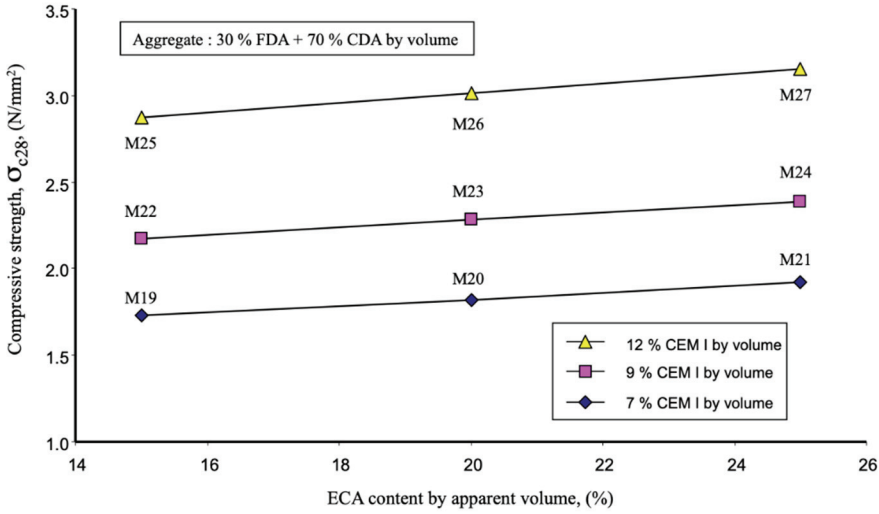

Figure 4 - The 28-day compressive strength versus ECA content by apparent volume for hollow blocks

Figure 4 shows the compressive strength versus ECA content of LCHC blocks containing FDA and CDA mixtures of 30 % FDA + 70 % CDA by apparent volume and with only a constant 3 % VTP as an additive. Fig. 4 indicates that the compressive strengths of LCHC

blocks increases with increasing in ECA contents depending on the CEM I content. However, only up to 12 % CEM I content blocks meet the minimum average strength requirement of 2.8 N/mm^2. The minimum average crushing strength prescribed in BS 6073: Part 1 [26] is 2.8 N/mm^2. Therefore, these blocks can easily be used with 12 % OCEM I content by volume for the purpose of non-load bearing building applications. However, the research showed that the compressive strength of LCHC blocks without VTP attain only very low strength values. Fig. 5 illustrates low average strengths of LCHC blocks made with concretes containing 15, 20, 25 % ECA and appropriate amounts of 50 % FDA + 50 % CDA mixtures did not attain the required strength as experienced in the mixes with 7 %, 9 % and 12 % CEM I, no VTP and the remaining volume completed with appropriate amounts of 30 % FDA + 70 % CDA by apparent volume. Although the dry block densities are much lower, all the mixes (M4 to M15) with appropriate quantities of 50 % FDA + 50 % CDA mixtures added to sum up to 100 % by apparent volume did not meet the strength requirement.

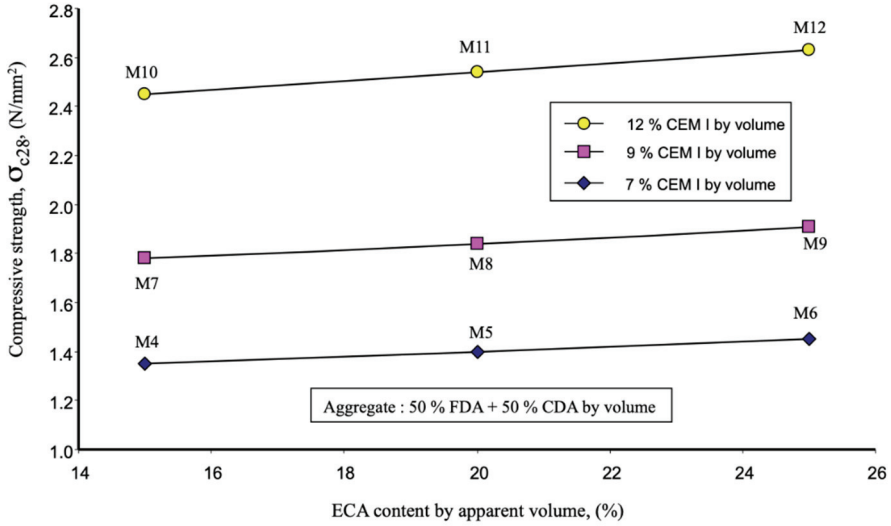

Figure 5 - The 28-day mean compressive strength versus ECA content by apparent volume for hollow blocks

The use of larger maximum size of aggregate affects the strength in several ways. Firstly, since larger aggregates have less specific surface area and the aggregate–paste bond strength is less, concrete fails along surfaces of the coarse aggregates resulting in reduced compressive strength of masonry concrete. Secondly, when a uniform grain size distribution is used, the smaller grains can be found among the larger grains. In this way, the gap volume and thus the need for cement paste is reduced. When the larger grain size is used, the volume of the gap between aggregates and the surface of the aggregate that need to be wrapped with cement paste are reduced. For a given volume of concrete, using larger aggregate particle size results in a smaller volume of cement matrix as the contact surfaces between the aggregates and cement paste will decrease, thereby providing more restraint to volume changes of the cement matrix. This may induce additional stresses in the matrix, creating microcracks prior to

application of load, which may be a critical factor in very high strength concretes [31]. Therefore, it is the general consensus that optimum size aggregates should be well investigated to produce masonry concrete mixtures of sufficient strength. Findings of this experimental research showed that the optimum aggregate size should not exceed 8 mm for masonry block concrete mixtures containing diatomite aggregates.

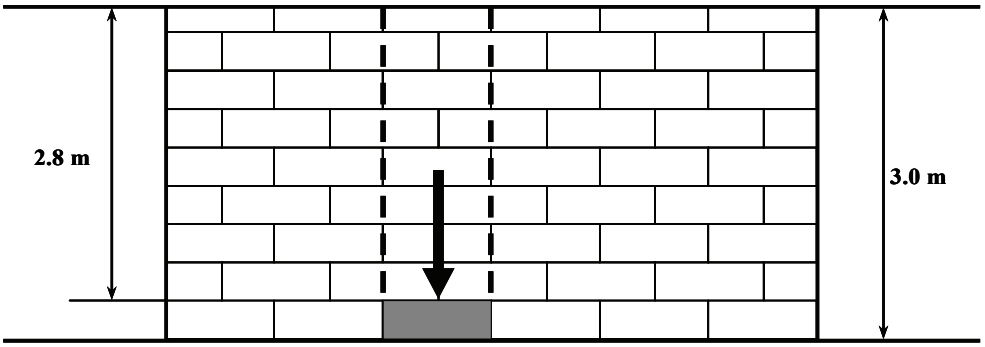

Figure 6 - Dead load acting on a critical lightweight concrete masonry block

The research results showed that some of the LCHC blocks have compressive strengths too low for masonry block application such as M10, M11, M12, M22, M23 and M24 etc. as shown in Table 7. Compressive strength values of these blocks, ranging from 2.17 N/mm^2 to 2.63 N/mm^2, are lower than 2.8 N/mm^2, the minimum LCHC block average compressive strength admissible by BS 6073. On the other hand, the obtained compressive strength values of LCHC blocks may still be acceptable in the context of lightweight masonry units. For instance, in a 3 m high wall built with LCHC blocks, the masonry units placed at the first layer (critical ones) will be under an approximate stress of 0.03 MPa compressive stress corresponding to the dead load related to the weight of the overlying wall as shown in Fig. 6. On the other hand, the obtained experimental ultimate compressive strength of the weakest LCHC blocks was 1.35 MPa which is significantly higher than 0.03 MPa. Therefore, the proposed LCHC blocks may have an acceptable mechanical behaviour in the context of lightweight concrete masonry units for non-load bearing applications.

The density of a lightweight concrete masonry block is expressed as the oven-dry density of concrete in kg/m^3 as determined in accordance with ASTM C 140: Standard Test Methods for Sampling and Testing Concrete Masonry Units and Related Units. In production, the density of a given concrete masonry unit is controlled in part by the methods used to manufacture the unit, but largely by the type of aggregate used in production [32]. Through the use of lightweight aggregates, the resulting density of lightweight concrete masonry units can be varied by the producer to achieve one or more desired physical properties. Block dry density, however, can influence other structural design considerations, aside from compressive strength. Reducing the density of a concrete masonry unit can reduce the overall weight of a structure, and potentially reduce the required size of the supporting foundation and the structural members. Reducing the mass of a structure or element also reduces the seismic load a structure or element must be designed to resist, because the magnitude of seismic loading is a direct function of dead load [32].

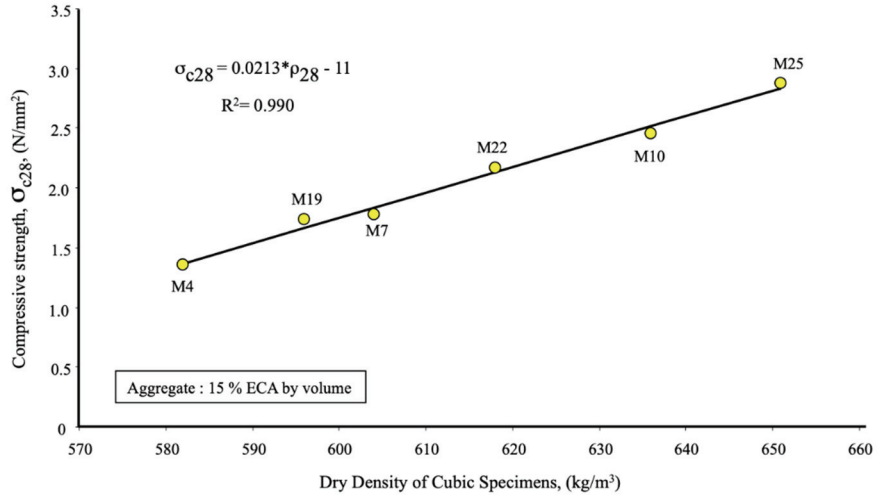

Figure 7 - The 28-day mean compressive strength of hollow blocks versus dry density of cubic specimens

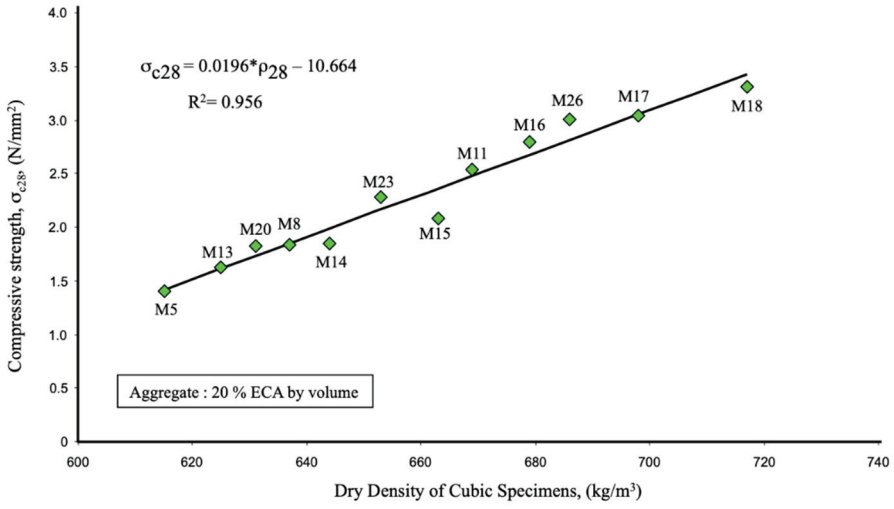

Figure 8 - The 28-day mean compressive strength of hollow blocks versus dry density of cubic specimens

In general, for a given concrete masonry unit mix design, higher compressive strengths can be achieved by increasing the unit density through adjustments to the manufacturing methods. [33]. Therefore, some correlations could be statistically developed for dry density versus compressive strength of the blocks according to constituent aggregate characteristics.

The difference in dry densities of LCHC blocks made with various proportions of VTP and ECA when cured in air environment condition is also presented in Table 7. Figs. 7-9 show relationships between dry density of hollow blocks and their mean compressive strength values at 28 days of curing time for 15 %, 20 % and 25 % ECA content by volume, respectively. As indicated in Figs. 7-9, increase of dry density of hollow blocks increases the compressive strength for all evaluations, too. However, the increase of 5 % ECA in use causes 5.5 % density reduction of masonry blocks on the average. The results indicate that LCHC blocks with high proportions of diatomite aggregates have less density compared to hollow blocks without diatomite aggregates. The difference of block dry density rate is almost near to 50 % with and without diatomite aggregates. It is evident from Table 7 that, the loss in dry block density is found to be as 46.5 % for 50 % FDA + 50 % CDA by apparent volume batches and 44.8 % for 30 % FDA + 70 % CDA by apparent volume batches, respectively. It is also observed that reduction in W/C ratio results in increase in the compressive strength of the LCHC blocks.

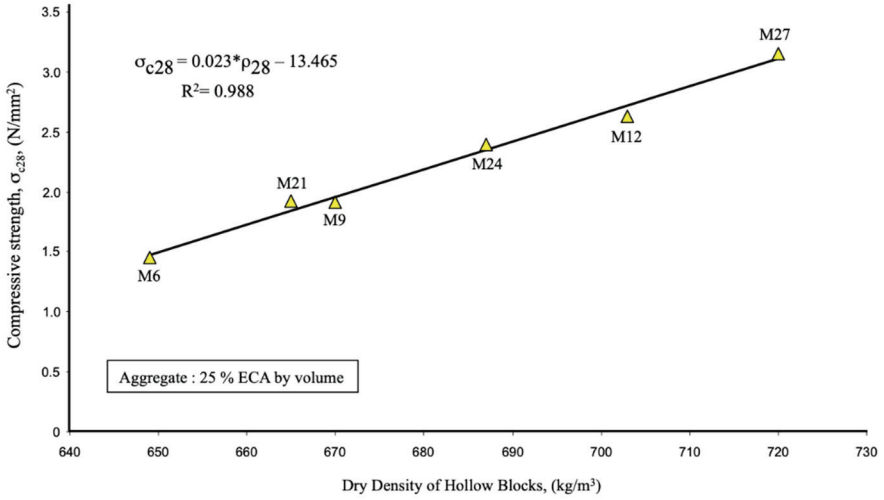

Figure 9 - The 28-day mean compressive strength of hollow blocks versus dry density of cubic specimens

An increase in C/A or cement content does not result in an increase in the bulk volume of concrete, additional cement is accommodated in the voids between the aggregate particles and their porous surfaces. The mixing water demand increases with increasing fine lightweight aggregate content. The results show that, unlike W/C ratio, an increase in A/C ratio seems to result in an increase in compressive strength of LCHC blocks, too. An examination of the data in Table 7 shows also that the minimum required strength according to BS 6073 is not achieved in LCHC blocks without VTP.

3.3. Water Penetration and Absorption

Lightweight hollow concrete masonry unit specifications typically establish upper limits on the amount of water permitted to be absorbed. Expressed in kilogram of water per cubic meter of concrete, these limits vary with the density classification of the unit. Although no limit value for water absorption has been stated in BS 6073: Part 1 for the concrete masonry units, US National Concrete Masonry Association proposes that the maximum water absorption should be lower than 288 kg/m^3 for lightweight concrete masonry units [32]. The mean values for water absorption of LCHC blocks are given in Table 7. In this table, it is clearly observed that all absorption values are in the range of 100 kg/m^3 and 170 kg/m^3, within the acceptable water absorption values according to US National Concrete Masonry Association recommendation. The research findings show that there is a close relation between water absorption and compressive strength of lightweight masonry blocks, as illustrated in Figures 10 and 11 for different mixes. The analysis results show that there is a logarithmic relationship between the compressive strength and water absorption for LCHC blocks. The increases in the compressive strengths of masonry units are generally associated with reduction in water absorptions and an increase in cement and VTP contents. The increases in cement and VTP contents are the major factors reducing the water absorption of the masonry units. Unlike the cement and VTP contents, the increase of diatomite aggregate content is an effective factor increasing the water absorption capacity of LCHC blocks due to diatomite aggregates having high porosities. The water absorption values of LCHC blocks without VTP approximately range between 140 kg/m^3 and 170 kg/m^3. This range is higher than that of the mixes containing VTP and ECA. While the absorption values are not directly related to masonry unit physical and geometrical properties such as dimension, pore size and to mechanisms of deterioration such as freeze-thaw, they do provide a measure of the void structure within the lightweight concrete of the masonry unit. Several production variables can affect the void structure, including degree of compaction, binder and water content of the plastic mix, aggregate gradation and the parameters of the mixing operation.

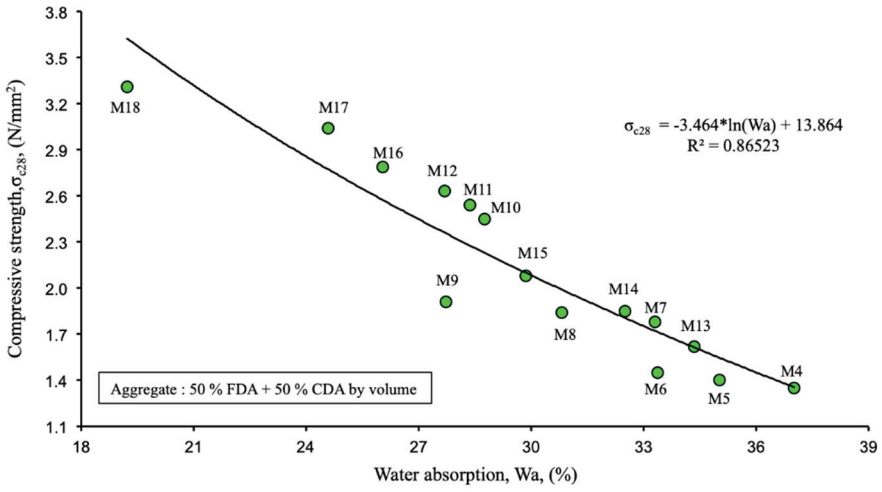

Figure 10 - The 28-day mean compressive strength versus water absorption of hollow blocks

Due to the vesicular structure of lower density units, there is a potential for higher measured absorption than is typical for higher density units [32]. This effect is observed in LCHC blocks almost for all mixes.

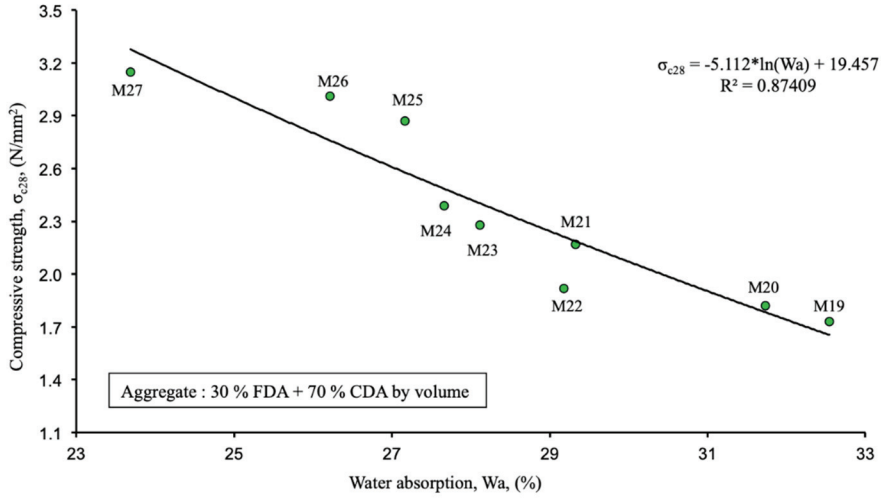

Figure 11 - The 28-day mean compressive strength versus water absorption of hollow blocks

Consequently, ASTM C 90 permits lower density lightweight masonry units to have higher maximum absorption values. The higher absorption limits permitted by ASTM C 90 for lower density units do not necessarily correlate to reduced water penetration resistance. One reason is that water penetration resistance is known to be highly affected by workmanship and dependent on detailing for water management. It is generally recognized that these two factors more heavily influence the wall's water penetration resistance than do other factors, such as unit density [32]. Corroborating this view, it was generally observed in this research that increase of masonry density reduced the water penetration of LCHC blocks. For thermal comfort as affected by the building envelope, water content of masonry blocks should be kept as low as possible [2]. Although no limiting value for water absorption of concrete masonry units was stipulated in BS 6073, it is usually accepted that less than 300 kg/m^3 of water absorption for individual masonry unit is more appropriate for the partitioning and curtain walls in buildings. When the test results evaluated according to water absorption limits of U.S. National Concrete Masonry Association (<288 kg/m^3), the experimental research study showed that LCHC blocks having less than 880 kg/m^3 of dry unit density provide the convenient water absorption capacity for quaternary blends containing volcanic tuff powder, expanded clay aggregate, diatomite and cement to produce LCHC blocks for non-load bearing walls and partitions (Table 7).

3.4. Masses of masonry units

The research showed that increasing the cement and VTP content increases the block unit mass. On the other hand, an increase of diatomite aggregate content generally results in mass reduction of masonry units due to its comparatively very low particle density than cement, VTP and ECA. Masses of the hollow blocks containing only VTP and ECA aggregates varied between 11.86 kg and 11.98 kg and those containing ECA and diatomite aggregates without VTP varied between 6.20 kg and 7.48 kg. In a combination of VTP, ECA, FDA and CDA, the masses of LCHC hollow blocks varied between 6.33 kg and 7.66 kg. It was also observed that increase of coarse diatomite aggregate in the mixture reduced the mass of the blocks. In general, the experience for this reduction for the hollow blocks used in this research was approximately 3 % block mass reduction versus 1 % increase in coarse diatomite aggregate content. Assuming the mass of normal weight aggregate concrete masonry for non-load bearing walls and partitions vary between 14 kg and 27 kg depending on their unit design geometry, the research work showed that LCHC blocks are 55 % to 72 % lighter than normal weight concrete masonry units. Furthermore, under masonry production conditions in Turkey, it is seen that LCHC blocks are also found to be 27 % - 33 % lighter than pumice aggregate lightweight concrete masonry units.

4. CONCLUSIONS

The properties of lightweight hollow concrete masonry units made of CEM I (Portland cement) volcanic tuff powder, expanded clay aggregate and diatomite aggregates were investigated in this research work. The LCHC blocks were manufactured using mix compositions in current use and applying common production technology complying with the requirements of BS 6073: Part 1 and Part 2 [26]. It was possible to manufacture standard shape and size LCHC blocks using dry to stiff consistency mixtures to keep their shape and size during the demoulding, curing and hardening processes. The dry densities of the LCHC blocks complied with the standard acceptable limits for lightweight hollow concrete masonry units (i.e., less than 880 kg/m^3).

The research findings show that the higher the amount of diatomite aggregates in the mixture, the lesser the dry density of LCHC blocks. Addition of VTP in a mixture increases the block strength. An increase of 2 % (by apparent volume) VTP with ECA provides approximately 18.5 % to- 19.0 % increase in the compressive strengths of the blocks. Lightweight concrete mixtures of 7 % and 9 % CEM I contents containing appropriate amounts of 50 % FDA + 50 % CDA or 30 % FDA + 70 % CDA mixtures by apparent volume do not qualify for use in producing CHLM blocks due to their insufficient strengths. All the mixtures with 9 % CEM I by apparent volume with only VTP and ECA aggregate mixes do comply with the strength requirements of BS 6073.

The volcanic tuff powder particles' being covered with cement paste tends to reduce the water absorption of the particles, and also to improve the adherence between the hardened cement paste and the surface of aggregate particles. It was noticed that there is a significant difference between the compressive strengths of LCHC blocks produced with only VTP+ECA and those with VTP+ECA+FDA+CDA. In fact, the compressive strengths of LCHC blocks with only VTP+ECA are 20 % to 70 %, and, on the average almost 50 % higher than the respective strengths of LCHC with VTP+ECA+FDA+CDA. Therefore, it is necessary to conduct

additional research work in order to improve the material properties of the LCHC with VTP+ECA+FDA+CDA. The evaluation of the diatomite- Portland cement compatibility in masonry concrete mixtures is a technical aspect that should be further studied.

Within the 2.8/1 to 7.3/1 range of A/C ratios, oven dry densities between 452 kg/m^3 and 874 kg/m^3 and compressive strength values between 1.35 N/mm^2 and 4.16 N/mm^2 can be achieved depending on the mixture proportions. Water absorptions of LCHC blocks, in the present investigation varied between 107 kg/m^3 and 168 kg/m^3. Although no limiting value for water absorption has been stated in BS 6073: Part 1 for the concrete masonry units, U.S. National Concrete Masonry Association proposes that the maximum water absorption should be lower than 288 kg/m^3 for lightweight concrete masonry units. Very low water absorption values were determined in this research as compared to the water absorption limit of U.S. National Concrete Masonry Association. The masses of LCHC blocks produced are found to be 55 % – to 72 % less than those of the normal weight hollow units. This could be considered as an important parameter in terms of reducing dead loads in buildings.

According to the results of the research, the compressive strength value of M3 mixture, which does not contain diatomite, was determined as the highest compressive strength value (4.6 MPa). However, as a function of the high compressive strength value, the unit volume value of the block is also quite high (874 kg/m^3). The low unit weight and high strength masonry block product with the quaternary mixture content according to the concept of the study was obtained in M18 coded mixture design. The average compressive strength of these blocks is 3.31 MPa, the unit weight is 557 kg/m^3 and the water absorption is 107.07 kg/m^3. The lowest water absorption value is achieved by this mixture design. On the other hand, if it is desirable to produce LCHC with a lower unit weight, it is necessary to make some concessions from compressive strength and water absorption values. The M25 mixture, which has a lower volume weight, seems to be positive in this regard. It provides the required standard values for compressive strength and at the same time it has a relatively low unit weight.

It is advised that the thermal insulation, sound absorption and drying shrinkage properties of these LCHC blocks could be studied as a future work. Hence, the effects of VTP, FDA and CDA can be examined in more detail.

References

[1] CEM IA, Concrete Masonry Units, America's Cement Manufacturers, 2016, USA

[2] Gündüz L., Use of quartet blends containing fly ash, scoria, perlitic pumice and cement to produce cellular hollow lightweight masonry blocks for non-load bearing walls. Construction and Building Materials 22, 747–754, 2008.

[3] Turkmenoglu, A. G., Tankut, A., Use of tuffs from central Turkey as admixture in pozzolanic cements assessment of their petrographical properties. Cem. Concr. Res. 32, 4, 629-637, 2002.

[4] Faella, G., Manfredi, G., Realfonzo, R., Cyclic behaviour of tuff masonry walls under horizontal loading. Proc. 6th Can. Masonry Symp., Canada, 317-328, 1992.

[5] Iwaro, J., Mwasha, A., Effects of using coconut fiber–insulated masonry walls to achieve energy efficiency and thermal comfort in residential dwellings. Journal of Architectural Engineering, 25(1), 04018035, 2019.

[6] Mahoutian, M., Chaallal, O., Shao, Y., Pilot production of steel slag masonry blocks. Canadian Journal of Civil Engineering, 45(7), 537-546, 2018.

[7] Annual books of ASTM standards, volume 04.02 and Volume 04.03, 2002.

[8] Gündüz, L., A technical report on lightweight aggregate masonry block manufacturing in Turkey. Suleyman Demirel University, Isparta, Turkey, 1-110, 2005.

[9] Weber, S., Curing of high strength concrete using lightweight aggregates, Bauberatung Zement Stuttgarti Loenberg. 377-391, 1997.

[10] BS 812: Part 2, Testing aggregates. Methods for determination of density, 1995, UK.

[11] BS 812 : Part 110, Testing aggregates. Methods for determination of aggregate crushing value (ACV), 1990, UK.

[12] ASTM C127-04 Standard test method for density, relative density (specific gravity), and absorption of coarse aggregate, USA.

[13] ASTM C128-04a Standard test method for density, relative density (specific gravity), and absorption of fine aggregate, USA.

[14] Ritmann, L., Volcanoes. London, UK: Orbis Publishing; 1980.

[15] Toprak, M.U. and Arslanbaba, M. A., Possibility of using Kütahya Volcanic Tuff as building stone: Microstructural evaluation and strength enhancement through heat treatment. Construction and Building Materials, 110, 128–134, 2016.

[16] Wang J., Jung W., Li Y. And Ghassemi A., Geomechanical characterization of Newberry Tuff. Geothermics, 63, 74-96, 2016.

[17] Tuncay, E., Rock. Original Research Article, International Journal of Rock Mechanics and Mining Sciences, 46(8), 1253-1266, 2009.

[18] Özguven, A. Genleşen kil agrega üretimi ve endüstriyel olarak değerlendirilmesi. PhD thesis. Isparta: University Süleyman Demirel; 2009 [in Turkish].

[19] Özguven, A. and Gunduz, L., Examination of effective parameters for the production of expanded clay aggregate. Cement & Concrete Composites 34, 781–787, 2012.

[20] Doğan, H. and Şener, F., Hafif yapı malzemeleri (pomza-perlit-ytong-gazbeton) kullanımının yaygınlaştırılmasına yönelik sonuç ve öneriler. TMMOB. The Newsletter of the Chamber of Geology Engineers, 1, 51–53, 2004 [in Turkish].

[21] Ha, J.H., Lee, J., Song, I. H. and Lee, S. H., The effects of diatomite addition on the pore characteristics of a pyrophyllite support layer. Ceramics International, 41(8), 9542-9548, 2015.

[22] Xu, S., Wang, J., Jiang, Q. and Zhang, S., Study of natural hydraulic lime-based mortars prepared with masonry waste powder as aggregate and diatomite/fly ash as mineral admixtures. Journal of Cleaner Production, 119, 118-127, 2016.

[23] Inchaurrondo, N., Font, J., Ramos, C.P., Haure, P., Natural diatomite: Efficient green catalyst for Fenton-like oxidation of Orange II. Applied Catalysis B: Environmental, 181, 481-494, 2016.

[24] BS 1881: Part 125, Testing concrete. Methods for mixing and sampling fresh concrete in the laboratory, 1986, UK.

[25] BS 1881: Part 114, Testing concrete. Methods for determination of density of hardened concrete, 1983, UK.

[26] BS 6073: Part 1, Precast concrete masonry units. Specification for precast concrete masonry units, 1981, UK.

[27] Abali, Y., Bayca, S. U., Targan, S., Evaluation of blends tincal waste, volcanic tuff, bentonite and fly ash for use as a cement admixture. J. Hazard. Mater., 131, 126-130, 2006.

[28] Smadi, M. M., Migdady, E., properties of high strength tuff lightweight aggregate concrete. Cem. Concr. Comp., 13(2), 129-135, 1991.

[29] Faustino, J., Silva, E., Pinto, J., Soares, E., Cunha, V.M.C.F., and Soares, S., Lightweight concrete masonry units based on processed granulate of corn cob as aggregate. Materiales de Construcción, 65(318), e055, 2015.

[30] BS EN 771-3, 2011, Specification for masonry units. Aggregate concrete masonry units (dense and lightweight aggregates).

[31] Neville, A.M., Properties of concrete. London, Longman Scientific and Technical series, 2000.

[32] TEK 2-6, Density-related properties of concrete masonry assemblies, National Concrete Masonry Association, an information series from the national authority on concrete masonry technology, 2008, USA.

[33] Holm, T. A., Engineered masonry with high strength lightweight concrete masonry units. Concrete Facts, 17(2), 1972.

Teknik Dergi, 2020 10315-10337, Paper 592

Corrosion and Chloride Diffusivity of Reinforced Concrete Cracked under Sustained Flexure

Nilüfer ÖZYURT[1]
Tayfun Altuğ SÖYLEV[2]
Turan ÖZTURAN[3]
Ahmet Onur PEHLİVAN[4]
Anıl NİŞ[5]

ABSTRACT

This research discusses the chloride diffusivity of concrete as well as corrosion performance of rebars in cracked and uncracked states. Prismatic concrete specimens with two water-to-cement ratios, two concrete cover thicknesses with and without steel fibers were used. Three-point flexural loading was applied to form cracks and cracks were sustained by a bolt system. Half-cell potential and corrosion rate measurements were carried out following wetting - drying cycles in chloride environment which were continued for 80 weeks. The positive effects of lower water-to-cement ratio and greater cover depth were found to be surpassed by existence of cracks in concrete.

Keywords: Corrosion, cracked concrete, corrosion rate, chloride profiles, diffusion coefficient, fibers, sustained crack width, sustained flexure.

1. INTRODUCTION

Corrosion is a major cause of deterioration for concrete structures. Especially chloride induced corrosion is one of the most severe of all corrosion mechanisms. Thus, penetration of chloride into concrete and chloride induced corrosion has been an important issue in the

Note:
- This paper has been received on June 4, 2018 and accepted for publication by the Editorial Board on May 30, 2019.
- Discussions on this paper will be accepted by January 31, 2021.
- https://dx.doi.org/10.18400/tekderg.430536

1 Boğaziçi University, Department of Civil Engineering, İstanbul, Turkey - nilufer.ozyurt@boun.edu.tr - https://orcid.org/0000-0003-4533-8702

2 Gebze Technical University, Department of Civil Engineering, Kocaeli, Turkey - tasoylev@gtu.edu.tr - https://orcid.org/0000-0001-5042-0431

3 Boğaziçi University, Department of Civil Engineering, İstanbul, Turkey - ozturan@boun.edu.tr - https://orcid.org/0000-0001-8097-3838

4 Maltepe University, Department of Civil Engineering, İstanbul, Turkey - onurpehlivan@maltepe.edu.tr - https://orcid.org/0000-0002-6296-4126

5 İstanbul Gelisim University, Department of Civil Engineering, İstanbul, Turkey - anis@gelisim.edu.tr - https://orcid.org/0000-0001-9092-8088

design of concrete structures and studied by several researchers [1-7]. Penetration of chloride ions into concrete destructs the passivation layer on the reinforcement and initiates the corrosion process. Corrosion of rebars degrades the performance of reinforced concrete structure by decreasing the cross-sectional area of reinforcement and deteriorating the bond between concrete and steel.

Previous research on corrosion of concrete has been conducted mostly on uncracked specimens however cracks in reinforced concrete structures are inevitable. In practice, concrete can crack due to several reasons and these cracks can alter the mechanism and duration of chloride penetration. Transportation of chloride ions in cracked specimens takes less time with respect to uncracked ones. Hence, it is very important to study the influence of cracks on the corrosion of rebars and chloride penetration in concrete. Effects of cracks on water, gas and chloride permeability have been investigated in several studies that led to controversial results and no clear conclusion can be derived. Effects of cracks on permeability of concrete were investigated in several studies and it was found that cracks affect the ingress of water into concrete [8-10].

In recent years, some researchers conducted chloride penetration tests on specimens with flexural cracks. Rodriguez and Hooton [1] studied the chloride ingress in artificially cracked concrete and concluded that cracks did not affect the diffusion coefficient. Win et al. [2] formed cracks on reinforced concrete specimens and exposed preloaded cracked specimens to chloride environment and concluded that cracks accelerated the penetration of chloride ions. Şahmaran [11] exposed preloaded cracked specimens at different crack widths to sodium chloride solution and concluded that specimens with crack widths lower than 0.135 mm had marginal chloride penetration where for the specimens with cracks larger than 0.135 mm diffusion coefficient increased rapidly. Marsavina et al. [3] used beam specimens with artificial cracks and concluded that cracked specimens showed higher chloride penetration in comparison with the uncracked specimens. In these studies, cracks were either artificial or loads applied to form cracks were removed after obtaining the intended crack width. Since structural members are under service loads at all times, removing the loads before exposing test specimens to aggressive environment may not represent the real situation. Sustaining the loads (to keep the crack open) may give more realistic results. Gowripalan et al. [4] used a ratio of crack width to concrete cover depth and studied the chloride diffusivity in the tension and compression zones of concrete cracked under sustained bending and found that the chloride diffusivity in the cracked tension zone was higher than the compression zone. Wang et al. [12] studied the chloride transport in concrete under sustained loads and concluded that chloride diffusivity decreased in the compression zone, while increased in the tension zone of the specimens. An increase in surface crack width from 0.05 mm to 0.20 mm caused a significant increase in the chloride content of concrete [13]. Crack width played a dominant role in chloride transport in cracked concrete (for transverse crack width up to 0.4 mm) together with the concrete quality [14].

Considerable amount of research was also conducted on the effects of cracks on reinforcement corrosion. Beeby [15] reported that effect of cracks loses its significance in long term. Also, in some other studies, effects of cracks were found to be small after the corrosion initiation period [5, 16]. In a study of Mohammed et al. [17], authors found that cracks that occurred under flexural loading increased the oxygen permeability of concrete cover and the oxygen concentration at the reinforcement level and thus increased the risk of

corrosion. In another study of Mohammed et al. [18], authors concluded that cracks increased the risk of corrosion, yet effect of crack width was lower than the effect of water-to-cement ratio. Most studies in literature are on the chloride penetration into saturated concrete. However, in reality concrete was found to be unsaturated, especially when it was subjected to wetting-drying cycles [19].

The results of the research study carried out by Otieno et al. suggested that for a given concrete quality (binder type and w/b ratio) and cover depth, corrosion rates increased with increase in crack width (w_{cr}) in the order: uncracked < 0.4 mm cracked < 0.7 mm cracked under chloride exposure. However, corrosion rate at a given crack width varied depending on the cover depth (20 mm and 40 mm) and concrete quality. For a given concrete cover thickness-to-surface crack width ratio (c/w_{cr}), corrosion rates varied significantly depending on the concrete quality [20]. The effect of the c/w_{cr} ratio was also reflected to the findings of Lu et. al, which showed an average loss in the diameter of steel bar in concrete with 0.2 mm crack more than twice as high as that of the uncracked concrete for 20 mm cover thickness, whereas there was only a slight increase in the loss of diameter for 40 mm cover thickness. According to the study, when the crack width was less than 0.1 mm, it did not affect the corrosion [14]. On the other hand, the study of Berrocal et al. indicated that after a period of 120 days chloride exposure, the specimen with 0.1 mm crack width started to corrode, while the uncracked specimens showed no sign of corrosion after 200 days of cyclic chloride exposure [21]. The shorter corrosion initiation time in the presence of transverse crack width smaller than 0.1 mm was reported by other studies. These studies found also higher corrosion rate results in the specimens with low crack width, which were supported by the visual observation of the steel surface [22-23]. Sangoju et al. concluded that the presence of the crack influences corrosion more than the crack width itself as mentioned also in another study [23], when they found that the increase in weight loss between the uncracked to 0.2 mm crack-width specimens was higher than between the 0.2 and 0.4 mm crack-width specimens. The weight loss for both uncracked and precracked specimens of plain concrete was in the range of 11.9–22.4%, 13.9–25.2%, and 18.5–33.4%, respectively for w=c of 0.37, 0.47, and 0.57. It is interesting to note that, the mass loss in the highest quality but cracked concrete is higher than that in the lowest quality but uncracked concrete [24]. The increase in crack width shortened the corrosion initiation time [21] and significantly affected the corrosion rate [23] varying from 0.1 mm to 0.4 mm and from 0.1 to 1.0 mm, respectively.

Steel fibers are mainly used for enhancing the mechanical behavior of concrete structures. However, in addition to mechanical strength, durability properties of steel fiber reinforced concrete should also be investigated for better evaluation of the performance of the concrete structures. Studies focusing on the corrosion of steel fiber reinforced concrete are very limited. Granju and Balouch agreed that corrosion arising from cracks is less severe when steel fibers are used [25]. However, as stated by other researchers [26] contradictory results exist on the use of fibers in chloride environments together with reinforcing bars. Therefore, further research on the subject is needed. The use of steel fibers provided a slight reduction in the corrosion initiation time for reinforcing steel embedded in cracked concrete (0.1 mm - 0.4 mm) under chloride exposure. However, there was significant improvement in corrosion resistance by the use of PVA fibers and hybrid fibers (steel + PVA) [21]. According to the results of another study, there was no significant difference in terms of corrosion resistance measured by the gravimetric loss in the concrete with hybrid fibers (steel + PVA) with respect to the plain concrete [27].

From the above studies, it is understood that concrete cover thickness and quality are important parameters when chloride ingress into concrete is considered. However, in reality under service loads cracks can occur thereby altering the situation into a more complicated state about the parameters affecting corrosion of rebars. In this study, a more realistic approach to the exact situation of reinforced concrete structures was investigated in order to understand the effect of different parameters (cracks, fiber inclusion, concrete cover depth and quality). Cracks were formed and kept open under sustained loads. Crack widths were 0.4 mm for non- fibrous specimens, while they varied between 0.22 – 0.34 mm for fibrous specimens. Maximum allowable crack width values from 0.1 to 0.4 mm were given in different standards/guidelines (ACI 224.01 [28], ACI 318-08 [29]) in the last decades. Comparative tables were prepared by different researchers to analyze approach of several standards/countries [4,11,30]. Unfortunately, there is still no consensus on the acceptable crack width values. The limits defined in the standards maybe useful while designing new structures. However, the studies carried out on the existing structures showed that cracks with much greater widths than mentioned in the guidelines are encountered in the concrete. Baah [31] carried out a study on the slabs of 13 structural bridges in Ohio and prepared a table to represent recorded maximum crack widths. He stated that cracks from 0.7 mm to 3.3 mm were measured under dead load only. A crack width as great as 3.3 mm means a direct passage to reinforcement, even for very large cover depths. Considering such findings, a relatively high maximum crack width value (0.4 mm) was selected for this study. Specimens were exposed to severe chloride environment (3.5 % NaCl solution) by applying wetting-drying cycles for 80 weeks and weekly corrosion data (half-cell potential and corrosion rate) were recorded. After the exposure duration, chloride diffusion profiles were obtained and chloride diffusion coefficients were estimated. Also, images of corroded rebars were taken and analyzed for the compatibility of the results with each other.

2. EXPERIMENTAL STUDY

2.1. Materials and Mix Design

Type I Portland cement (CEM I 42.5 R), two types of coarse aggregates (D_{max} = 20mm) and crushed as well as local river sand were used in making the concretes. ASTM C494 type F high range water-reducing superplasticizer (naphtalene based) was added to achieve a slump of about 17 ± 2 cm. Hooked end steel fibers of 0.55mm diameter and 35 mm length (length/diameter ratio=65) with a tensile strength of 1100 MPa were used in fibrous specimens.

Two water-to-cement ratios (0.45 and 0.65) and two different concrete cover depths (25 mm and 45 mm) were used with and without fibers. Details of the mix proportions are given in Table 1.

Eight series of concretes were produced to cast 64 concrete prisms (100 x 100 x 500 mm) with reinforcing bars. Specimens were cast in two layers and compacted using a vibrating table. After casting, specimens were covered with plastic sheets to prevent evaporation of mix water. Prisms were demolded after 24h and cured in moist room at 23±2 °C for 28 days. Three cylinder specimens with a diameter of 100 mm and a height of 200 mm were also cast from each series for compressive strength testing.

Table 1 - Mix proportions of concrete.

Mixes	w/c	Mix proportions (kg/m^3)					
		Cement	Water	Sand	Coarse Aggregate	Steel Fiber	SP
F065	0.65	310	201	797	1054	0	2.22
F045	0.45	400	180	797	1043	0	6.30
F165	0.65	310	201	797	1054	39	3.48
F145	0.45	400	180	797	1043	39	6.85

Following notation was used for designation of the specimens. F1 and F0 stand for the specimens with and without fibers. The following numbers, 45 and 65 show the water-to-cement ratio of the specimens, 0.45 and 0.65, respectively. The last two digits indicate concrete cover thickness of 25 mm and 45 mm. Thus, F14525 represents concrete with fibers, cast by using a w/c of 0.45 and a cover thickness of 25 mm.

2.2. Mechanical Tests

- **Compressive strength tests**

Compressive strength tests were performed according to ASTM C39 [32] on 100 x 200 mm cylinders at the age of 28 days.

- **Evaluation of force vs. crack width relation (preliminary experiments)**

Three-point bending tests were conducted to create the maximum possible crack width and to determine the ultimate flexural capacity of the reinforced concrete prisms in order to see also whether or not a 0.4 mm crack width can be achieved for all the specimens (Figure 1).

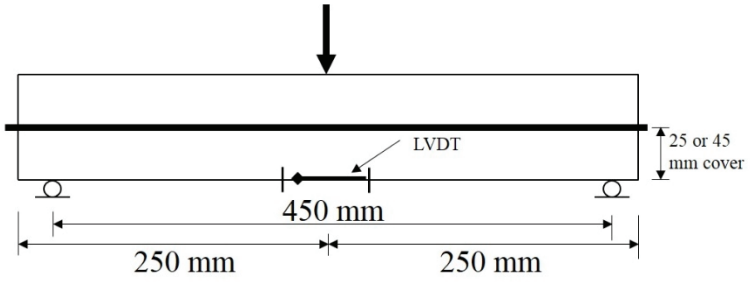

Figure 1 - Three-point bending test set-up

- **Sandwich cracking of specimens**

Each concrete prismatic specimen was reinforced with a 14 mm hot-rolled ribbed bar with a characteristic yield strength of 420 MPa as was stated above. The rebars were extended

beyond the concrete at both ends, in order to make corrosion measurements effectively. In order to sustain flexural loads on the prisms and prevent the closing of cracks, a set-up depicted in Figure 2 was used. As illustrated in Figure 2, a dummy specimen with identical properties was used for creating similar bending rigidity (32 dummy specimens were cast total, 4 specimens were used for each series). A smooth steel rod was placed between the dummy and the test specimens in the test setup in order to create compression and tension stresses on the inner and outer sides of the specimens, respectively. The system was loaded under stroke displacement control. Loading was applied at a rate of 0.001 mm/sec. When the crack width of 0.4 mm was achieved, bolts were tightened to sustain the load on the specimen and eventually the width of the crack. Two LVDTs were placed on both sides at the midsection of the tension zone of the test specimen as can be viewed from Figure 2 to measure the crack width. Specimens without fibers were cracked at mid-span to a crack width of 0.4 mm. Flexural loads needed to open the crack to a width of 0.4 mm were recorded. Fibrous specimens were loaded up to the pre-recorded flexure loads (for non-fibrous specimens) by using the same set-up, and the corresponding crack widths were recorded.

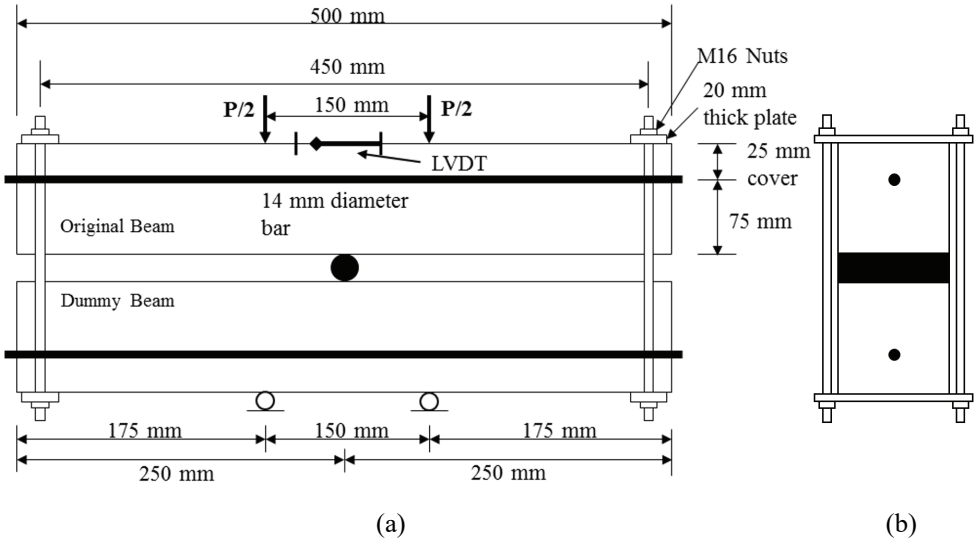

Figure 2 - Schematic diagram of the test setup ((a) front view and (b) side view).

2.3. Exposure Conditions

After cracking process, 70x130x15 mm reservoirs were made on the cracked face of each test beam by using silicon and a cement-based material for waterproofing. A 35g/l NaCl solution was used to expose the specimens to repeated cycles of 4 day ponding followed by 3 day air drying period. These cycles were continued for 80 weeks for the cracked and uncracked specimens. Cracked specimens were under sustained loading during exposure. Temperature and relative humidity of the storage area were measured and noted at certain intervals.

2.4. Corrosion Monitoring

Two different corrosion assessment techniques were used. Corrosion measurements were made in accordance with ASTM C876 [33] by galvanostatic pulse technique with an Ag/AgCl electrode (SSCE) measuring both corrosion rate and half-cell potential at the same time. A short time anodic current pulse is applied to reinforcement galvanostatically from a counter electrode placed on concrete surface together with a reference electrode. With the applied current, reinforcement gets polarized in the anodic direction compared to its free corrosion potential. A reference electrode which is placed in the center of the counter electrode record the resulting change of the electrochemical potential of the reinforcement as a function of polarization time.

Half-cell potential and corrosion rate measurements began 10 weeks after exposure due to a breakdown in the galvanostatic pulse device. In order to compensate for the missing data, new series of concrete specimens were cast and tested in uncracked state (3 specimens for each series). The comments on the results obtained from later produced uncracked specimens will be given in results and discussion section.

For half-cell circuit, it can be said that a certain decrease in the half-cell potential of the rebar can be correlated with the time to depassivation whereas corrosion rate is related to the loss of reinforcement cross-section. While half-cell measurements give information about corrosion initiation time, corrosion rate measurements are used to evaluate overall life time performance of rebars. Therefore, corrosion rate results are used as one of the most significant input parameters in corrosion-induced damage prediction models for reinforced concrete structures.

2.5. Chloride Content Measurements

Chloride ion profiles and diffusion coefficient of concrete were evaluated in accordance with ASTM C1556 [34]. There are several chloride transport mechanisms that can take place in concrete. These are a) diffusion under the influence of a concentration gradient, b) absorption due to capillary suction, c) migration in an electric field, d) pressure induced flow and e) wick action when water absorption and water vapor diffusion are combined [6].

The transport mechanism occurring in the case of chloride ingress into concrete is diffusion under the influence of a concentration gradient. The transport of the chloride ions into concrete specimens under sustained loading is assumed to be one dimensional in a semi-infinite medium complying with Fick's second law of pure diffusion given as,

$$\frac{\partial C}{\partial t} = D\,\frac{\partial^2 C}{\partial^2 x} \tag{1}$$

Where C = chloride concentration in concrete; t = exposure time, D = chloride diffusion coefficient and x = distance from surface.

An analytical solution to Equation 1 can be given by:

$$C(x,t) = C_S\left[1 - erf\left(\frac{x}{2\sqrt{Dt}}\right)\right] \quad (2)$$

Where C(x, t) is the chloride ion concentration at depth x after exposure time t for a chloride concentration of C_s at the concrete surface and the expression erf is the Gaussian error function.

Apparent chloride diffusion coefficient, D, and surface concentration, C_s, were determined by fitting the Equation 2 to the measured chloride contents by a non-linear regression analysis using the method of least squares. In the analysis of the chloride profile, the sum of the squared differences between the fitted and the actual data for the chloride-ion content of each sample must be minimized by adjusting the regressor variable [6]. Initial chloride content that may come from the mix ingredients can be neglected (if materials used are carefully controlled) in analyzing the chloride profiles [34]. Surface chloride content, C_s, is difficult to determine since chloride content at concrete surface is reduced due to several reasons. This is why C_s values were determined by fitting Equation 2 as suggested in the literature.

After completion of wetting - drying cycles for 60 and 80 weeks, the specimens were unbolted to be released from suspended load and measurements of chloride contents at different depths of concrete were done using the following procedure. First, powder samples from different depths of concrete specimens were collected by a profile grinder machine. Grinding process was carefully done by appropriate devices starting from the outmost layer exposed to NaCl solution going into deeper layers with intervals of 0-5 mm, 5-10 mm, 10-15 mm, 15-20 mm, 20-30 mm, 30-40 mm from concrete surface to the steel bar, pulverizing concrete into powder and handling carefully without any contamination. Second, chloride content of powder sample obtained from each layer was determined by acid soluble extraction in a nitric acid solution which was treated against 0.05 N silver nitrate ($AgNO_3$) by potentiometric titration within the requirements and precision levels given in ASTM C1152 [35]. Then, chloride content of each solution was calculated as percentage by weight of concrete. Finally, these results were used to create chloride profiles to determine diffusion coefficients (D) and surface concentrations (C_s).

3. RESULTS AND DISCUSSION

3.1. Fresh Concrete Properties

All concrete mixes were cast to achieve a slump of 17±2 cm as mentioned before. Slump, air content and density measurements were done for all mixes. Resulting fresh concrete properties can be seen in Table 2.

3.2. Mechanical Properties

3.2.1. Compressive Strength Analysis

Compressive strengths of 100 x 200 mm cylindrical specimens were determined at the age of 28 days by applying compressive axial load at a rate of 4.8 kN/sec. Compressive strength of concretes as average of 3 specimens can be seen in Table 2.

Table 2 - Fresh state and compressive strength tests results

Mixes	w/c	Slump (cm)	Air Content (%)	Density (kg/m^3)	f_c (MPa)
F065	0.65	17.5	3.5	2250	29.8
F045	0.45	17.0	3.8	2320	49.0
F165	0.65	17.5	5.2	2300	28.1
F145	0.45	17.0	4.8	2360	47.9

3.2.2. Flexural Strength Analysis

Flexural tests were done to obtain failure load and crack width that can be achieved as explained in experimental study section. A crack width of 0.4 mm was selected as the critical crack width in this study. Figure 3 (a) and (b) show force vs. crack width relations for the specimens with cover depths of 45 mm and 25 mm, respectively.

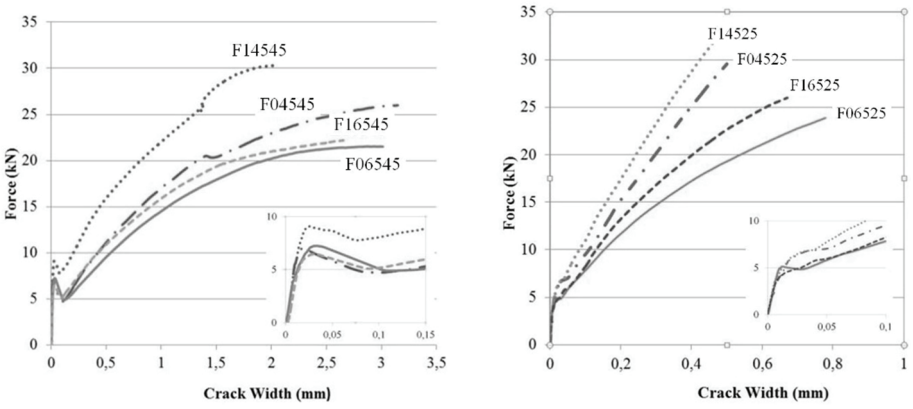

(a) (b)

Figure 3 - Force vs. crack width relations of the specimens with a cover thickness of (a) 45 mm and (b) 25 mm

First cracking behavior of concrete is given in the onset of Figure 3 (a) and (b). Following the first cracking, deformations increased at a decreased stress level and after that the effect of steel reinforcement was seen (increased bending capacity of the section) for the higher cover thickness. In other words, there is a transition phase from plain concrete to reinforced concrete. Fiber presence can easily be identified with additional flexural capacity especially in higher quality concretes (w/c = 0.45). Specimens with 25 mm cover depth had less than 1 mm crack widths until failure while specimens with 45 mm concrete cover depth had three times higher crack widths before failure occurs. The flexure tests showed that it was possible to create selected critical crack width of 0.4 mm for all specimens.

3.2.3. Formation of Cracks under Sandwich Loading

In order to attain and keep the needed crack widths, sandwich test procedure was used as explained before in experimental study section. The procedure was applied to two specimens of each mixture. On non-fibrous specimens, cracks with a width of 0.4 mm were formed and maintained on test specimens as explained before. Load values required to form 0.4 mm cracks for these non-fibrous specimens were recorded and then applied to the fibrous specimens and the cracks formed were measured and maintained.

The reason for applying the load required to form 0.4 mm crack on non-fibrous specimens to fibrous specimens was to see the contribution of fibers on crack width bridging. So as previewed from flexural test results, fibrous specimens showed the ability to attain smaller crack widths under same load levels (Figure 4).

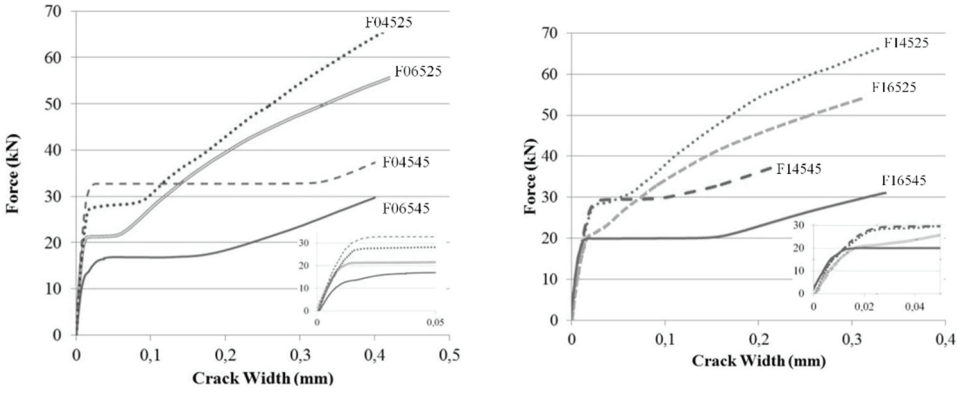

(a) (b)

Figure 4 - Force - crack width diagrams of specimens (a) without fibers and (b) with fibers.

It can be seen from Figure 4 that all fibrous specimens had smaller crack widths than their control specimens. This can be an early advantage for fibrous specimens before starting wetting - drying cycles. All cracks on the specimens were examined by naked eye and a magnifier (x10) and it was observed that there were one large and some very small distributed cracks on the specimens.

3.3. Corrosion Results

Corrosion tests were conducted for both cracked and uncracked specimens. Half-cell potential and corrosion rate measurements by using a galvanostatic pulse device were carried out for corrosion monitoring. For the first 60 weeks, 2 cracked specimens and 3 uncracked specimens were used. At the end of the 60 weeks period, 2 specimens (1 cracked and 1 uncracked) of each series were used for chloride content determination. Corrosion tests were continued until 80th week and again 2 specimens (1 cracked and 1 uncracked) of each series were used for chloride content determination.

- **Half-cell potential measurements**

Figure 5 and Figure 6, represent the half-cell potential values for uncracked and cracked specimens, respectively. The effects of various factors are seen when figures are examined. The results are interpreted based on limit values given in Table 3. The regions representing low and high risk of corrosion occurrence are separated for the attention of the readers.

Table 3 - Interpretation of half-cell potential values (ASTM C876 [33] /ASTM G3 [36])

Ag/AgCl (SSCE)	Interpretation
E > -83mV	Greater than 90% probability that no corrosion is occurring.
-233mV < E < -83mV	Corrosion activity is uncertain.
E < -233mV	Greater than 90% probability that corrosion is occurring.

The positive effects of water-to-cement ratio and cover thickness are easily seen in uncracked specimens (Figure 5). However, when Figure 5 is examined, it is seen that the advantage of using higher cover thickness is significantly decreased for cracked specimens. This is expected since the time needed for aggressive agents to penetrate into concrete to reinforcement decreased almost to zero when concrete cover was cracked. It should be emphasized that concrete was not only cracked but also under sustained loading, which resulted in a minimum crack width of approximately 0.22 and 0.40 mm for fibrous and non-fibrous specimens, respectively, for all times. The visual observations showed that, the crack directly went down to rebar when the crack widths given above were reached. The effect of water-to-cement ratio on half-cell potential results may also be considered secondary when concrete cover was cracked, since direct passage of aggressive agents to steel rebar was possible through the crack.

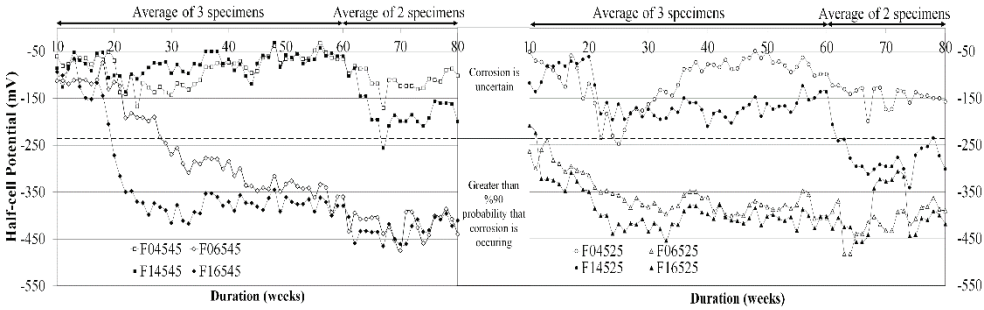

(a) (b)

Figure 5 - Half-cell potential values of uncracked specimens with a cover depth of (a) 45 mm, (b) 25 mm

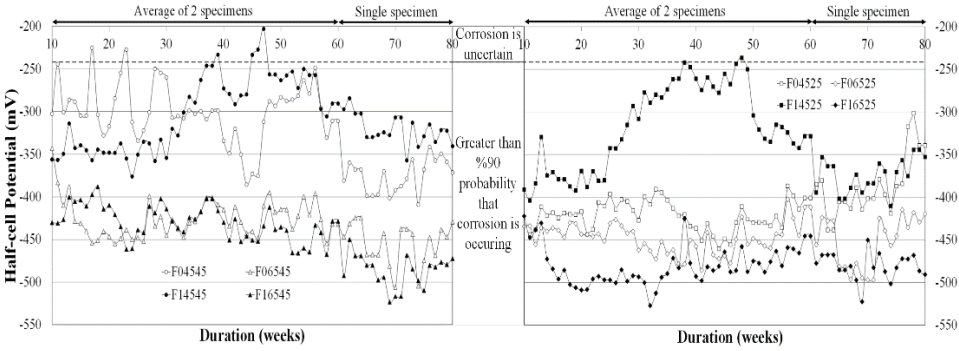

Figure 6 - Half-cell potential values of cracked specimens with a cover depth of (a) 45 mm, (b) 25 mm

It was observed that fibrous specimens yielded higher probability of corrosion occurrence especially in the uncracked state and this effect was more pronounced for low water-to-cement ratio specimens. This behavior may be explained by the existence of extra pores in fibrous specimens. Air contents of all mixes were measured by using pressure method immediately after mixing and the results showed that air contents of the fibrous mixes were higher when compared to non-fibrous mixes (Table 2). The expected positive effect of fibers was seen in the cracked state (Figure 6) for the specimens with low water-to-cement ratio (w/c: 0.45). Unfortunately, the same effect was not seen for high water-to-cement ratio specimens (w/c: 0.65). It is hypothesized that the positive effect of smaller crack width is reduced by the high permeability of the matrix.

Half – cell potential values are generally correlated with the time to depassivation as mentioned in Section 0. This gives an idea about corrosion initiation time for the specimens. Corrosion measurements began 10 weeks after exposure due to a breakdown in the galvanostatic pulse device as was mentioned in Section 0. A new series of uncracked specimens were cast and exposed to same wetting - drying cycles and the same corrosion monitoring procedure was applied to control the consistency of data obtained from the equipment. Results very similar to the data given in Figure 5 were obtained.

Based on the results, given in Figure 5 and obtained from latter produced specimens, corrosion initiation was not observed for the uncracked specimens produced using low water – to – cement ratio (0.45) at the end of 80 weeks of exposure (uncertain corrosion based on Table 3). However, corrosion initiation was observed earlier (from 10th week) on the rebars inside the uncracked specimens cast by using high water – to – cement ratio. For cracked specimens no extra specimens were cast since measurements showed corrosion initiation in the first 10 weeks. Therefore, corrosion was assumed to initiate immediately after NaCl exposure (based on very low half-cell potential values given in Figure 6). Later, the rebars were extracted from concrete specimens for visual examination of corrosion and for comparative checking of half-cell potential results.

4. CORROSION RATE MEASUREMENTS

Results of corrosion rate measurements are given in Figure 7 to Figure 10. The test results are presented separately for all mixtures for easy visualization by the readers. Corrosion rates were interpreted using Table 4 which was given by Frolund et al. [37]. Although, no standard table exists to interpret the corrosion rate data, Table 4 is found to be useful for evaluating the data obtained by using the equipment employed in this study. In evaluating the corrosion rate data, it should be kept in mind that the number of specimens dropped from 3 to 2 for the tests from 60 to 80 weeks. Therefore, degree of freedom in the data is decreased.

Table 4 - Interpretation of corrosion rate results [37].

I_{corr}	Interpretation
< 0.5μA/cm^2	Passive Areas
0.5–2 μA/cm^2	Negligible corrosion activity
2-5 A/cm^2	Low corrosion activity
5-15μA/cm^2	Moderate corrosion activity
>15μA/cm^2	High corrosion activity

Corrosion rate measurements of uncracked specimens are seen in Figures 7 and 8. Corrosion rates significantly increased when water-to-cement ratio was increased. No significant effect of fibers was observed on corrosion rate measurements of uncracked specimens.

The corrosion rate results of cracked specimens are given in Figures 9 and 10. The effect of water-to-cement ratio was important but less pronounced compared to uncracked specimens. Again, the effect of cover thickness was not pronounced. However, the effect of using fibers was more significant when concrete was cracked, since the crack opening is limited by fibers.

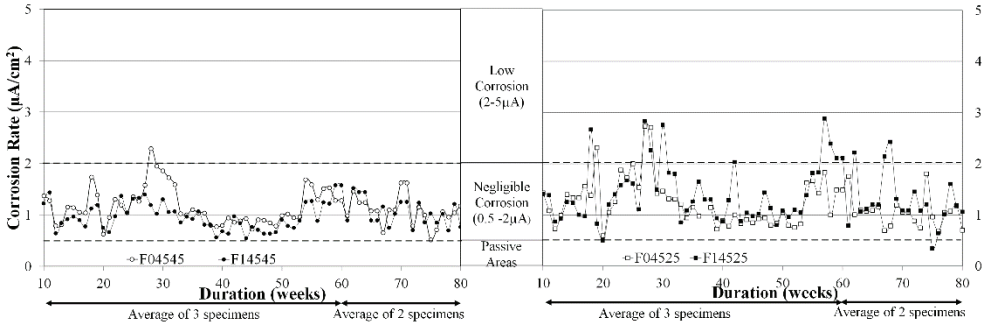

(a) (b)

Figure 7 - Corrosion rates of uncracked specimens with w/c ratio of 0.45 and a concrete cover of (a) 45 mm (b) 25 mm

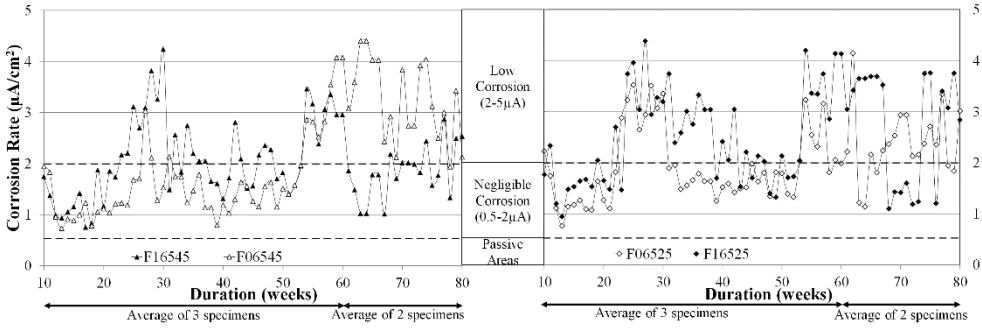

Figure 8 - Corrosion rates of uncracked specimens with w/c ratio of 0.65 and a concrete cover of (a) 45 mm (b) 25 mm.

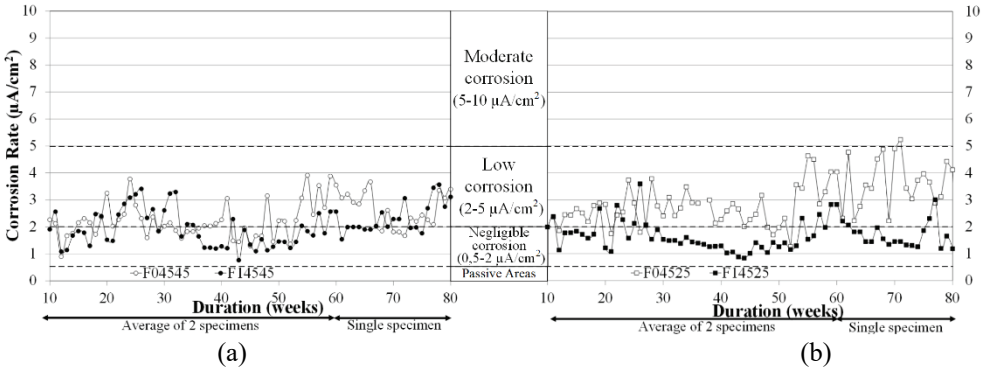

Figure 9 - Corrosion rates of cracked specimens with w/c ratio of 0.45 and a concrete cover of (a) 45 mm (b) 25 mm.

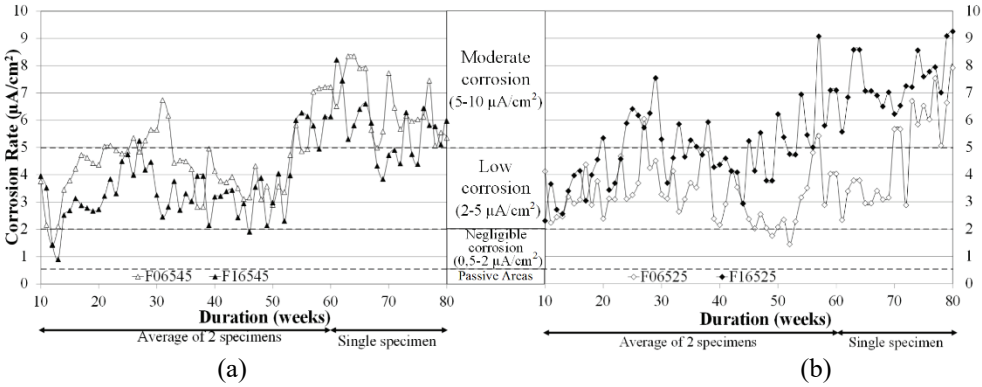

Figure 10 - Corrosion rates of cracked specimens with w/c ratio of 0.65 and a concrete cover of (a) 45 mm (b) 25 mm.

4.1. Chloride Penetration Results

Chloride penetration tests were conducted for all specimens at the end of wetting-drying period as explained in Section 0.

- **Chloride Profiles**

Chloride profiles of the specimens that were exposed to wetting-drying cycles for 80 weeks were given separately in Figure 11 - Figure 13.

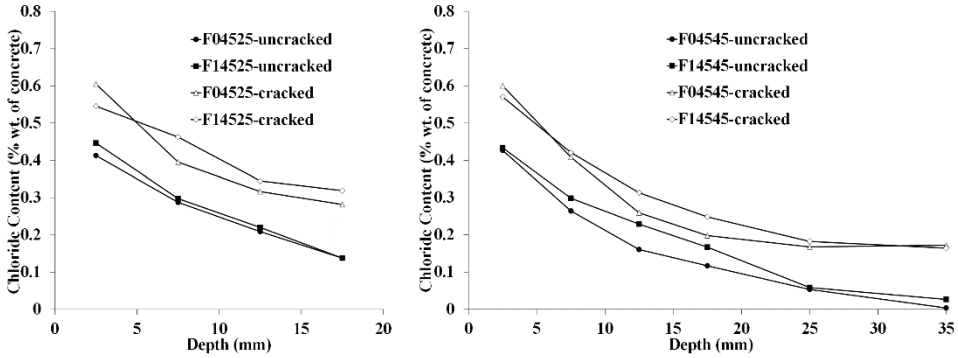

(a) (b)

Figure 11 - Effect of cracks and fibers on chloride penetration of specimens with a w/c ratio of 0.45 and a concrete cover of (a) 25 mm (b) 45 mm (after 80 weeks of exposure).

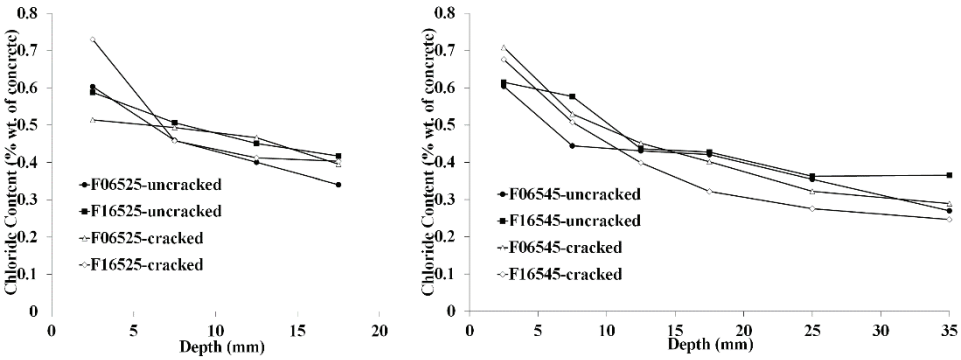

(a) (b)

Figure 12 - Effect of cracks and fibers on chloride penetration of specimens with a w/c ratio of 0.65 and a concrete cover of (a) 25 mm (b) 45 mm (after 80 weeks of exposure)

It was observed that cracks were more effective in increasing the diffusion of chloride ions at low water-to-cement ratio (0.45) concretes (Figure 11). However, the same effect was not

seen when water-to-cement ratio was increased to 0.65 (Figure 12), which was due to more porous microstructure of the high water-to-cement ratio concrete. Cover depth was found to be effective when low water-to-cement ratio mixes (0.45) were used (Figure 11). Chloride contents close to zero were observed for the uncracked specimens with a cover depth of 45 mm after 80 weeks of exposure. Same result was not valid for high water-to-cement ratio mixes. The effect of cover depth was almost negligible for high water-to-cement ratio mixes (0.65) even for uncracked specimens probably due to high permeability of concrete (Figure 12).

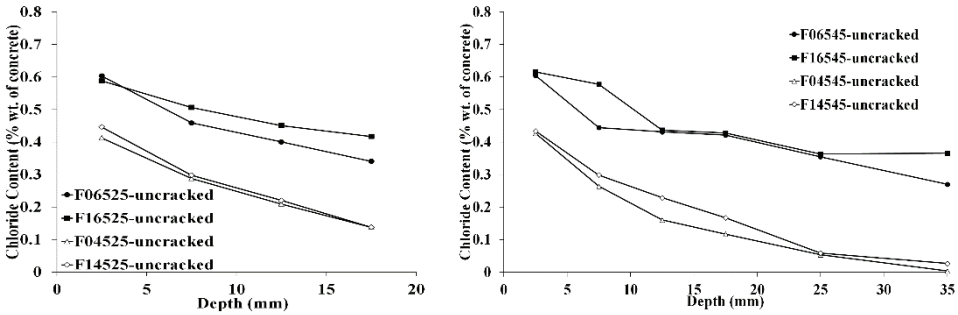

(a) (b)

Figure 13 - Effect of water-to-cement ratio and cover depth on chloride penetration of uncracked specimens with a concrete cover of a) 25 mm b) 45 mm (after 80 weeks of exposure).

The chloride penetration data is presented in Figure 13 to indicate the effect of water-to-cement ratio and cover depth after 80 weeks of exposure of uncracked specimens. It was observed that the water-to-cement ratio was the most pronounced parameter as mentioned above. Chloride penetration was increased greatly with an increased water-to-cement ratio even in the uncracked state due to increased porosity and thus permeability of the concrete. Effectiveness of greater cover depth was also observed for 80 weeks of exposure of lower water-to-cement ratio concretes.

- **Diffusion Coefficients**

Diffusion coefficients and % chloride content values at the rebar level for all the specimens were predicted by using 2nd Fick's law and given in Table 5.

As seen from the Table 5, diffusion coefficients and chloride contents are more compatible for uncracked specimens compared to cracked specimens. For the cracked specimens % chloride concentrations were found to be higher on top of the rebar; whereas surprisingly for some of the cracked specimens this high % chloride concentration values were not accompanied by high diffusion coefficients. This is probably because of the change of transport mechanism of chloride ions with the existence of cracks. Change of transport mechanism with formation of cracks was also mentioned by several other researchers [7,38].

Based on the results of this study and literature [7] it can be said that, calculating the diffusion coefficient by using Fick's second law of diffusion may be misleading for cracked specimens since diffusion is not the only active mechanism for these specimens.

Table 5 - Diffusion coefficients and chloride concentrations on rebar level (calculated using Fick's 2nd law).

		w/c : 0.45			w/c : 0.65	
	Code	D (10^{-12} m^2/s)	Cl cont. (% by weight of concrete)	Code	D (10^{-12} m^2/s)	Cl cont. (% by weight of concrete)
Uncracked	F04525	2.80	0.060	F06525	7.51	0.222
	F04545	1.99	0.001	F06545	23.24	0.197
	F14525	2.56	0.056	F16525	17.20	0.328
	F14545	3.11	0.005	F16545	30.01	0.246
Cracked	F04525	4.14	0.134	F06525	32.18	0.356
	F04545	4.72	0.021	F06545	14.03	0.150
	F14525	7.39	0.205	F16525	6.12	0.221
	F14545	6.67	0.044	F16545	10.20	0.099

Therefore, using diffusion coefficient as the only parameter while analyzing the corrosion potential of cracked concrete specimens may be misleading since true diffusion can't be observed in these specimens.

3.5. Visual Observation of Corrosion on Rebars

All of the rebars taken out of the specimens after 60 and 80 weeks of exposure were visually examined and surface images were taken. Images of rebars after 80 weeks of exposure are given below for comparing the experimentally obtained results (half cell potential, I_{corr}, C_s, D and concentration values) with the exact corrosion states of rebars (Figure , Figure 1). Following comments can be made if Figure 14 and Figure 1 are carefully examined.

For the specimens with a water-to-cement ratio of 0.45, experimental data obtained using galvanostatic pulse technique were found to be in accordance with the observations made on the rebars taken out of the specimens. If Figure is examined together with the experimental values given, it is seen that, based on the classification given by ASTM C876 [30], no signs of corrosion were observed on the specimens that represented half-cell potential values in the "uncertain corrosion activity zone" (uncracked specimens cast using a water-to-cement ratio of 0.45 – except F14525). The corrosion rate of these specimens was also found in the "negligible corrosion activity" zone when Table 4 is examined. For all of the cracked specimens, half-cell potential values were assessed in the corrosion occurrence zone (> 90%). Corrosion rates of these specimens were found in the "low corrosion activity zone" except

F14525. In compliance with this result some corrosion was observed on all of the rebars taken out of these specimens except F14525.

For the specimens with a water-to-cement ratio of 0.65, again comparable results are seen between the corrosion observations and the experimental data. Corrosion activity was found on different parts of the rebars (as can be seen on the figure) and this is attributed to the high permeability of concrete. It is hypothesized that the solution may be diffused through different parts of concrete resulting in corrosion. It should be emphasized that only a part of the rebar beneath the ponding area was monitored for corrosion rate measurements. It is seen from the figure that this method of measurement, may be misleading for high permeability concretes, since harmful substances may diffuse through different parts of concrete resulting in corrosion on the regions which are not monitored. This phenomenon was observed on almost all of the uncracked specimens cast by using w/c of 0.65. This was not an issue for the cracked specimens, since solution directly reached to the rebar through the crack.

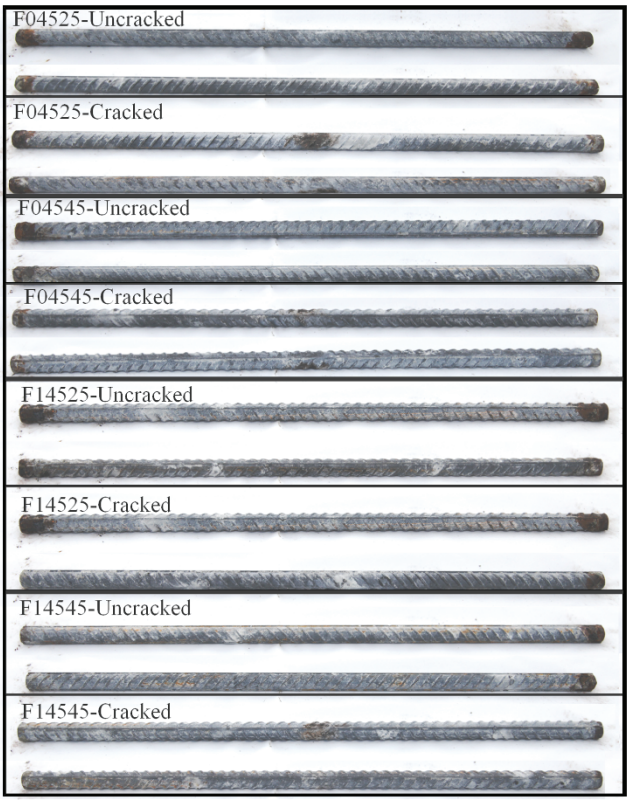

Half-Cell	I_{corr}	C_s	D	%conc
-219.14	1.29	0.462	2.80	0.060

Half-Cell	I_{corr}	C_s	D	%conc
-339.27	4.12	0.632	4.14	0.134

Half-Cell	I_{corr}	C_s	D	%conc
-191.62	1.11	0.481	1.99	0.001

Half-Cell	I_{corr}	C_s	D	%conc
-371.48	3.40	0.592	4.72	0.021

Half-Cell	I_{corr}	C_s	D	%conc
-309.41	1.27	0.500	2.56	0.056

Half-Cell	I_{corr}	C_s	D	%conc
-352.91	1.18	0.585	7.39	0.205

Half-Cell	I_{corr}	C_s	D	%conc
-186.45	1.21	0.479	3.11	0.005

Half-Cell	I_{corr}	C_s	D	%conc
-340.76	3.11	0.569	6.67	0.044

Figure 14 - Images of corroded rebars taken out of specimens with a water-to-cement ratio of 0.45.

Half-Cell	I_{corr}	C_s	D	%conc
-393.12	1.41	0.629	7.51	0.222

Half-Cell	I_{corr}	C_s	D	%conc
-419.68	7.92	0.544	32.18	0.356

Half-Cell	I_{corr}	C_s	D	%conc
-411.45	1.00	0.574	23.24	0.197

Half-Cell	I_{corr}	C_s	D	%conc
-467.45	3.25	0.675	14.03	0.150

Half-Cell	I_{corr}	C_s	D	%conc
-433.32	4.04	0.607	17.20	0.328

Half-Cell	I_{corr}	C_s	D	%conc
-490.69	9.25	0.725	6.12	0.221

Half-Cell	I_{corr}	C_s	D	%conc
-398.76	2.31	0.608	30.01	0.246

Half-Cell	I_{corr}	C_s	D	%conc
-472.35	5.96	0.650	10.20	0.099

Figure 15 - Images of corroded rebars taken out of specimens with a water-to-cement ratio of 0.65.

5. CONCLUSIONS

Following conclusions were drawn from this comprehensive experimental study on the effects of chloride-induced corrosion on cracked and uncracked reinforced concrete.

1. Water-to-cement ratio was found to be the most effective parameter in the uncracked state. No corrosion was measured or observed on the rebars extracted from the specimens cast using a water-to-cement ratio of 0.45 after 80 weeks of exposure. Corrosion was found to initiate from 10-20 weeks for the uncracked specimens with high water-to-cement ratio of 0.65.

2. The positive effect of low water-to-cement ratio decreased in the cracked state. NaCl solution might have directly reached to the rebar through the open crack (0.3-0.4 mm) surpassing concrete cover resulting in an immediate corrosion initiation.

3. Increased cover depth was effective only for concretes with low water-to-cement ratio in the uncracked state. Increasing cover depth was not effective in reducing the rate of corrosion in high water-to-cement ratio and cracked concretes.

4. Fibers were not effective in the uncracked state where slightly higher corrosion was even observed, most probably due to higher air content measured in the fibrous specimens.

5. Positive effects of fibers were seen in the cracked concretes for low water-to-cement ratio mixes. No clear effect was observed when high water-to-cement ratio mixes were used.

6. Chloride contents (%) and diffusion coefficients were compatible for uncracked specimens which was not the case for cracked specimens. Diffusion is not the dominating mechanism for cracked concretes, where cracks are providing direct passage to the rebar for harmful substances.

7. Visual observations were in accordance with the results obtained from half-cell potential and corrosion rate measurements, except for the uncracked specimens with high water-to-cement ratio which showed corrosion on different parts of the rebar instead of the monitored ponding area (middle section). Chloride containing solution might have easily diffused in all directions through the material owing to high permeability of the matrix resulting in corrosion on different parts of rebars. However, this was not represented by corrosion rate measurements since only middle section of the rebar was examined in the scope of the test.

8. There is no agreement on the maximum allowable crack width in the standards. The results of this study showed how the protection provided by low water-to-cement ratio and high cover depth is to be questioned when crack widhts up to 0.3 to 0.4 mm exist on the concrete surface. This implies the importance of having a concrete surface free from cracks and/or the regular control/maintenance procedures of concrete surfaces for protection against corrosion.

Acknowledgement

The authors gratefully acknowledge the financial support of TUBITAK (110M-264). They also would like to thank to AKÇANSA Cement, BASF-YKS Construction Chemicals and LIMAK Construction for providing materials used to produce specimens and Boğaziçi University Construction Materials Lab. personnel Ümit Melep for his most sincere efforts during experiments.

References

[1] Rodriguez O.G., Hooton R.D., Influence of cracks on chloride ingress into concrete, *ACI Materials Journal*, 100(2), 120-126, 2003.

[2] Win P.P., Watanabe M., Machida A., Penetration profile of chloride ion in cracked reinforced concrete, *Cement and Concrete Research*, 34, 1073-1079, 2004.

[3] Marsavina L., Audenaert K., Schutter G.D., Faur N. and Marsavina D., Experimental and numerical determination of the chloride penetration in cracked concrete, *Construction and Building Materials*, 23, 264-274, 2009.

[4] Gowripalan N., Sirivivatnanon V. and Lim C., Chloride diffusivity of concrete cracked in flexure, *Cement and Concrete Research*, 30, 725-730, 2000.

[5] Schiessl P., Raupach M., Laboratory studies and calculations on the influence of crack width on chloride induced corrosion of steel in concrete, *ACI Materials Journal*, 94(1), 56-62, 1997.

[6] Song H.W., Lee C.H., Ann. K.Y., Factors influencing chloride transport in concrete structures exposed to marine environments, *Cement Concrete Composites*, 30, 113-121, 2008.

[7] Boulfiza M., Sakai K., Banthia N., Yoshida H., Prediction of chloride ions ingress in uncracked and cracked concrete, *ACI Materials Journal*, 100(1), 38-48, 2003.

[8] Aldea C. M., Shah S. P., Karr A., Permeability of cracked concrete, *Materials and Structures*, 32, 370-376, 1999.

[9] Djerbi A., Bonnet S., Khelidj A., Baroghel-bouny, V., Influence of traversing crack on chloride diffusion into concrete. *Cement and Concrete Research*, 38, 877-883, 2008.

[10] Wang K., Jansen D.C., Shah S.P., Karr A.F., Permeability study of cracked concrete, *Cement and Concrete Research*, 27, 381-393, 1997.

[11] Sahmaran M., Effect of flexure induced transverse crack and self-healing on chloride diffusivity of reinforced mortar, *Journal of Materials Science*, 42, 9131-9136, 2007.

[12] Wang H., Lu C., Jin W., Bai Y., (2001) Effect of external loads on chloride transport in concrete, *Journal of Materials in Civil Engineering*, 23(7), 1043-1099, 2011.

[13] Papa N.F., Yinghua Y., Bo D., Effects of crack width on chloride penetration and performance deterioration of RC columns with sustained eccentric compressive load, *KSCE Journal of Civil Engineering*, 22(2), 637-646, 2018.

[14] Chunhua L, Jinmu Y, Hui L, Ronggui L., Experimental studies on chloride penetration and steel corrosion in cracked concrete beams under drying-wetting cycles, *Journal of Materials in Civil Engineering*, 29(9), 2017:04017114.

[15] Beeby A., Corrosion of reinforcing steel in concrete and its relation to cracking, *Structural Engineer Part A*, 56A(3), 77-81, 1978.

[16] Arya C. and Ofori-Darko F.K., Influence of crack frequency on reinforcement corrosion in concrete, *Cement and Concrete Research*, 26(3), 345-353, 1996.

[17] Mohammed T.U., Otsuki N., Hamada H., Oxygen permeability in cracked concrete reinforced with plain and deformed bars, *Cement and Concrete Research*, 31, 829-834, 2001.

[18] Mohammed T.U., Otsuki N., Hisada M., Shibata T., Effect of crack width and bar types on corrosion of steel in concrete, *Journal of Materials in Civil Engineering*, 13, 194-201, 2001.

[19] Ye H., Jin N., Jin X. and Fu C., Model of chloride penetration into cracked concrete subject to drying-wetting cycles, *Construction and Building Materials*, 36, 259-269, 2012.

[20] Otieno M, Beushausen H, Alexander M., Towards incorporating the influence of cover cracking on steel corrosion in RC design codes: the concept of performance-based crack width limits, *Materials and Structures*, 45, 1805-1816, 2012.

[21] Berrocal C.G., Löfgren I., Lundgren K, Tang L, Corrosion initiation in cracked fiber reinforced concrete: Influence of crack width, fiber type and loading conditions, *Corrosion Science*, 98, 128-139, 2015.

[22] Zafar I, Sugiyama T, The influence of bending crack on rebar corrosion in fly ash concrete subjected to different exposure conditions under static loading, *Construction and Building Materials*, 160, 293-307, 2018.

[23] Yongsheng J, Yijie H, Lingle Z, Zhongzheng B, Laboratory studies on influence of transverse cracking on chloride induced corrosion rate in concrete, *Cement and Concrete Composites*, 69, 28-37, 2016.

[24] Sangoju B, Gettu R, Bharatkumar B.H, Neelamegam M, Chloride induced corrosion of steel in cracked OPC and PPC concretes: Experimental study, *Journal of Materials in Civil Engineering*, 23(7), 1057-1066, 2011.

[25] Granju J.L., Balouch S.U., Corrosion of steel fiber reinforced concrete from the cracks, *ACI Materials Journal*, 35, 572-577, 2005.

[26] Berrocal C.G., Lundgren K., Lofgren I., Influence of steel fibers on corrosion of reinforcement in concrete in chloride environments: A review, *Fiber Concrete 2013*, Prague, Czech Republic, Sept. 12-13, 2013.

[27] Hay R, Ostertag C.P, Influence of transverse cracks and interfacial damage on corrosion of steel in concrete with and without fiber hybridization, *Corrosion Science*, 153, 213-224, 2019.

[28] ACI Committee 224R., Control of cracking in concrete structures, *ACI 224-01*, American Concrete Institute, Detroit, Michigan, 2001.

[29] ACI Committee 318, (2008) Building code requirements for reinforced concrete, *ACI 318-08*, American Concrete Institute, Detroit, Michigan, 2008.

[30] Bentur A., Diamond S., Berke N.S., Steel corrosion in concrete: Fundamentals and civil engineering practice, *E & FN Spon*, London, United Kingdom, 1997.

[31] Baah P., Cracking behavior of structural slab bridge decks, *Ph.D. Thesis*, University of Akron, Ohio, 2014.

[32] ASTM Standard C39/C39M, Standard test method for compressive strength of cylindrical concrete specimens, *ASTM International*, West Conshohocken, PA., 2014.

[33] ASTM Standard C876, Standard test method for corrosion potentials of uncoated reinforcing steel in concrete, *ASTM International*, West Conshohocken, PA, 2015.

[34] ASTM Standard C1556. Standard test method for determining the apparent chloride diffusion coefficient of cementitious mixtures by bulk diffusion, *ASTM International*, West Conshohocken, PA., 2017.

[35] ASTM Standard C1152., Standard test method for acid-soluble chloride in mortar and concrete, *ASTM International*, West Conshohocken, PA.,2012

[36] ASTM Standard G3, Standard practice for conventions applicable to electrochemical measurements in corrosion testing, *ASTM International*, West Conshohocken, PA, 2017

[37] Frolund T., Klinghoffer O., Poulsen E., Rebar corrosion rate measurements for service life estimates, *ACI Fall Convention*, Toronto, Canada, 2000.

[38] Gerard B., Marchand J., Influence of cracking on the diffusion properties of cement-based materials Part I: Influence of continuous cracks on the steady-state regime, *Cement and Concrete Research,* 30, 37-43, 2000.

Teknik Dergi, 2020 10339-10358, Paper 593

Effect of Modeling Beam-Column Joints on Performance Assessment of Columns in Non-Ductile RC Frames

Sadık Can GİRGİN[1]

ABSTRACT

Seismic performance evaluation of non-seismically detailed reinforced concrete (RC) buildings requires proper analytical modeling approaches for beam-column joints which are most vulnerable parts. This study investigates the influence of beam column joint modeling assumptions on performance evaluation of non-ductile RC buildings. Numerical simulation model includes truss-based elements for beam-column connections and fiber-based elements for beams and columns. Two-dimensional four- and six- story reinforced concrete frames of an existing RC building are designed and analyzed by conducting incremental dynamic analyses. Column chord rotations and corresponding strains are compared with code provisions for performance assessment of non-ductile RC frames.

Keywords: Beam-column joints, non-ductile frames, hybrid model, performance limits.

1. INTRODUCTION

Beam-column joints in reinforced concrete (RC) buildings are expected to transfer flexure and shear forces without significant strength and stiffness degradation in modern construction practice. However, older-type RC buildings constitute a significant portion of the building inventory designed only considering gravity loads before 1970's in earthquake-prone regions (Figure 1a). Field observations after earthquakes revealed that brittle failure modes may occur at the vicinity of beam-column joints in reinforced concrete frames those non-conforming the design requirements. Observed failure modes in RC beam-column joints are reported due to non-seismic detailing such as insufficient anchorage of beam rebars, lack of transverse reinforcement in the joint and discontinuity of beam and column rebars (Figure 1b). There has been a significant amount of experimental research on cyclic behavior of exterior beam- column joints with respect to axial load ratio, transverse reinforcement ratio, anchorage detailing of beam rebars and drift histories [1-5]. Bedirhanoğlu et al. (2010) [6] tested exterior beam-column joints representing construction practice deficiencies in Turkey before 1970's. Main test variables were the effect of displacement history, axial load, presence of transverse beam in the joint and amount of joint reinforcement. They concluded

Note:
- This paper has been received on September 3, 2018 and accepted for publication by the Editorial Board on May 30, 2019.
- Discussions on this paper will be accepted by January 31, 2021.
- https://dx.doi.org/10.18400/tekderg.456752

1 Dokuz Eylul University, Department of Civil Engineering, İzmir, Turkey - sadik.girgin@deu.edu.tr - https://orcid.org/0000-0002-5224-3122

that presence of lateral beam didn't have significant effect on bond of reinforcing bars in the joint. Gökdemir and Tankut (2017) [7] tested 4 reference and 7 strengthened exterior beam-column joints with diagonal steel bars. Reference specimen without shear reinforcement showed significant strength degradation at small drifts. On the other hand, for interior beam-column joints without transverse reinforcement, significant stiffness degradation will occur due to insufficient development length of beam longitudinal bars [8]. Interior beam-column joint specimens were tested by Alire (2002), and damages were observed with a combination of bond-slip of reinforcing bars and shear cracks in the joint [9].

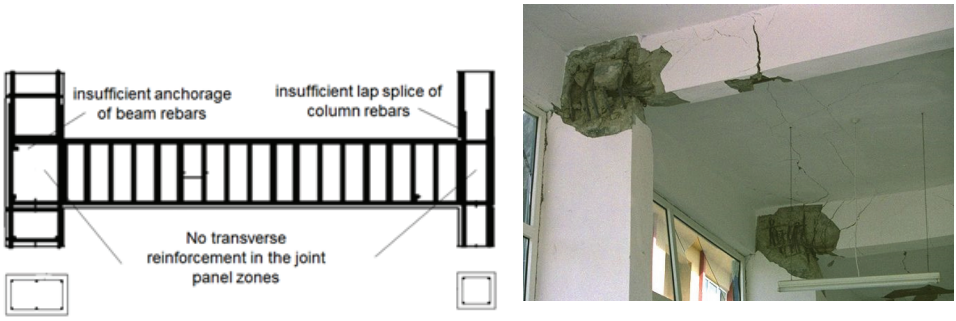

(a) (b)

Figure 1 - (a) Typical detailing of beam-column connections built before 1970's, (b) Damage to beam-column joint from August 17, 1999 Kocaeli Earthquake (nisee.berkeley.edu)

Although beam-column joints characterize the seismic behavior of existing RC buildings, rigid joint assumption is generally considered in design-oriented analyses [10]. Analytical models ignoring joint flexibility using rigid joint assumption may lead to underestimation in damage levels of RC members [11]. Hence, seismic performance assessment of existing RC buildings requires refined analytical tools accounting for damage states of non- seismically detailed beam-column joints. Modeling approaches for numerical simulation of beam-column joints can be classified as (i) lumped plasticity models, (ii) distributed plasticity (fiber-based) models, and (iii) truss-based models. Lumped plasticity models are employed to simulate nonlinear behavior of structural elements with concentrated nonlinearities in a finite length. Zero-length rotational springs or moment-curvature relations within a specified length, which follow nonlinear hysteretic rules, can be assigned to the ends of beam-column elements [12-15]. These models also include springs representing shear, bond slip and rigid links at the vicinity of the connection [11, 15-18]. Distributed plasticity models with fiber-based beam-column elements provide sufficient estimation for local response parameters such as curvature and strains. Element cross section is discretized into fibers at integration points along the element length. Force-based formulation for nonlinear beam-column elements has advantages over the displacement-based formulation, because equilibrium is satisfied at each section and end node for force interpolation function [19].

Truss-based modeling approaches have been studied for design and analysis of RC members subjected to shear, flexure and axial forces [20-23]. Panagiotou et al. (2012) [24] improved

existing truss modeling approaches by including mesh size effects and biaxial effects for diagonal elements in compression. Moharrami et al. (2015) [25] enhanced the truss model for analysis of shear-critical RC columns including the contribution of aggregate interlock effects. Bowers (2014) [26] and Xing et al. (2018) [27] proposed a hybrid numerical model for beam-column joints of non-ductile frames including nonlinear cyclic truss model for connection region and distributed plasticity model for beams and columns.

This study investigates the influence of beam column joint modeling assumptions on performance evaluation of non-ductile RC frames. For this purpose, a hybrid analytical model is validated by using test results of exterior beam-column joint specimens representing joints in existing buildings. Two-dimensional structural models of four- and six- story buildings were modeled using the hybrid model and analyzed by incremental dynamic analyses. Rotation-based and strain-based performance limits of RC members are investigated and compared with the code provisions.

2. NUMERICAL SIMULATION OF BEAM-COLUMN JOINTS

2.1. Numerical Simulation Model

In this study, all numerical analyses are performed by using OpenSees computer program [28]. Bowers (2014) [26] proposed a numerical simulation model for shear critical interior and exterior beam-column joints and validated cyclic behavior of joint tests representing existing buildings. The numerical model includes nonlinear cyclic truss model for connection region and distributed plasticity model for beams and columns as shown in Figure 2. Nonlinear truss model is established by assignment of location of horizontal elements including longitudinal rebars for beams and diagonal element angles. Truss model herein uses elements in the horizontal, vertical and diagonal directions representing steel reinforcement and concrete areas. Nonlinear concrete trusses for diagonal elements account for biaxial effects on the compression behavior while tension stiffening effects are considered in the vertical and horizontal directions. Nonlinear force-based beam-column elements with Gauss-Lobatto quadrature and two integration points with linear transformation are used for beams and columns.

2.2. Material Models

Giuffré-Menegotto-Pinto (GMP) steel material model is used to define the stress-strain relationship for the reinforcing steel. A GMP model is shown in Figure 3, where f_y is the yield strength, the corresponding yield strain ε_y, E_s the elastic modulus, and B_s the post-yield hardening ratio – the monotonic envelope for this material model is bilinear.

The stress-strain law for concrete proposed by Lu and Panagiotou (2014) [29] which is schematically presented in Figure 4 where f_c' is the compressive strength at ε_0=0.2% strain for unconfined concrete. Ultimate strain (ε_u) of concrete is adjusted by accounting for the mesh-size effects due to the procedure outlined by Lu and Panagiotou (2014) [29]. For horizontal and vertical concrete truss elements, tensile strength is $f_t = 0.33\sqrt{f_{ck}}\,(MPa)$ with a softening portion in accordance with tension stiffening by Stevens et al. (1991) [30]:

$$f = f_t\left[(1-M)e^{-\lambda_t(\varepsilon-\varepsilon_{cr})}+M\right] \tag{1}$$

$$M = C_t\frac{\rho_l}{d_b} \tag{2}$$

$$\lambda_t = \frac{540}{\sqrt{M}} \tag{3}$$

where ρ_l is steel ratio in the horizontal and vertical truss elements, M is tension stiffening parameter, d_b is rebar diameter and C_t = 75 mm.

The concrete material model for the diagonal elements considers for the reduction of compressive strength due to transverse strains described by Vecchio and Collins (1986) [31]. Compressive stresses are multiplied by a reduction coefficient (β) at each analysis step based on calculated transverse strains using fictitious strain gauge elements. Figure 5 shows the relation between stress reduction factor, β, and normal strain, ε_n. The values of β_{int} = 0.3 and β_{res} = 0.1 are considered for the analyses.

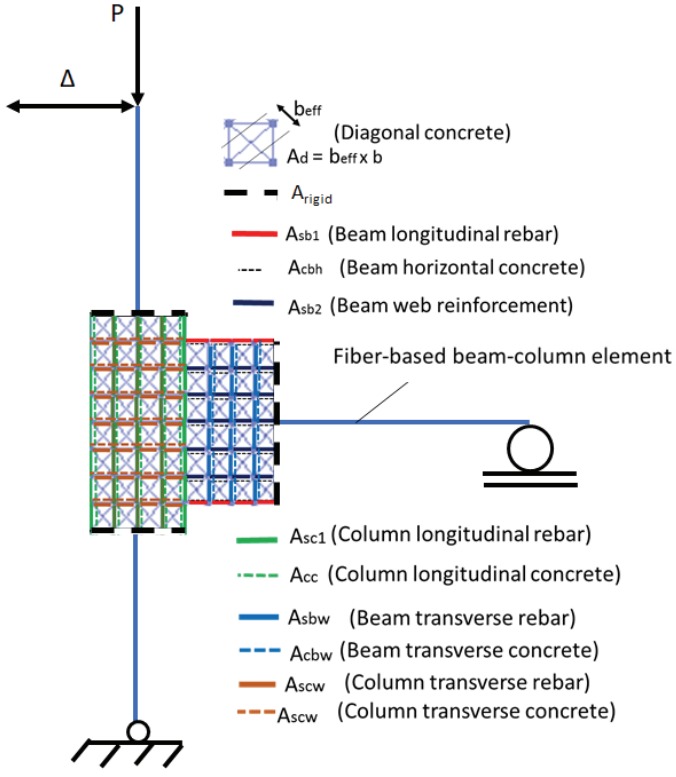

Figure 2 - Numerical simulation model for an exterior beam-column joint

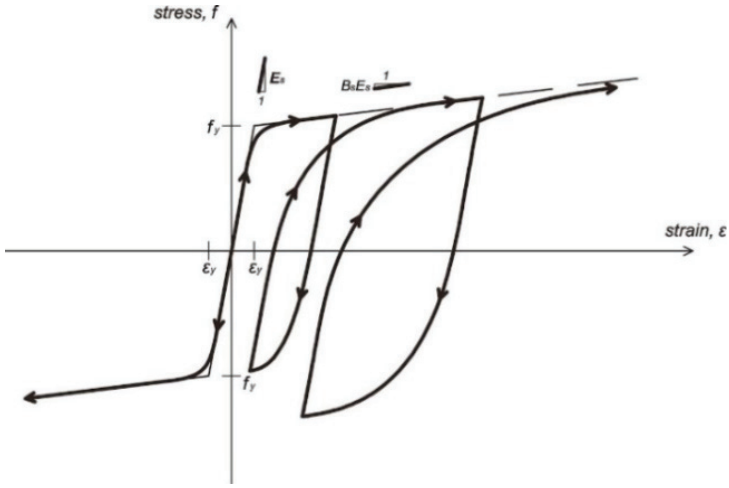

Figure 3 - Stress-strain relationship of the GMP steel material model

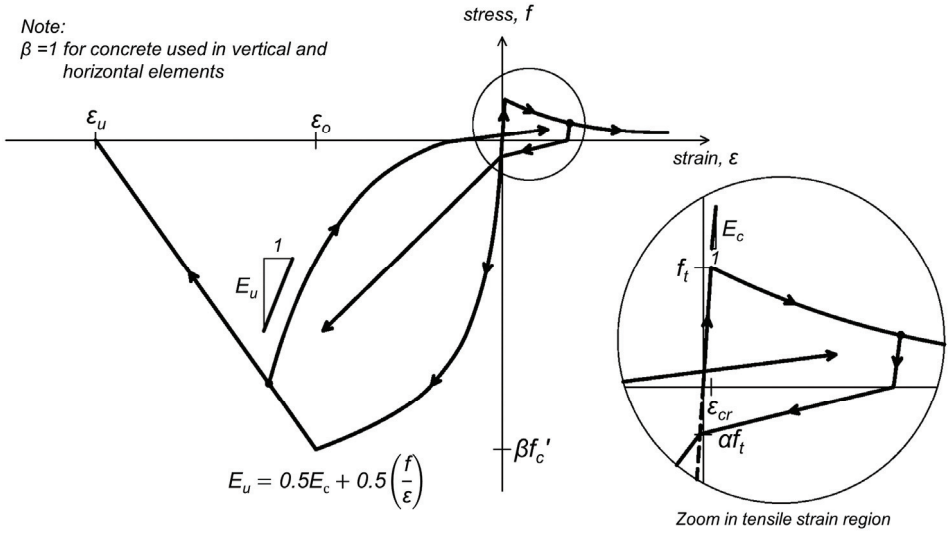

Figure 4 - Stress-strain relationship of concrete material models [29].

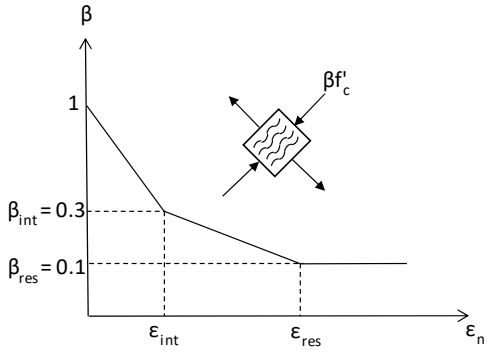

Figure 5 - Relation between reduction factor and normal strain

3. CASE STUDIES

Experimental research studies on non-seismically detailed beam-column joints conducted by Mısır and Kahraman (2013) [32] and Pantelides et al. (2002) [33] are considered in this study. Geometry and reinforcing details of 2/3 scale S1 specimen [32] and full-scale Unit 4 [33] are shown in Figure 6. One reference (S1) and two exterior beam-column joints strengthened with SIFCON blocks were tested by Mısır and Kahraman (2013) [32]. For S1 specimen, average concrete strength was 10 MPa for beam-column joint at the test day. Beam and column longitudinal rebars with 8- and 10-mm diameters had 402 MPa and 411 MPa yield strengths, respectively. Axial load was applied under 15% of column axial load capacity during cyclic reversals. Lateral cyclic displacements were applied at the top of the column with increasing amplitude from 0.15% to 3.5% drift ratios. During the test, first flexural and diagonal cracks were observed at 0.15% and 0.75% drift ratios, respectively. Shear cracks increased and expanded in the joint panel at 1% drift ratio. At 1.75% drift ratio, concrete cone developed, detached from the specimen and severe pinching was observed following 0.75% drift ratio due to shear deformations. Lateral strength of the specimen was reached at 0.5% drift ratio and test was continued up to third the cycle of 3.5% drift ratio at which specimen showed heavily damage state.

Figure 7 shows the hybrid models with different mesh sizes as Model-A and Model-B for beam-column joint specimen (S1). Nonlinear concrete trusses in the vertical and horizontal directions account for tension stiffening effects. Inclination angle of diagonal elements with respect to horizontal axis is considered as 46^0. Nonlinear truss model is connected to force-based beam-column elements with rigid elements as shown in Figures 7 (a) and (b). The lateral force– displacement responses for experimentally measured and cyclically computed using numerical simulation model are compared in Figure 8 (a) and (b). Both models computed stiffness degradation as well as pinching in a good agreement with cyclic behavior of specimen (Figure 8c) and the failure mode is captured with the diagonal concrete crushing.

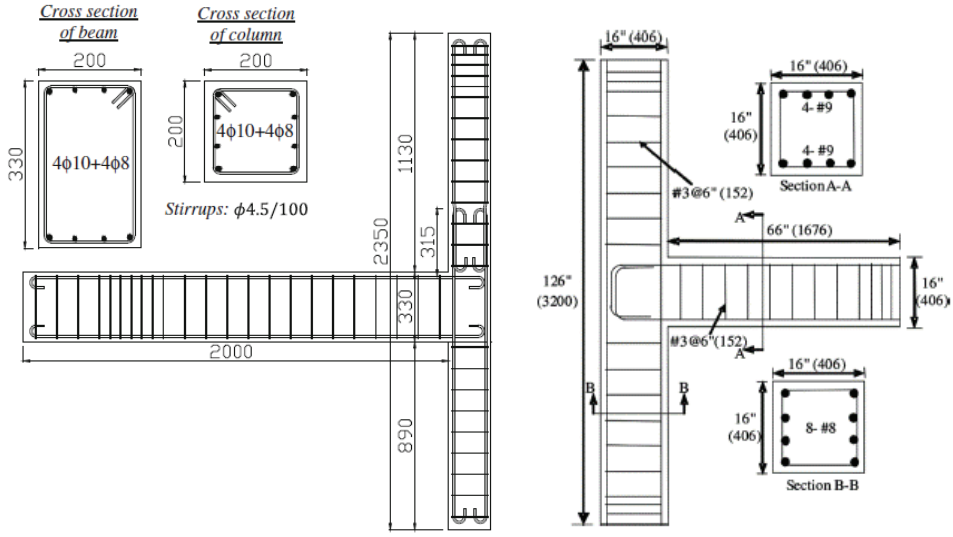

(a) (b)

Figure 6 - Geometry and reinforcing details of unreinforced beam- column joint for (a) S1 specimen tested by Mısır and Kahraman [32], and (b) Unit 4 tested by Pantelides et al. [33]

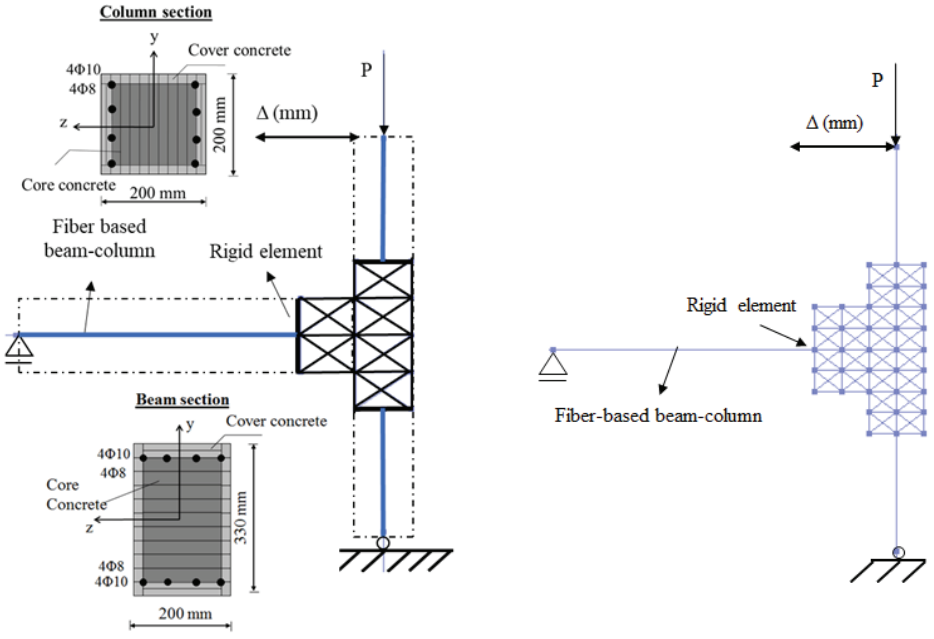

(a) (b)

Figure 7 - Numerical simulation models for S1 specimen (a)Model A and (b) Model B

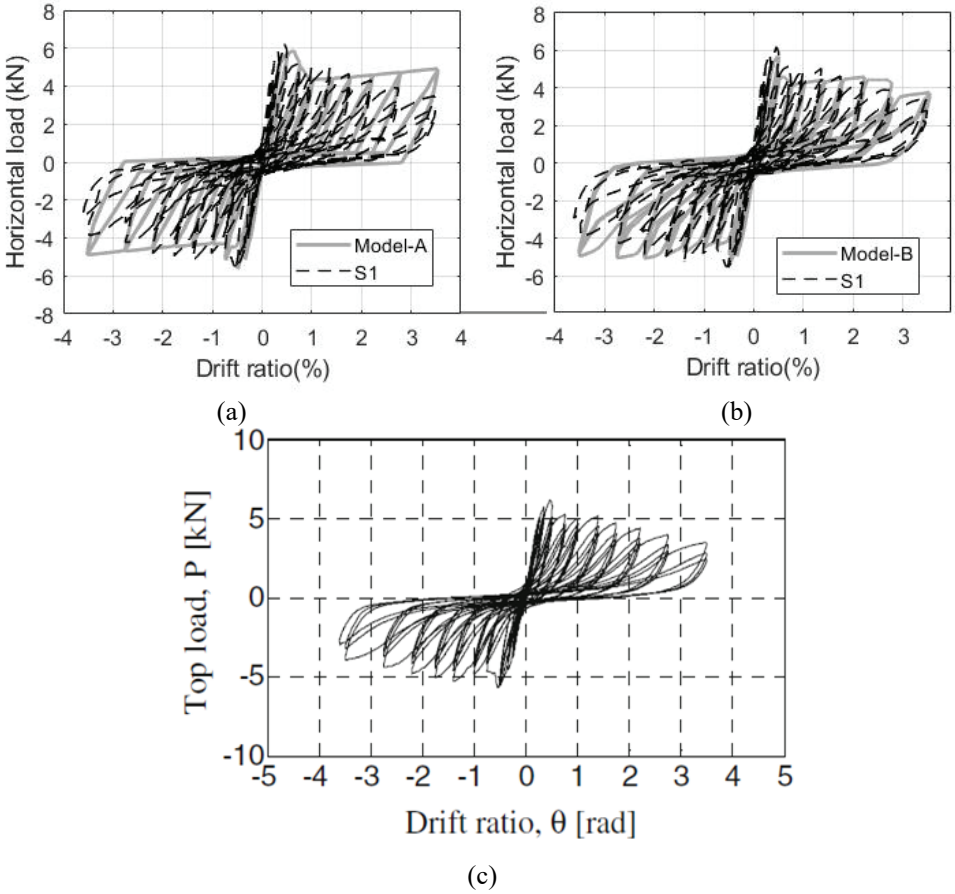

Figure 8 - Comparison of measured and computed responses for S1 specimen and (a) Model-A, and (b) Model-B and (c) lateral load-drift ratio relationships for S1 specimen [32]

Pantelides et al. (2002) [33] tested six exterior full-scale beam-column joints with different details of beam reinforcement and axial load ratios. For Unit-4 specimen shown in Figure 6b, average concrete strength was 31.6 MPa at the test day and beam and column longitudinal rebars with 25- and 29-mm diameters had 469 MPa and 458.5 MPa yield strengths, respectively. Axial load was applied under 25% of column axial load capacity during cyclic reversals. During the test, first yield in longitudinal reinforcement was observed and initial significant cracking in the joint was observed at at 0.5% and 1.5% drift ratios, respectively. Shear cracks increased and expanded in the joint panel at 2% drift ratio. At 5% drift ratio, significant spalling in concrete occurred. Figure 9 (a) shows the hybrid models for Unit-4 beam-column joint specimen tested by Pantelides et al. [33]. The lateral force– displacement responses for measured and monotonically and cyclically computed using numerical simulation model are compared in Figure 9(b). The failure mode observed in the case study

is captured with the diagonal concrete crushing. The peak strength in numerical model is 1.2 times the experimentally measured.

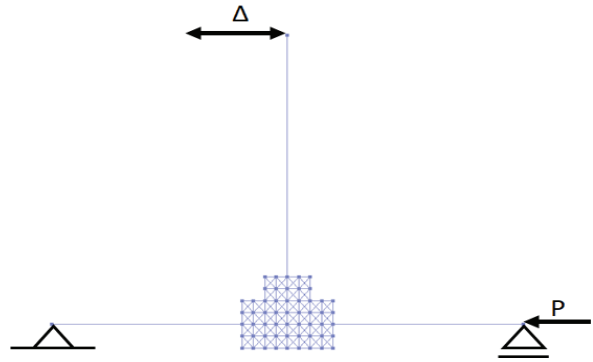

(a)

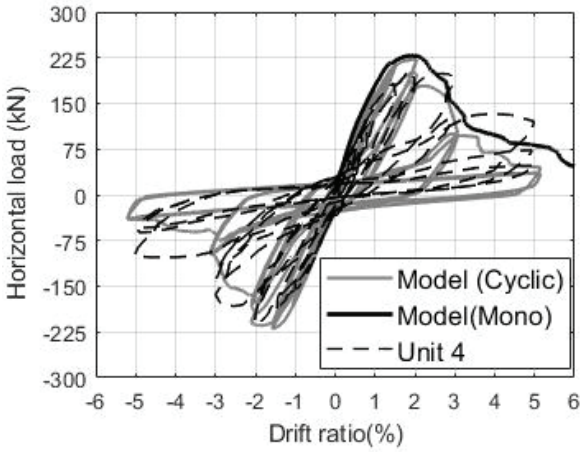

(b)

Figure 9 - (a) Numerical simulation model, and (b) Comparison of measured and computed responses for Unit 4 specimen (Pantelides et al., 2002) [33].

4. ANALYSIS OF FRAME STRUCTURES

Seismic performance of existing reinforced concrete buildings with unreinforced beam-column joints is investigated by analyzing *hybrid models* (H) and a *rigid model* (R) using incremental dynamic analysis (IDA) approach by Vamvatsikos and Cornell [34]. Incremental dynamic analysis approach (IDA) relates damage measures (inter-story drift ratios (θ_{max}), rotations etc.) with corresponding intensity measures such as 5% damped spectral acceleration at first-mode period (Sa (T_1, 5%)). In this approach, one or more unscaled ground motion records (accelerograms) are selected and multiplied by a scale factor S_a (T_1,

5%). Accelerograms are scaled so that S_a is increased by 0.1g and IDA curves are obtained by plotting (θ_{max}; $S_a(T_1, 5\%)$) pairs. In this study, incremental dynamic analyses (IDA) were performed by using Duzce (Turkey, 1999), Parkfield (USA, 1966) and Imperial Valley (USA, 1979) unscaled earthquake records shown in Figure 10 (PEER Strong Ground Motion Database, 2019) [35].

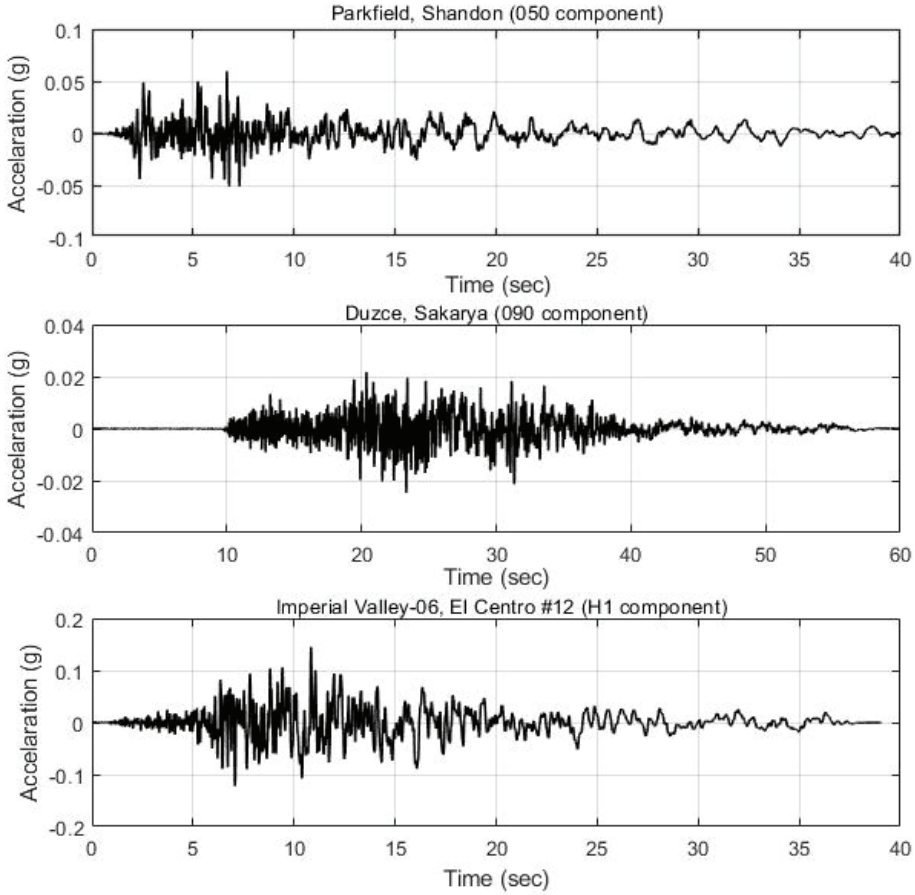

Figure 10 - Unscaled earthquake records for the incremental dynamic analyses [35]

Structural analysis models have similar longitudinal bar ratios and material strengths with S1 specimen and structural plan of the buildings as well as geometric details are shown in Figure 11. Calculated expected design loads based on tributary areas for a 4- story frame model is shown in Figure 12. Rayleigh damping corresponding to 5% critical damping in the first and second modes is applied. Floor masses are assigned to the intersections of joint nodes and truss model and equal dof is assigned to the nodes at each story level. Four-story hybrid (H4) and six-story hybrid (H6) models have 1.16 sec and 1.72 sec fundamental periods (T1), respectively.

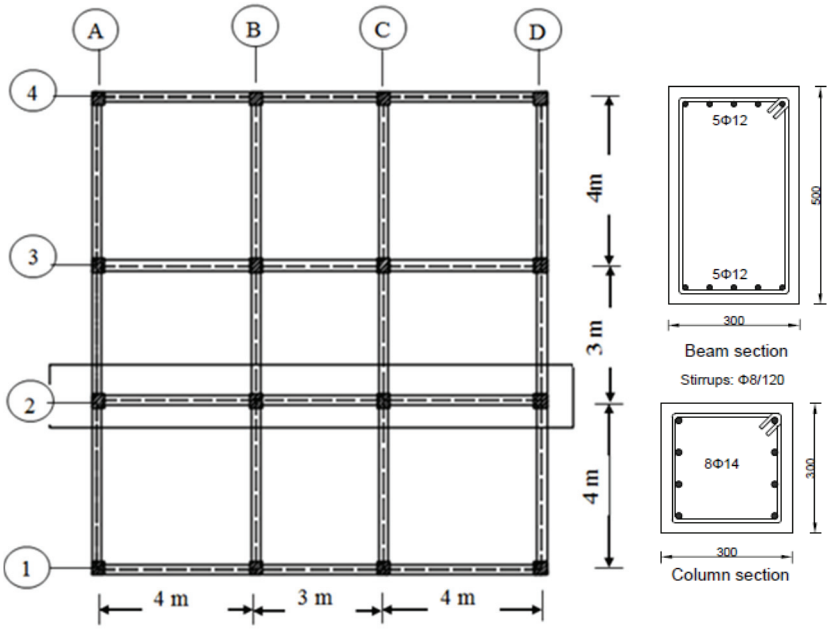

Figure 11 - Structural plan and column and beam reinforcing, and geometric details of RC building designed in 1970's

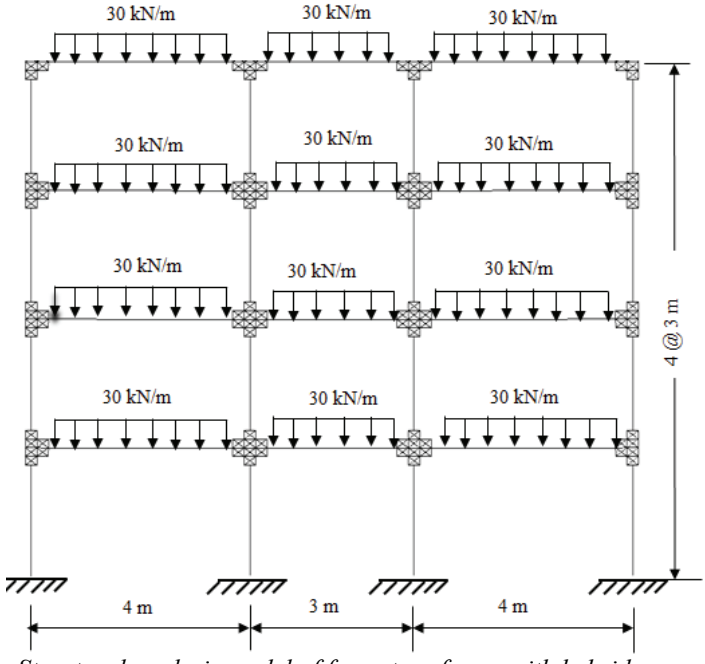

Figure 12 - Structural analysis model of four-story frame with hybrid connections (H4)

IDA curves are obtained with respect to the nonlinear dynamic analysis results. IDA procedure is repeated based on FEMA 350 (2000) [36] until the slope between consecutive points on IDA curve is less than 0.2 S_e, where S_e is the slope in elastic part. IDA curves in Figure 13 depict the relation between maximum inter-story drift ratios and spectral acceleration of the building for the amplitude scaled earthquake records. R4-P model with rigid joints reached a relatively lower drift ratio (2.5%) than H4-P model (4.2%) at same spectral acceleration (Sa (T_1) = 0.37 g). Figure 14 shows the roof displacement and corresponding base shear for structural models. Calculated maximum base shear for 4- and 6- story hybrid models are 106.5 kN and 86.1 kN, respectively. However, 4-story model with rigid joint assumption (R4-P) computed the maximum base shear as 198 kN which is approximately 2 times the base shear for hybrid models.

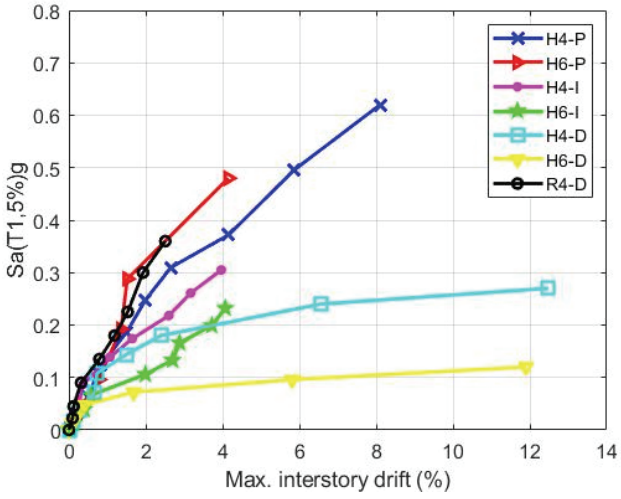

Figure 13 - IDA curves for 4- and 6 story structural models

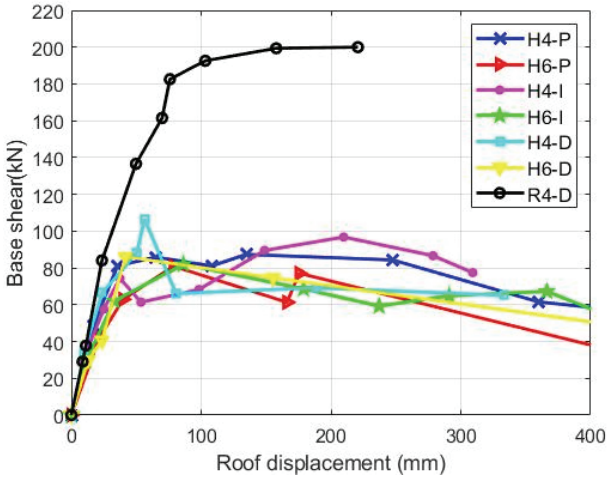

Figure 14 - Base shear- roof displacement relation for 4- and 6- story structural models

5. EVALUATION OF PERFORMANCE LIMITS

Performance-based seismic design approach provides numerical estimation of damage in structural elements subjected to earthquake loading. Acceptable damage limits are stipulated to be compatible with the anticipated performance levels for different intensity levels of earthquakes by codes. Performance levels for a structural element are defined as immediate occupancy (IO), life safety (LS) and collapse prevention (CP) for rotation-based defined in ASCE/SEI 41 (2006) [37] or strain-based limit states in Turkish Building Earthquake Code (TBEC-2018) [38].

The generic normalized force-deformation ratio relation and the performance limit states corresponding to certain deformations for a ductile structural element are shown in Figure 15 [37]. In this figure, line AB is the linear response up to effective yield point B while line BC represents the increase in strength due to strain hardening up to strength of the element C. Significant strength degradation is represented by line CD and residual strength at point E. The values in life safety (LS) performance level should be 0.75 times the deformation at point C which corresponds to collapse prevention (CP) performance level as given in [37].

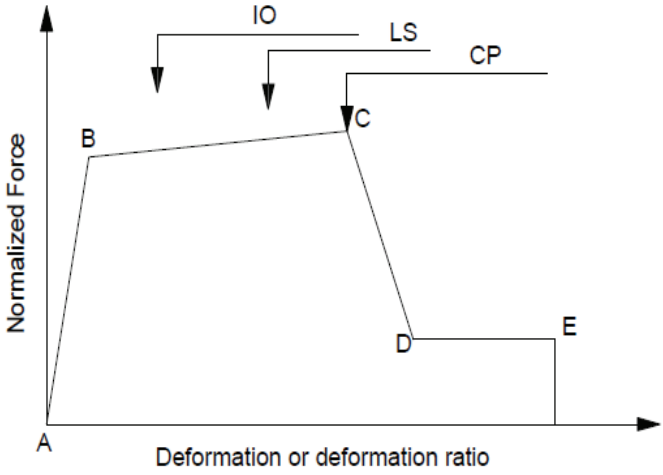

Figure 15 - Generalized component force-deformation relations [37]

Normalized moment- column rotation relationships of a ground story column for 4- and 6-story hybrid and rigid structural models are shown in Figure 16. Plastic chord rotations for performance levels of columns are summarized in Table 1. Besides, column performance limit states corresponding to axial load ratios for 4- and 6- story models are defined by Table 6.8 in ASCE/SEI 41 [36] and include only plastic rotations as shown in Table 1. Models with hybrid connections predicted lower plastic rotations for RC columns than ASCE/SEI 41 (2006) provisions for IO and CP performance levels. Model with rigid joints have 2.5 times higher plastic rotation values for RC columns compared to ASCE/SEI 41 (2006) limits. In hybrid models, based on the strength degradation of beam-column joints with diagonal

cracking, lateral loads of the structural system as well as column moment capacity are reduced.

Table 1 - Comparison of predicted RC column rotation-based limits for models and ASCE/SEI 41 [37] provisions

Model	*Plastic rotations (rad) (Models)*			*Plastic rotations (rad) (ASCE/SEI 41)*		
	IO	*LS*	*CP*	*IO*	*LS*	*CP*
H4-P	*0.003*	*0.010*	*0.017*	*0.004*	*0.0135*	*0.017*
H4-D	*0.003*	*0.009*	*0.015*	*0.004*	*0.0135*	*0.017*
R4-P	*0.008*	*0.033*	*0.048*	*0.004*	*0.0135*	*0.017*
H6-P	*0.003*	*0.008*	*0.013*	*0.003*	*0.012*	*0.015*
H6-D	*0.0025*	*0.006*	*0.010*	*0.003*	*0.012*	*0.015*

**IO: immediate occupancy; LS: life safety; CP: collapse prevention performance level*

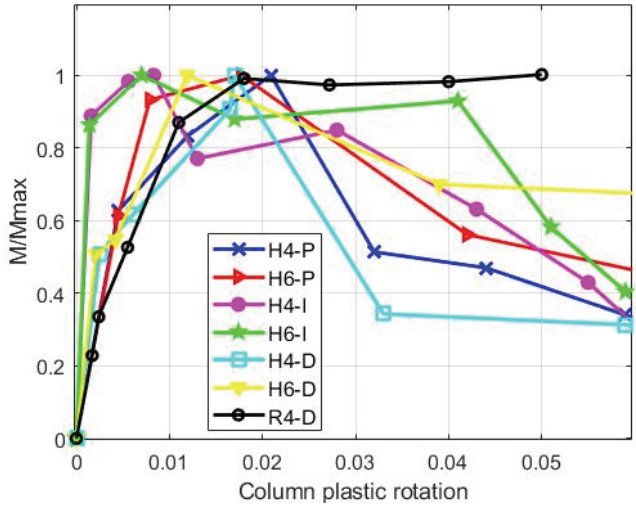

Figure 16 - Normalized moment-column chord rotations

Strain-based performance limits for seismic evaluation of reinforced concrete members are stipulated by Turkish Building Earthquake Code (TBEC-2018) [38]. Concrete and reinforcing bar strains for collapse prevention limit state are expressed by the equations below:

$$\varepsilon_c^{(CP)} = 0.0035 + 0.07\sqrt{\omega_{we}} \le 0.018 \tag{4}$$

$$\text{and } \omega_{we} = \alpha_{se}\,\rho_{sh,\min}\frac{f_{ywe}}{f_{ce}} \tag{5}$$

where α_{se} is the coefficient of effectiveness for transverse reinforcement, $\rho_{sh,\min}$ is the minimum volumetric ratio of transverse reinforcing bar, f_{ywe} and f_{ce} are the expected yield strength of the transverse reinforcement and concrete, respectively.

$$\alpha_{se} = \left(1 - \frac{\sum a_i^2}{6b_0h_0}\right)\left(1 - \frac{s}{2b_0}\right)\left(1 - \frac{s}{2h_0}\right) \tag{6}$$

$$\varepsilon_s^{(CP)} = 0.4\varepsilon_{su} \tag{7}$$

For life safety (LS) and immediate occupancy (IO) limit states concrete and reinforcing bar strains are defined as [38]:

$$\varepsilon_c^{(LS)} = 0.75\varepsilon_c^{(CP)} \text{ and } \varepsilon_s^{(LS)} = 0.75\varepsilon_s^{(CP)} \tag{8}$$

$$\varepsilon_c^{(IO)} = 0.0025 \text{ and } \varepsilon_s^{(IO)} = 0.0075 \tag{9}$$

Strain-based performance limits for column shear force ratios greater than 1.3 should be decreased by 50% of the strain limits defined in TBEC (2018) [38]. The tabulated maximum strains in Table 2 for hybrid and rigid models are computed using the strain-column chord rotation plots shown in Figure 17 and were compared with the strain limits with the decreased limits in TBEC (2018) for columns at the ground story. Computed strains for models with rigid beam-column joint assumption (R4-P) have higher values than hybrid models.

Table 2 - Computed maximum strains in hybrid and rigid joint models for corresponding performance levels

Performance levels	*Cover concrete*		*Core concrete*		*TBEC (2018)*	*Reinforcing bar*		*TBEC (2018)*
	Hybrid	*Rigid*	*Hybrid*	*Rigid*	*Concrete*	*Hybrid*	*Rigid*	*Reinforcing bar*
IO	*0.0013*	*0.002*	*0.0011*	*0.0016*	*0.00125*	*0.0012*	*0.0022*	*0.0037*
LS	*0.0018*	*0.0049*	*0.0014*	*0.0048*	*0.00675*	*0.0015*	*0.0079*	*0.018*
CP	*0.0023*	*0.005*	*0.0019*	*0.007*	*0.009*	*0.0019*	*0.011*	*0.024*

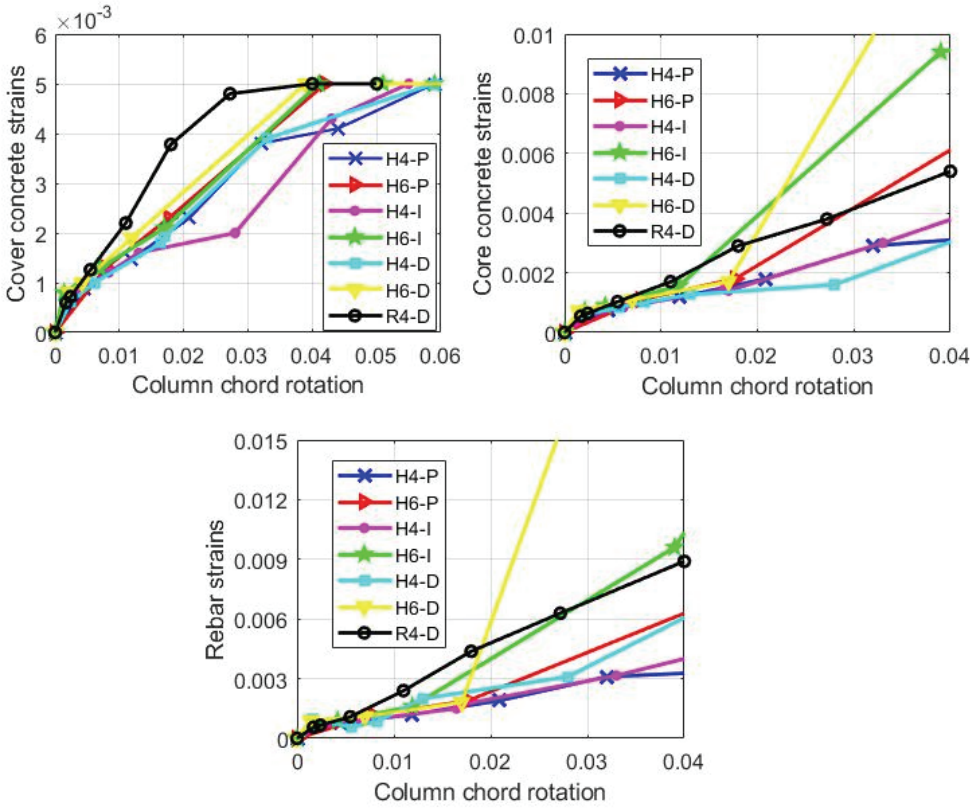

Figure 17 - Predicted column chord rotations and corresponding strains for (a) cover concrete, (b) core concrete and (c) reinforcing bars

6. CONCLUSIONS

This paper has presented a hybrid numerical model for performance-based seismic evaluation of columns of existing reinforced concrete buildings with non-seismically detailed beam-column joints. Hybrid numerical model including truss and fiber-based models has been validated with two exterior beam-column joint tests subjected to cyclic loading. Numerical model has simulated the observed joint behavior with crushing of diagonal elements at the joints. Developed four and six story frame models have been analyzed by performing nonlinear incremental dynamic analyses. Rotation-based performance limit states for RC columns of non-ductile frames have been investigated and compared with ASCE/SEI 41 (2006) provisions. Besides, strain-based limits have been obtained for cover concrete, core concrete and reinforcing bar strains of reinforced concrete columns at the ground story and compared with TBEC (2018) provisions. The results showed that plastic rotations and corresponding concrete and reinforcing bar strains of columns have relatively lower values than the code provisions for life safety (LS) and collapse prevention (CP) performance limits. Modeling non-ductile RC frames with rigid joint assumption has led to an underestimation

in damage levels of members. Further numerical studies should be performed considering bond slip of beam reinforcing bars in interior joints and reinforcing material models accounting for buckling and rupture. Also, performance limit states for beams and joints should be performed by increasing the number of ground motion records in the scope of future studies.

Symbols

a_i = distance between axes of longitudinal bars which are supported with a tie leg [mm]

b_0 = cross-section dimension between axes of ties confining the core area [mm]

B_s = post-yield hardening ratio

d_b = longitudinal bar diameter [mm]

E_s = Young Modulus of reinforcing steel material [MPa]

f_c' = Compressive strength of unconfined concrete [MPa]

f_{ce} = Average (expected) compressive strength of concrete [MPa]

f_{ck} = Characteristic compressive strength of unconfined concrete [MPa]

f_t = Tensile strength of concrete [MPa]

f_y = Yield strength of longitudinal bar [MPa]

f_{ywe} = Average (expected) yield strength of transverse bar [MPa]

h_0 = cross-section dimension between axes of ties confining the core area [mm]

M = tension stiffening parameter

s = tie spacing [mm]

$S_a(T_1)$ = spectral acceleration at first-mode period [m/sn^2]

T_1 = period corresponding the fundamental mode (sn)

α_{se} = coefficient of effectiveness for transverse reinforcement

β = reduction coefficient

ε_0 = Compressive strain of unconfined concrete at maximum strength

$\varepsilon_c^{(CP)}$ = Compressive strain limit of concrete at collapse prevention limit state

$\varepsilon_s^{(CP)}$ = Strain limit of reinforcing bar at collapse prevention limit state

ε_n = normal strains in concrete

ε_u = Ultimate compressive strain of unconfined concrete at maximum strength

ε_y = Yield strain of longitudinal bar

θ_{max} = maximum inter-story drift ratios

$\rho_{sh,min}$ = minimum volumetric ratio of transverse reinforcing bar

ρ_l = longitudinal reinforcing bar ratio

ω_{ce} = mechanical reinforcing bar ratio of effective confinement

Acknowledgement

The author would like to thank Prof. Dr. Serap Kahraman and Assoc. Prof. Dr. Ibrahim Serkan Misir for sharing the beam-column test data and providing their valuable opinions during preparation of the study.

References

[1] Hanson, N. W., & Conner, H. W. 1967, Seismic resistance of reinforced concrete beam-column joints, J. of Str. Div., 93(5), 533-560, 1967.

[2] Park, R., and Paulay, T., Behaviour of reinforced concrete external beam-column joints under cyclic loading, Proceedings of the 5th World Conference on Earthquake Engineering, Rome, 1973.

[3] Kunnath, S. K., Hoffmann, G., Reinhorn, A. M., Mander, J. B., Gravity-load-designed reinforced concrete buildings — Part I: Seismic evaluation of existing construction, ACI Structural Journal, 92(3), 343–354, 1995.

[4] Hakuto, S., Park, R., Tanaka, H., Seismic load tests on interior and exterior beam column joints with substandard reinforcing details, ACI Structural Journal, 97(1), 11-25, 2000.

[5] Park, R., A summary of results of simulated seismic load tests on reinforced concrete beam-column joints, beams and columns with substandard reinforcing details, J. of Earth. Eng., 6(2), 147-174, 2002.

[6] Bedirhanoglu, I., Ilki, A., Pujol, S. and Kumbasar, N., Behavior of deficient joints with plain bars and low-strength concrete, ACI Structural Journal, 107(3), 300-310, 2010.

[7] Gökdemir, H. and Tankut, T., Kiriş-kolon birleşim bölgesinin depreme karşı çelik donatılarla güçlendirilmesi, İMO Teknik Dergi, 7977-7992, 2017.

[8] Moehle, Jack P. Seismic design of reinforced concrete buildings. New York: McGraw-Hill Education, 2015.

[9] Alire, D., Seismic evaluation of existing unconfined reinforced concrete beam-column joints, M.S. Thesis, University of Washington, Seattle, WA, 306pp, 2002.

[10] Lima C., Martinelli, E., Macorini, L. and Izzuddin, B. A., Modelling beam-to-column joints in seismic analysis of RC frames, Earthquakes and Structures, 12(1), 119-133, 2017.

[11] Bayhan, B., Özdemir, G., and Gülkan, P., Impact of joint modeling approach on performance estimates of older-type RC buildings, Earthquake Spectra, 33(3), 1101-1123, 2017.

[12] Calvi, G. M., Magenes, G., and Pampanin, S., Relevance of beam-column joint damage and collapse in RC frame assessment, J. of Earth. Eng., 6(1), 75-100, 2002.

[13] Favvata, M. J., Izzuddin, B. A., and Karayannis, C. G., Modelling exterior beam–column joints for seismic analysis of RC frame structures, Earth. Eng. and Str. Dyn. 37(13), 1527-1548, 2008.

[14] Sharma, A., Eligehausen, R., and Reddy, G. R., Pivot hysteresis model parameters for reinforced concrete columns, joints, and structures, ACI Structural Journal, 110(2), 217-227, 2013.

[15] Bedirhanoğlu, I, Düşük dayanımlı betona sahip betonarme kolon ve birleşimlerin deprem yükleri altında davranışlarının incelenmesi ve iyileştirilmesi, Doktora tezi, İstanbul Teknik Üniversitesi Fen Bilimleri Enstitüsü, 2009.

[16] Youssef, M., and Ghobarah, A., Modelling of RC beam-column joints and structural walls, Jour. of Earth. Eng., 5(1), 93-111, 2001.

[17] Lowes, L. N., Mitra, N., and Altoontash, A., A beam-column joint model for simulating the earthquake response of reinforced concrete frames, Report No. PEER 2003/10; Pacific Earthquake Engineering Research Center, College of Engineering, University of California, Berkeley, 2003.

[18] Park, S. and Mosalam, K.M., Simulation of reinforced concrete frames with nonductile beam-column joints. Earthquake Spectra, 29(1), 233-257, 2013.

[19] Kostic, S., and Filippou, F., Section discretization of fiber beam-column elements for cyclic inelastic response. Jour. of Str. Eng., 138, 592-601, 2012.

[20] Kim, J. H., and Mander, J. B. Truss modeling of reinforced concrete shear – flexure behaviour, MCEER Report 99-0005, University at Buffalo, State University of New York, 1999.

[21] Miki, T., and Niwa, J., Nonlinear analysis of RC structural members using 3D lattice model, J. of Adv. Con. Tech., 2(3), 343-358, 2004.

[22] Park, H., and Eom, T., Truss model for nonlinear analysis of RC members subject to cyclic loading, J. of Str. Eng., 133(10), 1351-1363, 2007.

[23] To, N., Sritharan, S., and Ingham, J., Strut-and-tie nonlinear cyclic analysis of concrete frames", J. of Str. Eng., 135(10), 1259-1268, 2009.

[24] Panagiotou, M., Restrepo, J. I., Schoettler, M., and Kim, G., Nonlinear cyclic truss model for reinforced concrete walls, ACI Structural Journal, 109(2), 205-214, 2012.

[25] Moharrami M., Koutromanos I., Panagiotou M., Girgin S.C., Analysis of shear-dominated RC columns using the nonlinear truss analogy, Earth. Eng. and Str. Dyn., 44(5), 677-694.

[26] Bowers, J.T., Nonlinear cyclic truss model for beam-column joints of non-ductile RC frames. M.Sc. thesis, Virginia Polytechnic and State University, 2014.

[27] Xing C., Koutromanos I., Leon R., and Moharrami M., Computational simulation of RC Beam-to-Column Connections Under Earthquake Loading, Eleventh US National Conference on Earthquake Engineering, Loa Angeles, CA, USA, 2018.

[28] McKenna, F., Fenves, G. L., Scott, M. H., and Jeremic, B. Open system for earthquake engineering simulation. http://opensees.berkeley.edu, 2015.

[29] Lu, Y. and Panagiotou, M., Three-dimensional cyclic beam-truss model for non-planar reinforced concrete walls, J. of Str. Eng., 140(3), 2014.

[30] Stevens, N. J., Uzumeri, S. M., Collins, M. P., and Will, T. G., Constitutive model for reinforced concrete finite element analysis, ACI Structural Journal, 99(10), 2109-2122, 1991.

[31] Vecchio, F. G. & Collins, M.P., The modified compression field theory for reinforced concrete elements subjected to shear, J. of the American Con. Inst., 83(2), 219-231, 1986.

[32] Misir, I. S., & Kahraman, S., Strengthening of non-seismically detailed reinforced concrete beam–column joints using SIFCON blocks, Sadhana, 38(1), 69-88, 2013.

[33] Pantelides, C.P., Hansen, J., Nadauld, J. and Reaveley, L.D., Assessment of reinforced concrete building exterior joints with substandard details. PEER report, 2002.

[34] Vamvatsikos, Dimitrios, & Cornell, C.A., Incremental dynamic analysis. Earth. Eng. & Str. Dyn. 31.3:491-514, 2002.

[35] Pacific Earthquake Engineering Research (PEER) Center, PEER Strong MotionDatabase, https://peer.berkeley.edu/peer-strong-ground-motion-databases/, 2019.

[36] FEMA 350 (2000). Recommended seismic design criteria for new steel moment-frame buildings. Federal Emergency Management Agency, 2000.

[37] ASCE/SEI 41, Seismic rehabilitation of existing buildings, Reston, VA, U.S.A 2006.

[38] Turkish Building Earthquake Code (TBEC), Principles for the design of buildings under earthquake, Ankara, Turkey, 2018.

Teknik Dergi, 2020 10359-10378, Paper 594

Corrosion Behavior of Rebars Embedded in Alkali-Activated and Conventional Reactive Powder Concretes

Hüseyin YİĞİTER[1]
Ahsanollah BEGLARIGALE[2]
Serdar AYDIN[3]
Bülent BARADAN[4]

ABSTRACT

The present study investigated the corrosion behavior of reinforcement bars embedded in alkali-activated (ARPC) and conventional (CRPC) reactive powder concretes. Corrosion progress in 3.5% NaCl solution, water and air environments were monitored up to 365 days. The physical and mechanical characteristics, such as water absorption, rapid chloride ion permeability, compressive and flexural strength, and corrosion characteristics, such as half cell potential and corrosion current intensity results were compared for ARPC and CRPC matrices. Even for the same mechanical performance, alkali-activated mortars were found to have a high permeable structure and an early depassivation of the rebars occurred. In the propagation stage of chloride induced corrosion, almost 13 times higher corrosion current intensity values were measured as well as earlier deterioration and cracking was observed for ARPC compared to CRPC.

Keywords: Reactive powder concrete, alkali-activated slag, steel rebar, chloride-induced corrosion.

1. INTRODUCTION

Reactive powder concrete (RPC) shows great potential for use in special applications such as nuclear structures, impact-resistant structures, skyscrapers, corrosion-resistant structures

Note:
- This paper has been received on November 2, 2018 and accepted for publication by the Editorial Board on July 17, 2019.
- Discussions on this paper will be accepted by January 31, 2021.
- https://dx.doi.org/10.18400/tekderg.478154

1 Dokuz Eylül University, Department of Civil Engineering, Izmir, Turkey - huseyin.yigiter@deu.edu.tr - https://orcid.org/0000-0001-7414-8620

2 Istanbul Okan University Department of Civil Engineering, İstanbul, Turkey - ahsan.beglari@okan.edu.tr ahsan.beglari@gmail.com - https://orcid.org/0000-0002-4842-4289

3 Dokuz Eylül University, Department of Civil Engineering, Izmir, Turkey - serdar.aydin@deu.edu.tr - https://orcid.org/0000-0002-0830-5357

4 Dokuz Eylül University, Department of Civil Engineering, Izmir, Turkey - bulent.baradan@deu.edu.tr - https://orcid.org/0000-0001-5271-1224

and pre-fabricated structural elements such as bridge bearings, security vaults, waste/transportation vessels etc. RPC has very high high compressive strength (200 - 800 MPa [1]), fracture energy and tensile strain capacity. The basic principles for developing RPC are; enhancement of homogeneity by elimination of coarse aggregate, microstructure enhancement by heat curing, steel fiber incorporation for ductility, and densification of cementitious matrix through optimization of granular mixture, and application of pressure during setting [1-4].

The deficiency of RPC is its high heat of hydration, high drying shrinkage and high price as a result of its very high Portland cement content. Recent intensive studies performed by Aydın and Baradan [2, 5-9], showed that RPC can be produced by using alkali-activated slag without any Portland cement. These studies showed that activator solution with 4% Na_2O content and M_s=1.2 (solution modulus, Ms = mass ratio SiO_2/Na_2O) provides optimum properties in terms of compressive strength, setting times and drying shrinkage [5, 6], steam curing at 100 °C present better mechanical performance compared to autoclaving [6], silica fume act as a water reducer and shrinkage reducer in alkali activated systems in contrast to Portland cement based systems [2]. For instance, at 20% of GGBFS replacement with SF, the water/binder ratio decreased from 0.44 to 0.20 [2]. By this way and with incorporation of 1.5% steel fiber with 13 mm length, alkali-activated slag based reactive powder concrete (ARPC) that has compressive strength values over 200 MPa has been produced [8]. The mechanical properties of ARPC and conventional Portland cement based reactive powder concrete (CRPC) were given in Table 1. It should be noted that both RPC mixtures have 1.5% steel-fiber by volume. As shown in Table 1, the flexural performance and fracture energy of steam cured ARPC were better than CRPC in the same compressive strength class. Aydın and Baradan also showed [9] that the ARPC had a better high temperature resistance as well as better adherence ability to steel when compared to CRPC. ARPC did not show explosive spalling up to 800 °C while CRPC samples suffered from explosive spalling beyond 300 °C [9]. Because of its technical advantages (lower heat of hydration, higher strength, better durability etc.) and environmental benefits (lower CO_2 emission, lower energy demand, and conservation of natural resources), ARPC is a very good alternative to CRPC.

Table 1 - Properties of steam cured ARPC and CRPC [8]

Mechanical Properties	**ARPC**	**CRPC**
Compressive strength, MPa	215.9	214.6
Splitting tensile strength, MPa	19.5	19.2
Modulus of elasticity, GPa	84.1	114.0
Poisson ratio	0.22	0.21
Fracture energy, N/m	16016	14200
Flexural strength, MPa	41.5	34.7

On the other hand, a necessity on investigating the steel corrosion behavior embedded in alkali activated composites still exists. While some researchers concluded that alkali-activated composites had better performance, some researchers contradict this mechanism.

Wang, et al. [10] have stated that aluminate in the pore solution of alkali activated slag (AAS) mortar had an inhibition effect on the corrosion of steel bars after the addition of NaCl. Silicate, another major ion in the AAS pore solution, provided a good protective effect on the steel bars in both passivation and chloride attack stages. Simulated pore solutions of AAS mortar had a greater capacity to passivate steel bars than the simulated pore solutions of Portland cement (PC) mortar and had better protective effect on steel bars from chloride ingress, especially under higher chloride concentration. Ma et al. [11] have concluded that AAS concretes had higher total chloride content at the surface than that of PC concrete. Greater ionic exchange between chloride and the hydroxyl ions and the possibly enhanced chloride binding at the surface of the AAS concretes have been identified as the possible reasons. AAS concretes were found to have lower chloride diffusivity, better pore structure, stronger interaction between hydration products and accompanying sodium, improved chloride binding. Non-steady state diffusion coefficient (D_{nssd}) of AAS concretes was found to be influenced by both Na_2O and M_s. 6% Na_2O and 1.5 M_s seems optimum for reducing the rate of corrosion. Holloway and Sykes [12] have investigated the corrosion behavior of steel in alkali activated slag cement containing NaCl admixtures. Even the very high level of chloride admixture in alkali activated slag cement mortar, the corrosion rates of these mortars were found low. Babaee and Castel [13] showed that the low-calcium fly ash based geopolymer concrete exhibit a comparable electrochemical performance to a similar strength PC concrete during propagation phase of corrosion. Additionally, recalibration need on the some of the measurements and classification techniques for corrosion assessment, especially for the Tafel slopes, have been noted. Chaparro et al. [14] have concluded that AAS concrete presented passive corrosion behavior in the first 3 months, after which it presented decreased corrosion resistance lower than that of ordinary portland cement (OPC) concrete. Aperador et al. [15] have investigated the corrosion of steel rebars embedded in carbonated and uncarbonated alkali-activated slag and Portland cement concretes. The steel corrosion rates of AAS concretes were found to be higher than PC concretes. The highest corrosion rate was obtained with carbonated AAS concrete. Aperador et al. [15] also stated that carbonation rate was higher in AAS concrete than in the respective OPC concrete under both accelerated and laboratory environment. The high carbonation rate of AAS might be attributed to the low calcium content that leads to a low capacity to buffer the pH of the pore solution in AAS and also leads to rate deposits of $CaCO_3$. Monticelli et al. [16] have characterized the corrosion behavior of reinforcing bars in alkali-activated fly ash (AAFA) mortars by corrosion potential, polarization resistance and electrochemical impedance spectroscopy measurements. AAFA mortars afforded a lower corrosion protection to the rebars and the FA mortars were found to undergo a fast carbonation so that depassivation of the rebars occurred concurrently in spite of a limited total chloride content. Higher scale porosity was found in geopolymers. After 95 days, active corrosion was started in 50% of rebars embedded in reference mortar. On the other hand rebars in geopolymers started active corrosion after 20 days.

It seems that ARPC is a very good alternative to CRPC with its technical advantages such as mechanical strength and environmental benefits. On the other hand, the use of a newly developed material in application is significantly dependent on its durability properties, such as corrosion behavior of steel bars embedded in this mixture. Within the scope of this study, corrosion behavior of steel reinforcing bars embedded in the ARPC and CRPC matrices were investigated as well as the physical and mechanical characteristics of matrices.

2. EXPERIMENTAL

2.1. Materials

Ground granulated blast furnace slag (GGBFS) and silica fume (SF) for ARPC, and ordinary Portland cement and SF for CRPC were used as cementitious materials. GGBFS was procured from Ereğli steel plant with the chemical composition presented in Table 2. Blaine specific surface area value of GGBFS was 410 m^2/kg, and 90% of particles were smaller than 45 µm. CEM I 42.5 type OPC with 369 m^2/kg Blaine fineness, and a commercial SF with BET fineness of 23360 m^2/kg have been used. The chemical compositions of PC and SF were also presented in Table 2. A commercial quartz sand with a maximum size of 3 mm was used as aggregate. The particle size distribution curves of SF/GGBFS and quartz aggregate were shown in Figs. 1 and 2, respectively.

Table 2 - Chemical composition of cementitious materials

	SiO_2	Fe_2O_3	Al_2O_3	CaO	MgO	Na_2O	K_2O	SO_3	Loss on ignition
GGBFS	40.20	1.68	11.66	35.90	5.88	0.30	1.47	0.90	0.88
PC	19.10	3.96	4.40	61.85	2.05	0.27	0.70	3.72	1.82
SF	96.10	—	—	—	—	—	—	—	1.81

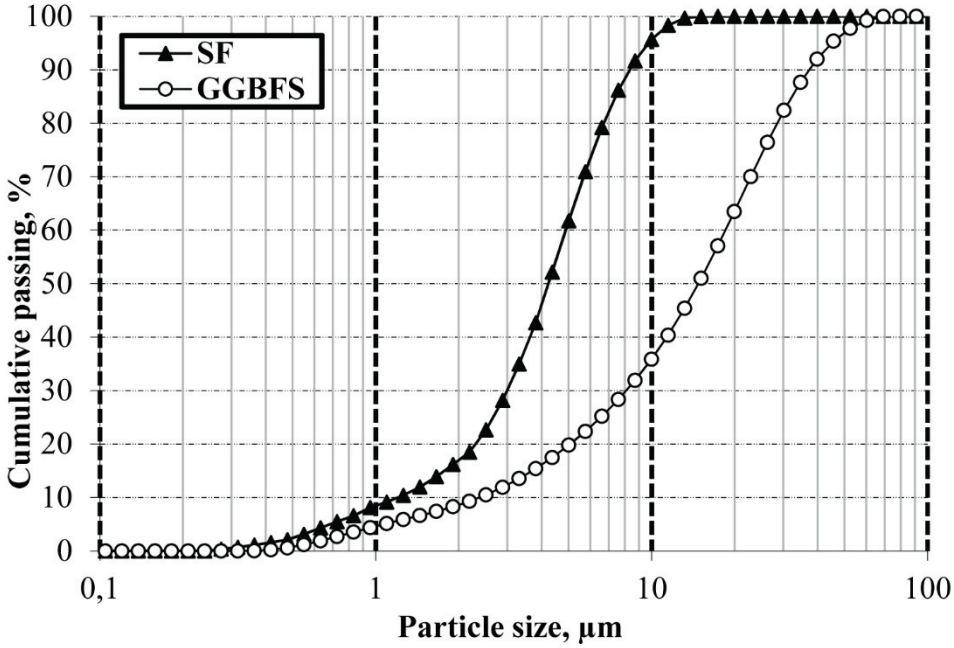

Figure 1 - Particle size distribution of SF and GGBFS

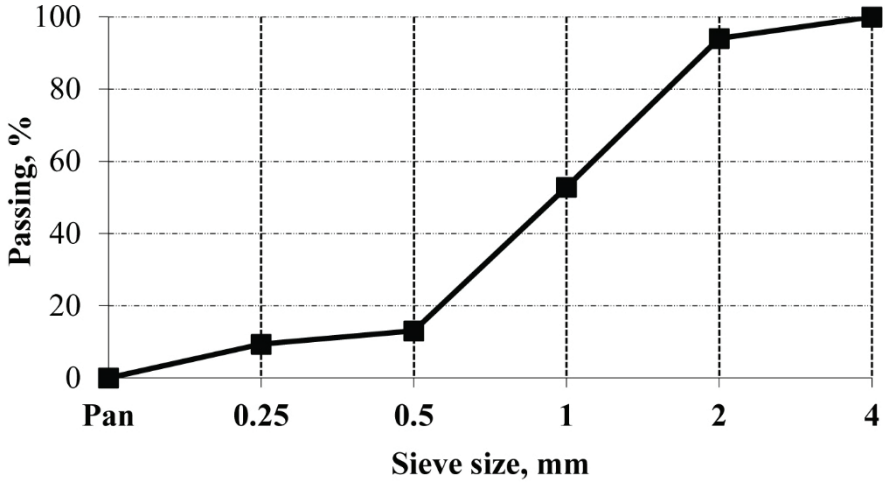

Figure 2 - Particle size distribution of quartz aggregate

ARPC has been produced by the activation of GGBFS and SF with the mixture of technical grade sodium hydroxide and sodium silicate providing silicate modulus (M_s=SiO_2/Na_2O) in the solution 1.2 and Na_2O was 4% by binder weight. A polycarboxylate-based superplasticizer with a 40% solid content has been used in CRPC production.

The compositions of ARPC and CRPC based on previous studies [8, 9] were given in Table 3. In order to produce an ARPC with compressive strength of RPC class, the water/binder ratio of the concrete must be at about 0.20. In conventional RPC, the water/binder ratio can be reduced to 0.20 by using high range water reducer (superplasticizers). However, in the alkali-activated binders, the superplasticizers do not show any water-reducing effect. This effect can only be achieved by silica fume replacement with slag. For conventional RPC class concrete with Portland cement binder, the high compressive strength values can be obtained thanks to silica fume's filler effect and strong pozzolanic properties. It should be noted that the previous study [7] showed that the optimum SF replacement percentage for ARPC was 20% by weight of total binder (GGBFS+SF). The lower dosages caused to inadequate setting time and workability while the higher dosages resulted in very high viscosity. Thus, silica fume contents of both RPC mixtures were selected as 20%. In the preparation of ARPC, the powders were dry-mixed at low speed (99 rev/min) in a pan type special designed mixer for about 1 minute. After the introduction of activator solution, materials were mixed at a low speed (99 rev/min) for a minute then at a high speed (440 rev/min) for about 2 minutes. Aggregates were added to pre-mixed composition and mixed at the same high speed for about 2 minutes. A similar procedure was applied for the production of CRPC samples. The mixtures were cast into molds, and compacted by hand operations and vibration. Pressure was not applied to the fresh samples. The specimens were kept in the molds for 5 h at room temperature of ~ 20 °C. Then, the specimens were subjected to steam curing at 100 °C for 12 h at a heating rate of 22 °C/h.

Table 3 - Mixture proportions for ARPC and CRPC

Components	ARPC	CRPC
GGBFS, kg/m^3	720.0	--
PC, kg/m^3	--	720.0
SF, kg/m^3	180.0	180.0
Quartz (1-3 mm), kg/m^3	543.2	575.3
Quartz (0.6-1.2 mm), kg/m^3	422.5	447.5
Quartz (0-400 μm), kg/m^3	144.9	153.4
Quartz (0-75 μm), kg/m^3	96.6	102.3
Waterglass, kg/m^3	160.0	--
NaOH, kg/m^3	30.9	--
Water, kg/m^3	49.0	123.0
Superplasticizer, kg/m^3	--	50.0
Water/binder ratio	0.17	0.17
Aggregated/binder ratio	1.34	1.42

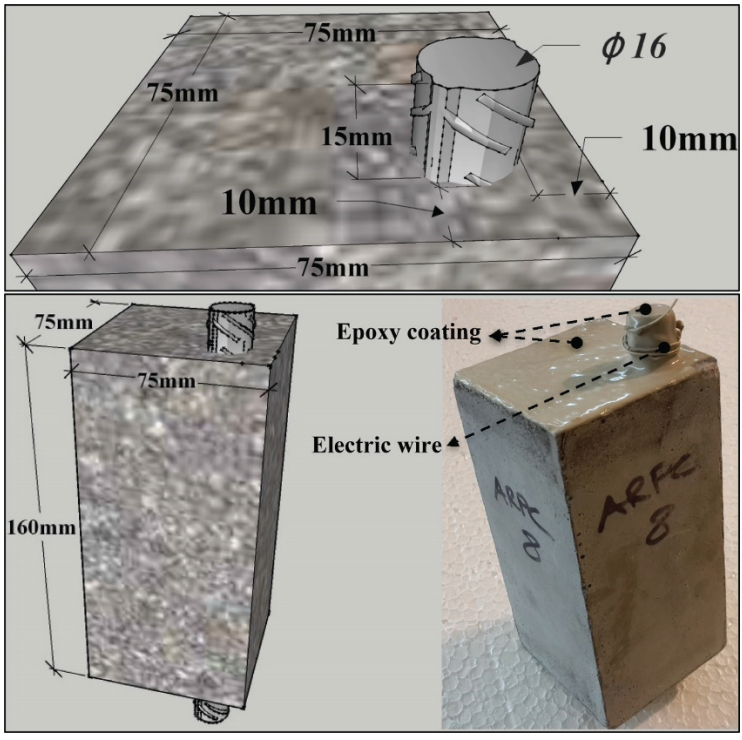

Figure 3 - Details of corrosion test specimens

The schematic figure of corrosion test specimen and its details are presented in Fig. 3. S420 grade deformed steel rebar (yield strength of 511 MPa, tensile strength 605 MPa, strain capacity at failure 21%) with a diameter of 16 mm was used. For corrosion tests, an electric wire was mounted on one of the free ends of the rebar. The upper and lower surface of the specimens and also free ends of the rebar were carefully sealed by epoxy coating. The first group of specimens was subjected to wetting-drying cycles in 3.5% NaCl solution. The corrosion process of specimens was monitored after 200, 400, 1400 wetting-drying cycles. It must be mentioned that the 1400 wetting-drying cycles lasted in 360 days. The second and third groups of specimens were kept in water and in air at laboratory conditions, respectively, for 360 days.

2.2. Measurements

Flexural strength of the mixtures was determined on three prismatic specimens (40 x 40 x 160 mm). Compressive strength values were determined on broken specimen pieces (40 x 40 mm) left from flexural test.

The sorptivity values of RPC matrices were determined on three prismatic specimens (40 x 40 x 160 mm) by the measurement of water absorption by capillary rise. The specimens were dried at 105 ± 5 °C to achieve constant weight. Side surfaces of the samples were coated to prevent absorption through side surfaces. Then the specimens were kept in a water tray with small supports and the water level was maintained in such a way that only 3 mm of the specimens were submerged in water. The weight measurements were recorded for 48 h.

The volume of permeable voids and total water absorption capacity of mortar specimens were determined on the three disk specimens with a radius of 100 mm and 50 mm height according to ASTM C642 [17]. The specimens were dried at 105±5 °C to constant weight. After cooling the specimens were weighted (A). The specimens were immersed in water for 72 h and weighed (B). Then the specimens were boiled in water for 5 h, then surface moisture was removed and the saturated surface dry weight was measured (C). Finally, apparent volume of samples boiled in water was determined using Archimedes' scales (D). Total water absorption and volume of permeable voids, V_{pv} determined by using Eq. 1 and 2, respectively.

$$\text{Water absorption (\%)} = [(B-A)/A]\times 100 \quad (1)$$

$$\text{Volume of permeable voids (\%)} = [(C-A)/(C-D)]\times 100 \quad (2)$$

The rapid chloride permeability (RCPT) tests were performed on cylindrical specimens with 100 mm diameter and 50 mm thickness according to the ASTM C 1202 standard [18].

The open-circuit potential (E_{OCP}) and corrosion current density (i_{corr}) values of the specimens were obtained using a computer-controlled potentiostat, Gamry Interface1000, through a three-electrode system (Fig. 4). The working electrode was the rebar embedded in the concrete matrices. Saturated calomel electrode (SCE) and graphite were used as the reference electrode and counter electrode, respectively. The E_{OCP} measurements were carried out for at least 60 min to obtain a steady state condition. Immediately after E_{OCP} measurement the potentiodynamic polarization curves were obtained in the ±150 mV range of E_{OCP} with scan

rate of 0.2 mV/s. The corrosion current density has been analyzed through the Tafel analysis. It must be noted that the electrolytic environment of three-electrode system was the 3.5% NaCl solution.

Pore-size distributions of the samples were determined by the Mercury Intrusion Porosimetry (MIP) method.

Figure 4 - Corrosion test setup.

3. RESULTS AND DISCUSSION

3.1. Workability and Mechanical Properties

Fresh state flow diameter, compressive strength and flexural strength values of ARPC and CRPC matrices without steel fiber were given in Table 4. As shown in Table 4, both RPC matrices have a quite high workability. The compressive strength values of ARPC and CRPC matrices were about 134 MPa while the flexural strength of ARPC was about 22% higher than CRPC.

Table 4 - Workability and mechanical properties of ARPC and CRPC matrices.

	ARPC matrix	CRPC matrix
Flow diameter, mm	167	186
Compressive strength, MPa	133.3	135.1
Flexural strength, MPa	12.4	10.2

3.2. Physical properties

Fig. 5 shows the capillary water absorption of RPC matrices. As shown in Fig. 5 the capillary water absorption of ARPC matrix was significantly higher than CRPC. As expected, the slope of capillary water absorption curves for both RPC matrices reduced with elapsed time. For CRPC matrix, the capillary water absorption ceased beyond 24 hours. However, matrix phase of ARPC continued to capillary water movement up to 48 hours. Capillary water suction value of CRPC matrix at 48 hours was about one-third of the ARPC's value. The volume of permeable voids and total water absorption by weight of ARPC and CRPC matrices are presented in Fig. 6. Parallel to capillary water absorption test results, the amount of permeable voids and total water absorption of ARPC matrix were about four times higher than CRPC.

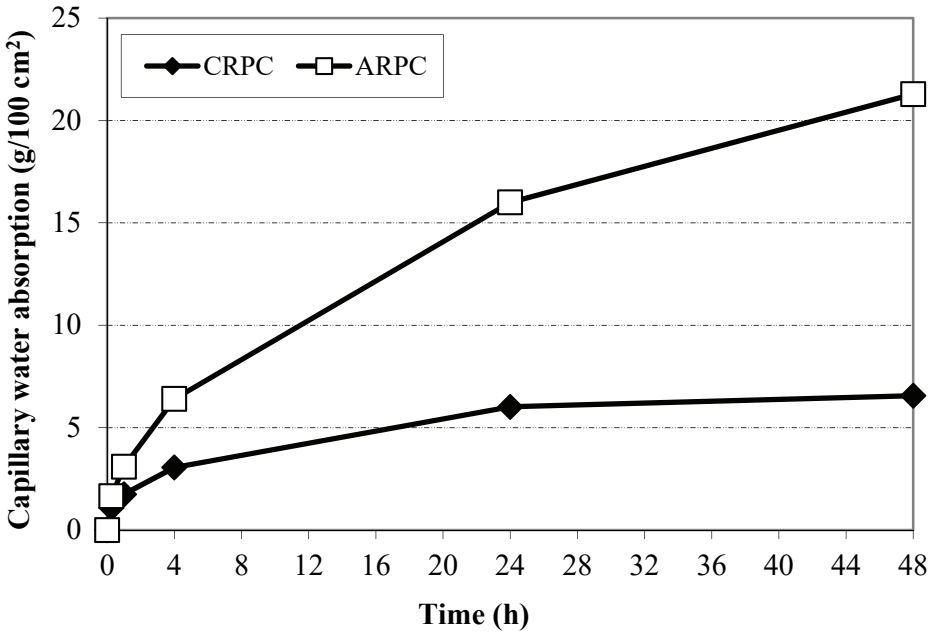

Figure 5 - Capillary water absorption of ARPC and CRPC

Pore size distribution of ARPC and CRPC matrices were presented in Fig. 7. As shown in Fig. 7, pores in cement-based materials can be categorized as gel pores, capillary pores and

macro pores. Macro pores mainly influence the mechanical properties while the capillary pores affect the permeability and mechanical properties [19]. As shown in Fig. 7, ARPC have a coarser pore size distribution compared to CRPC. The pores in CRPC were generally lower than 0.008 μm and can be classified as gel pores. The amount of gel, capillary and macro pores in ARPC was significantly higher than those of CRPC. The high amount of capillary pores in ARPC explains its higher permeability compared to CRPC.

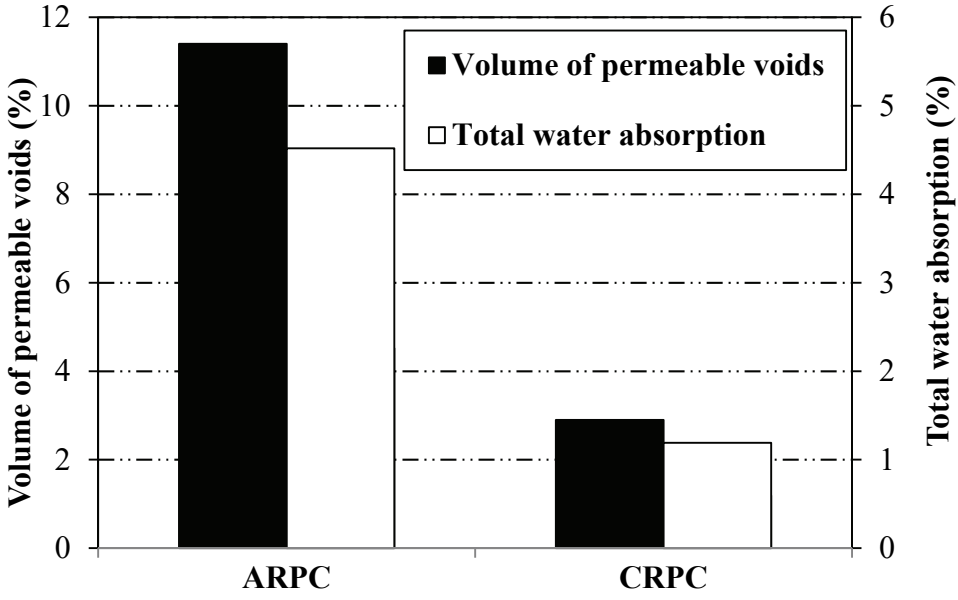

Figure 6 - Volume of permeable voids and total water absorption of mixtures.

From the stand point of electrical indication of concrete's ability to resist chloride ion penetration, there was no any charge passing in the CRPC mixture, whereas in the ARPC mixture there was 700 coulombs after 6 hours. Concretes are divided into five permeability classes according to the ASTM C1202 standard classification. According to this classification, the chloride permeability for CRPC was "negligible", while the ARPC mixture was "very low". RCPT is a measurement based on the electrical conductivity of concrete and depends on the pore structure of the concrete and also the chemistry of the pore solution. The higher amount of charge passing through the ARPC mixture as compared to the CRPC mixture can be attributed to the more porous structure of ARPC, but mainly to the change in the chemical composition of the pore solution of these concretes. Najimi and Ghafoori [20] have reported that the RCPT can give pessimist results in the case of alkali activated cement. They have stated that the high alkali ion concentrations in the pore solution of these materials increase the electrical conductivity remarkably. From the obtained data, it can be said that the electrical resistance of the ARPC mixture was lower than the CRPC mixture. However, it is thought that the experimental results do not give a good information about the chloride ion permeability for the reasons mentioned above.

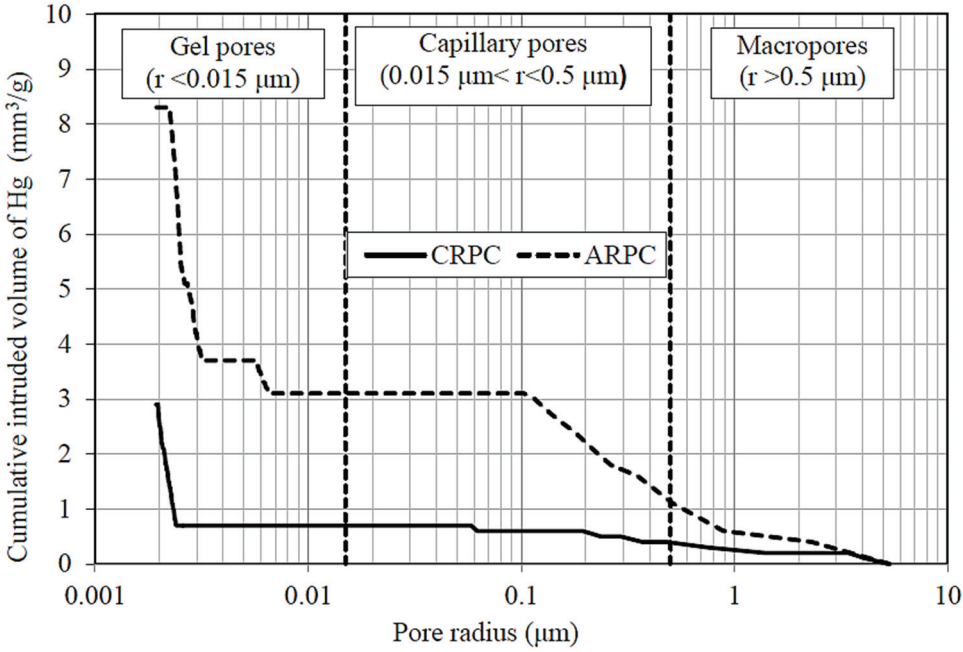

Figure 7 - Pore size distribution of ARPC and CRPC.

3.3. Rebar Corrosion

The E_{OCP}, which was measured relative to the SCE as the reference electrode, is a parameter to predict the corrosion potential of reinforcing steel in concrete (ASTMC876). ASTMC876 [21] recommends that there is a greater than 90% probability of corrosion in the case of potential less than −270 mV. A corrosion potential more positive than −120 mV shows that there is a greater than 90% probability that no corrosion is occurring. Also, an E_{OCP} value between −120 mV to−270 mV represents uncertain corrosion activity. The average E_{OCP} values of specimens kept in water and air are presented in Fig. 8. The specimens stored in air, no matter the mixture type, were in passive state at the end of the 365 days. The lack of humidity in the pore system conserved the reinforcement against the corrosion activity. Passive position of the reinforcement was valid for the CRPC specimens kept in standard water curing. It can be explained by the impermeable pore structure of CRPC, which can keep the steel bars in passive state. On the other hand, a depassivation seemed to occur at approximately 20 days for ARPC specimens in water curing. Pore structure analysis of the specimens showed that ARPC specimens had approximately 4 times greater permeable voids than CRPC specimens. Electrochemical potential activity seemed to start even in presence of humidity by ingress of water into ARPC specimens. Although, it means that corrosion activity risk was greater than 90% probability, this corrosion activity could not detected in observational and microscopic studies. Fig. 9 shows the rebars embedded in the specimens that were kept in water for 360 days. There was no evidence of corrosion on the surface of

rebars embedded in the CRPC and ARPC specimens. This finding was also supported by the by the microstructural analysis conducted on the matrix-rebar interface of these specimens.

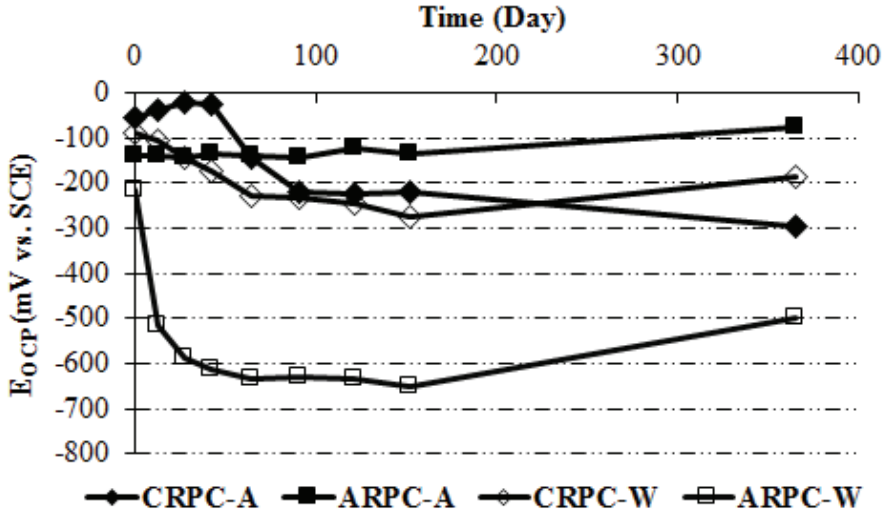

Figure 8 - E_{OCP} values of specimens in water and air

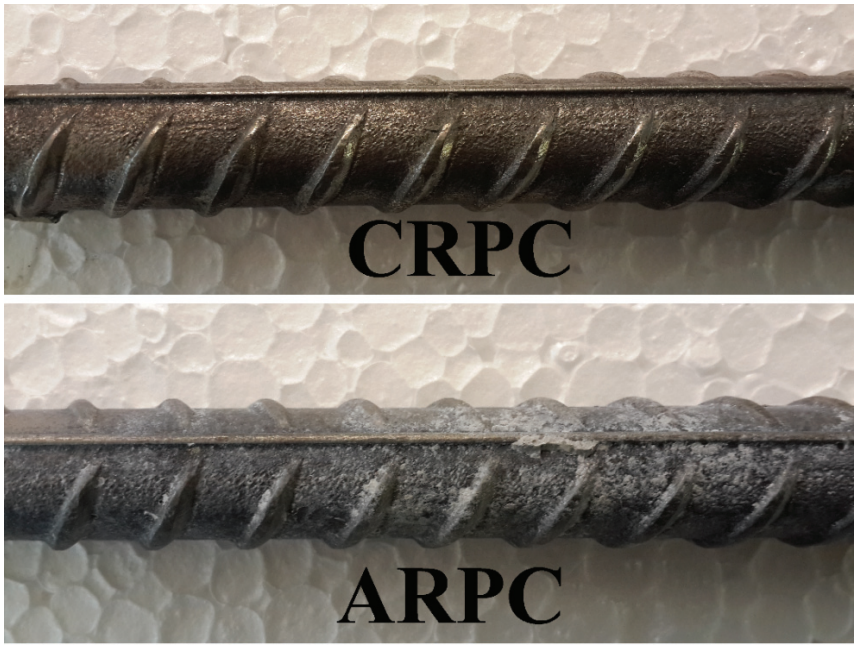

Figure 9 - The rebars embedded in the CRPC and ARPC specimens that were kept in water for 360 days.

The average E_{OCP} values of specimens subjected to wetting-drying cycles are presented in Fig. 10. According to the E_{OCP} values, there was more than 90% probability that the steel rebars embedded in the CRPC mixture were not corroded up to 400 wetting-drying cycles. However, the average E_{OCP} values of rebars embedded in the ARPC exceeded the −270 mV value and depassivation occurred even at the 50 wetting-drying cycles. The E_{OCP} values of rebars in both of the mixtures were higher than −600 mV after 1400 wetting-drying cycles that showed a high potential risk of corrosion.

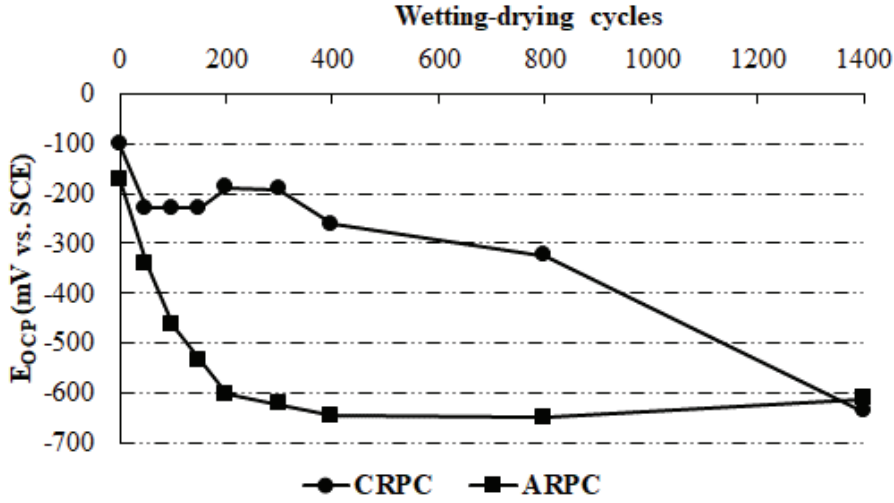

Figure 10 - E_{OCP} values of specimens subjected to wetting-drying cycles in NaCl solution.

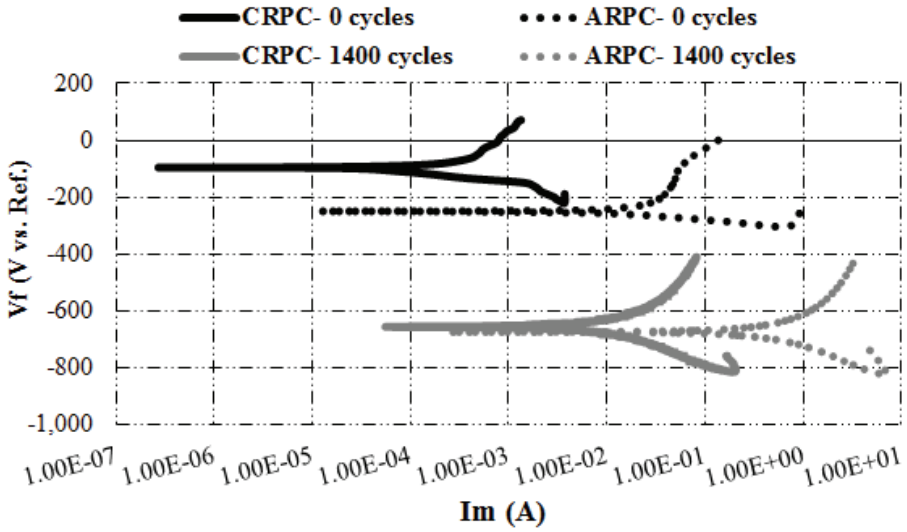

Figure 11 - Polarization curves.

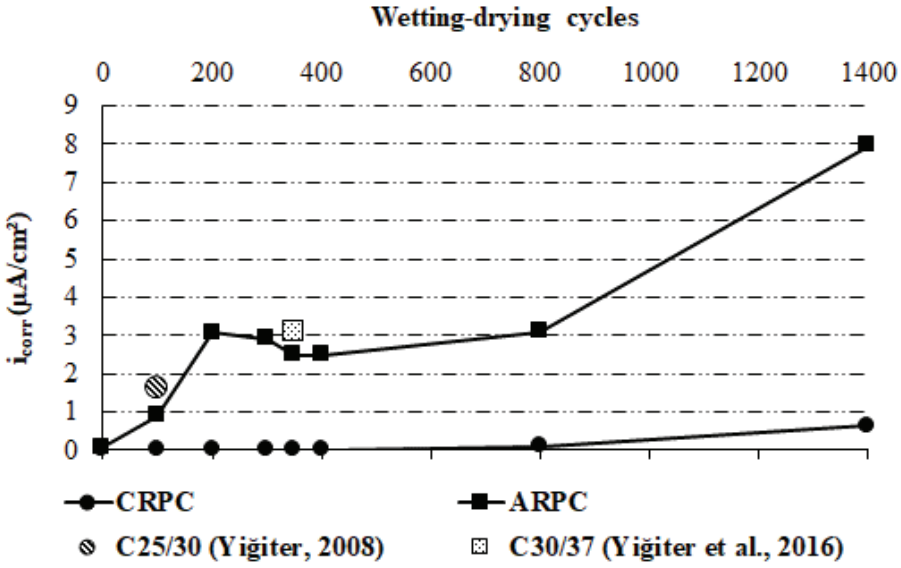

Figure 12 - i_{corr} values during wetting-drying cycles

Fig. 11 shows the polarization curves of the specimens. As expected, an increase in corrosion activity shifted the intersection of Tafel slopes to greater current and lower potential values. I_{corr} values were calculated from Tafel analysis. It can be seen from Fig. 12 that the i_{corr} values were accordance with the E_{OCP} values. After 100 wetting-drying cycles, the average i_{corr} values of the steel rebars embedded in the CRPC was lower than the 0.1 µA/cm^2 that indicates a negligible corrosion level. However, the average i_{corr} values measured in ARPC specimens was in the range of 0.5 to 1 µA/cm^2 (0.9 µA/cm^2) that indicates a moderate corrosion level. However, the average i_{corr} value of steel embedded in the CRPC can be categorized in moderate corrosion level (0.64 µA/cm^2) after 1400 cycles. It is obvious that corrosion rate of steel rebars embedded in the ARPC increased rapidly even at a low wetting-drying cycles. The average i_{corr} value of steel rebar embedded in the ARPC was in the range of 2.48 to 3 µA/cm^2 (high corrosion activity) at 200, 300, 400 wetting-drying cycles.

Yiğiter [22] reported 1.6 µA/cm^2 corrosion current density value at 100 wetting-drying cycles in 3.5% chloride solution (Fig. 12). In that study, 10 mm concrete cover and C25/30 concrete class were tested. In another study, 3.1 µA/cm^2 corrosion current density value was measured from a steel reinforcement embedded with 10 mm cover thickness in a C30/37 grade OPC concrete subjected 350 wetting-drying cycles in real sea environment [23]. From the viewpoint of corrosion activity it can be said that, ARPC reflected a similar performance to conventional OPC mixtures.

Corrosion current density higher than 1 µA/cm^2 indicates high corrosion level [24]. The average i_{corr} value of steel rebars embedded in the ARPC (7.96 µA/cm^2) was almost 13 times higher than the CRPC after 1400 wetting-drying cycles. These findings were in accordance with mass losses in the embedded rebars given in Fig. 13.

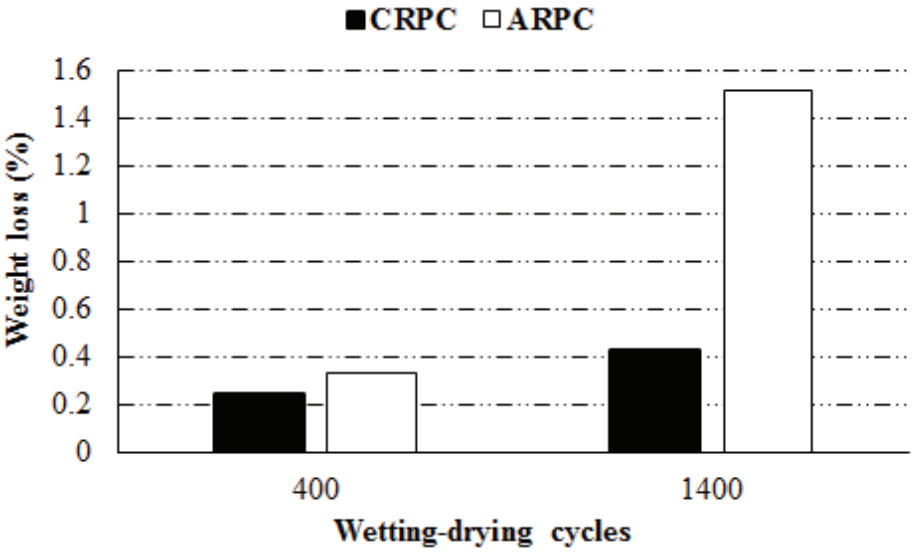

Figure 13 - Mass loss obtained from steel reinforcement

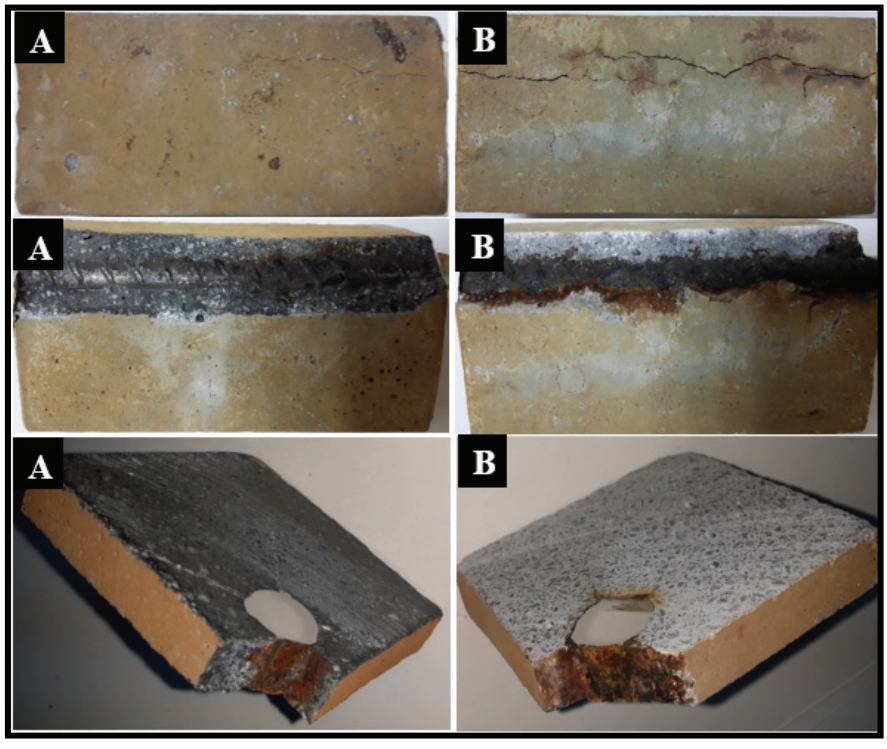

Figure 14 - A) CRPC and B) ARPC specimens after 1400 wetting-drying cycles

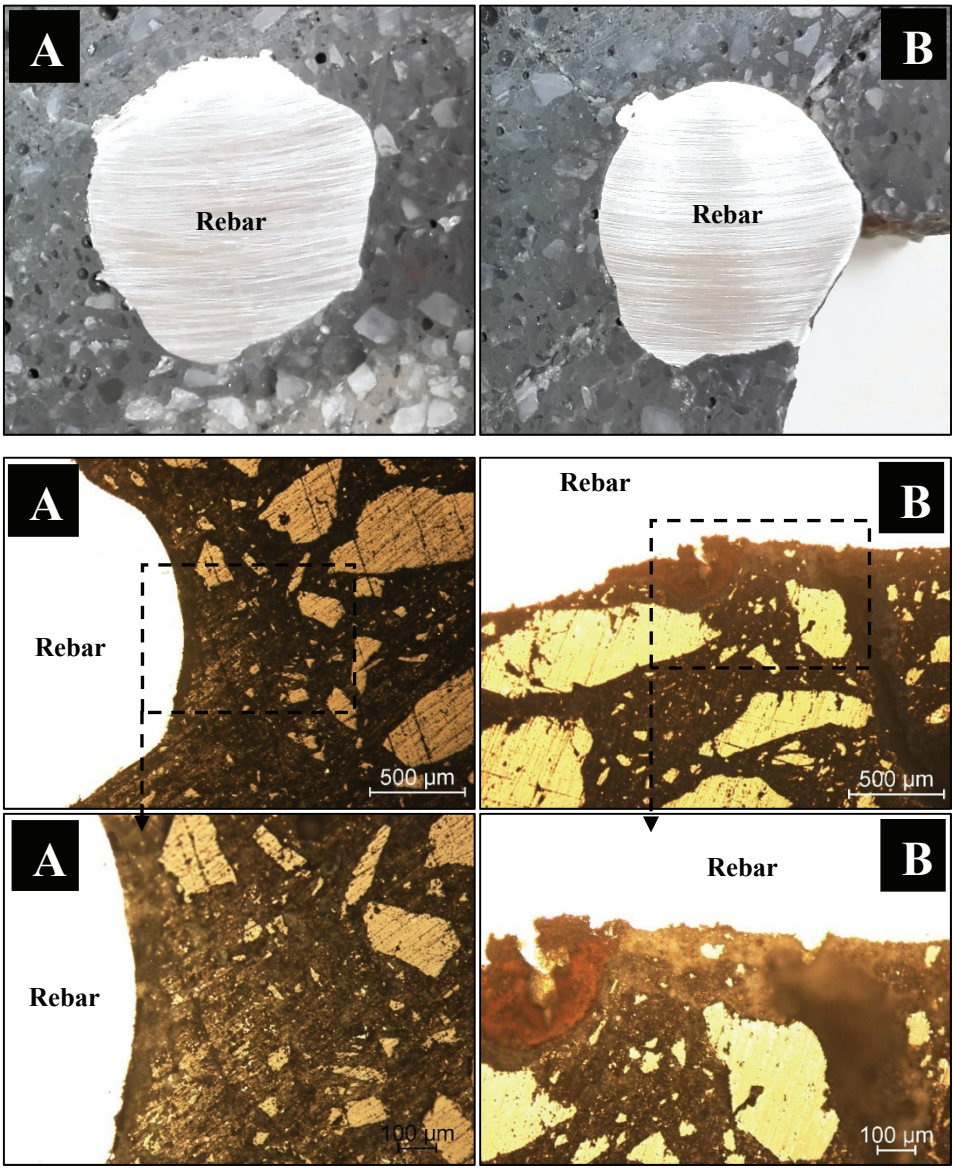

Figure 15 - A) CRPC specimen kept in water. B) CRPC specimen subjected to 1400 wetting-drying cycles.

The digital camera (DC) and optical microscope (OM) images presented in Figs. 14, 15 and 16 showed the higher corrosion-induced deterioration (after 1400 cycles) in the ARPC specimens compared in the CRPC ones. As can be seen from Fig. 14 the deterioration in concrete cover of ARPC mixture was much more obvious when compared in CRPC. Figs 15 and 16 shows the polished cross section of CRPC and ARPC specimens, respectively. It can

be seen from the DC images the inner side of rebar embedded in ARPC was also corroded, but obviously not as much as the outer side of the rebar. This corrosion led to formation of macro cracks in the ARPC matrix. In addition, OM images revealed the existence of many micro cracks in the rebar-matrix interface of ARPC mixture (Fig. 16). SEM analysis conducted on the matrix-rebar interfaces revealed the existence of higher amount of corrosion products in ARPC as compared to CRPC. Fig. 17 shows the characteristic corrosion products with different morphology in the matrix-rebar interfaces of CRPC and ARPC.

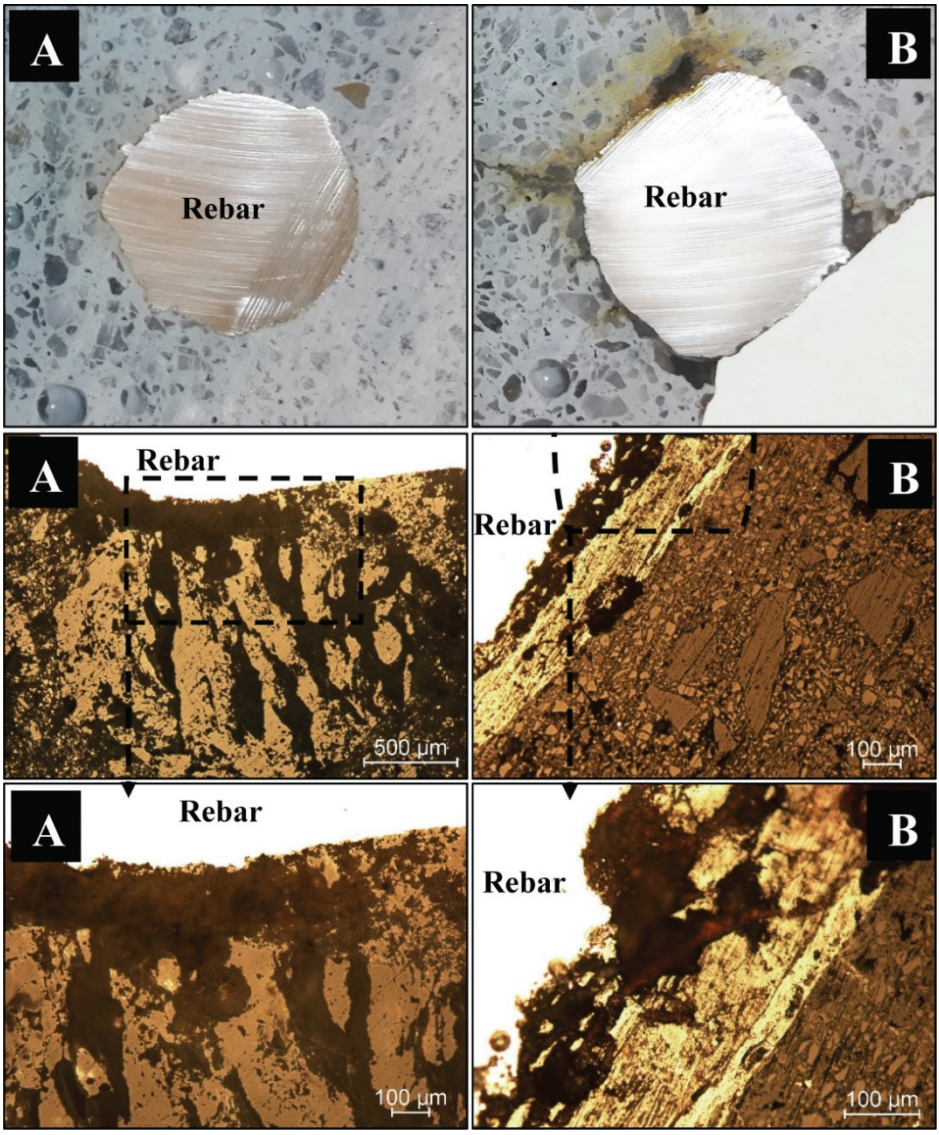

Figure 16 - A) ARPC specimen kept in water. B) ARPC specimen subjected to 1400 wetting-drying cycles.

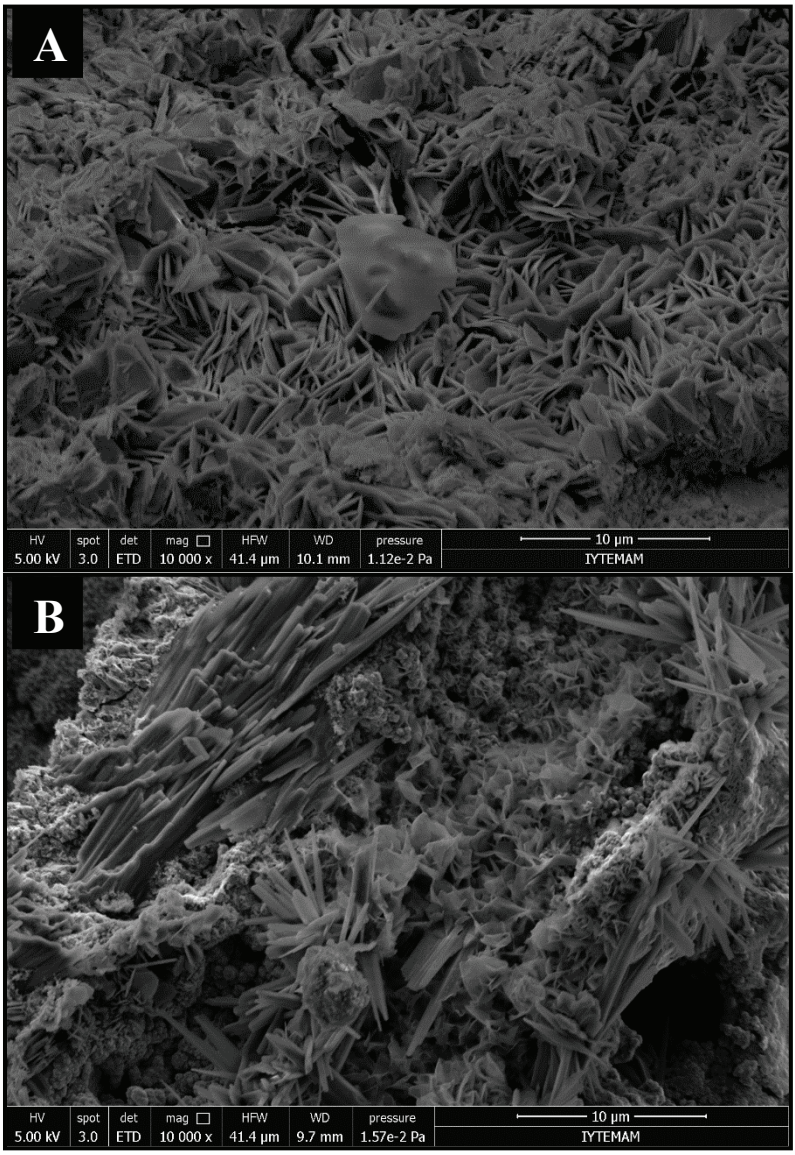

Figure 17 - SEM images of the matrix-rebar interfaces of A) CRPC and B) ARPC after 1400 wetting-drying cycles

4. CONCLUSION

Similar mechanical performance to conventional reactive powder concrete can be obtained by alkali-activated slag/silica fume, but the porosity and permeability of ARPC were much higher than CRPC. Thus, it may lead to early deppassivation of steel reinforcement. In the

case of chloride environment corrosion propagation proceeds in a higher level in ARPC mixtures. Therefore, the cracking and damage occurrence began earlier in ARPC mixtures as compared to the CRPC mixtures. On the other hand, test results showed that the electrode potential shift in water environment especially for ARPC mixtures, was not an indicator of deteriorative corrosion activity in RPC mixtures.

Acknowledgment

This study was supported by the Scientific Research Council of Dokuz Eylül University (2009.KB.FEN009). The authors gratefully acknowledge for the financial support.

References

[1] Richard, P. and M.H. Cheyrezy, Reactive powder concretes with high ductility and 200-800 MPa compressive strength. Special Publication. 144507-518, 1994.

[2] Aydın, S., Development of a Fiber Reinforced Composite with Alkali Activated Ground Granulated Blast Furnace Slag, in The Graduate School of Natural and Applied Sciences. 2010, Dokuz Eylul University: Turkey.

[3] Bonneau, O., et al., Characterization of the granular packing and percolation threshold of reactive powder concrete. Cement and Concrete Research. 30(12), 1861-1867, 2000.

[4] Ju, Y., et al., Toughness and characterization of reactive powder concrete with ultra-high strength. Science in China Series E-Technological Sciences. 52(4), 1000-1018, 2009.

[5] Aydin, S. and B. Baradan, Effect of activator type and content on properties of alkali-activated slag mortars. Composites Part B-Engineering. 57166-172, 2014.

[6] Aydin, S. and B. Baradan, Mechanical and microstructural properties of heat cured alkali-activated slag mortars. Materials & Design. 35374-383, 2012.

[7] Aydin, S. and B. Baradan, The effect of fiber properties on high performance alkali-activated slag/silica fume mortars. Composites Part B-Engineering. 45(1), 63-69, 2013.

[8] Aydin, S. and B. Baradan, Engineering Properties of Reactive Powder Concrete without Portland Cement. Aci Materials Journal. 110(6), 619-627, 2013.

[9] Aydin, S. and B. Baradan, High Temperature Resistance of Alkali-Activated Slag- and Portland Cement-Based Reactive Powder Concrete. Aci Materials Journal. 109(4), 463-470, 2012.

[10] Wang, W.R., et al., Corrosion behavior of steel bars immersed in simulated pore solutions of alkali-activated slag mortar. Construction and Building Materials. 143289-297, 2017.

[11] Ma, Q.M., et al., Chloride transport and the resulting corrosion of steel bars in alkali activated slag concretes. Materials and Structures. 49(9), 3663-3677, 2016.

[12] Holloway, M. and J.M. Sykes, Studies of the corrosion of mild steel in alkali-activated slag cement mortars with sodium chloride admixtures by a galvanostatic pulse method. Corrosion Science. 47(12), 3097-3110, 2005.

[13] Babaee, M. and A. Castel, Chloride-induced corrosion of reinforcement in low-calcium fly ash-based geopolymer concrete. Cement and Concrete Research. 8896-107, 2016.

[14] Chaparro, W.A., J.H.B. Ruiz, and R.D.T. Gomez, Corrosion of Reinforcing Bars Embedded in Alkali-activated Slag Concrete Subjected to Chloride Attack. Materials Research-Ibero-American Journal of Materials. 15(1), 57-62, 2012.

[15] Aperador, W., R.M. de Gutierrez, and D.M. Bastidas, Steel corrosion behaviour in carbonated alkali-activated slag concrete. Corrosion Science. 51(9), 2027-2033, 2009.

[16] Monticelli, C., et al., A study on the corrosion of reinforcing bars in alkali-activated fly ash mortars under wet and dry exposures to chloride solutions. Cement and Concrete Research. 8753-63, 2016.

[17] ASTM C642-13. Standard Test Method for Density, Absorption, and Voids in Hardened Concrete. 2013, ASTM International: West Conshohocken, PA.

[18] ASTM C1202-05. Standard Test Method for Electrical Indication of Concrete's Ability to Resist Chloride Ion Penetration. 2005, ASTM International: West Conshohocken, PA.

[19] Monticelli, C., et al., Corrosion behavior of steel in alkali-activated fly ash mortars in the light of their microstructural, mechanical and chemical characterization. Cement and Concrete Research. 8060-68, 2016.

[20] Najimi, M., et al., Comparative Study of Alkali-Activated Natural Pozzolan and Fly Ash Mortars. Journal of Materials in Civil Engineering. 30(6), 2018.

[21] ASTM C876-09. Standard Test Method for Corrosion Potentials of Uncoated Reinforcing Steel in Concrete. 2009, ASTM International: West Conshohocken, PA.

[22] Yiğiter, H., The Determination Of Chloride Induced Corrosion Of Rebars By Electrochemical Methods, in The Graduate School of Natural And Applied Sciences. 2008, Dokuz Eylül University: Izmir.

[23] Yiğiter, H., et al., An Investigation On The Effects Of Cement Type And Concrete Quality On Durability Of Concrete And Rebar Corrosion Under Real Seawater Exposure. 2016, TÜBİTAK-Project No: 112M899: Izmir.

[24] Andrade, C., et al., Test methods for on-site corrosion rate measurement of steel reinforcement in concrete by means of the polarization resistance method. Materials and Structures. 37(273), 623-643, 2004.

Teknik Dergi, 2020 10379-10397, Paper 595

Improvement of Flexural Performance of UHPFRC with Hybrid Steel Fiber

Altuğ YAVAŞ[1]
Tamer BİROL[2]
Kaan TÜRKER[3]
Umut HASGÜL[4]
Halit YAZICI[5]

ABSTRACT

This study investigates the flexural behavior of Ultra-High Performance Fiber Reinforced Concrete (UHPFRC) with hybrid steel fiber referencing the ASTM standard C 1609. Two types of end-hooked fibers in macro fiber concretes and one type short straight fiber in micro fiber concretes were used in mono and hybrid forms. In order to determine the flexural response of UHPFRC, a series of prismatic beam specimens with a dimension of 100 x 100 x 400 mm were tested under the four-point loading and following parameters were compared and discussed in terms of the first cracking load and pattern, flexural strength, deflection capacity, toughness and residual strength capacity under bending loads. The test results showed that as the fiber amount of specimens with the mono fiber increases, in general, better flexural behavior may be ensured. It should be also noted that the hybrid use enhanced the flexural behavior compared to the macro fiber usage.

Keywords: Ultra-high performance fiber reinforced concrete, hybrid fiber, steel fiber, flexural behaviour.

Note:
- This paper has been received on November 20, 2018 and accepted for publication by the Editorial Board on December 4, 2019.
- Discussions on this paper will be accepted by January 31, 2021.
- https://doi.org/10.18400/tekderg.485565

1 Balikesir University, Department of Civil Engineering, Balıkesir, Turkey - ayavas@balikesir.edu.tr - https://orcid.org/0000-0002-2619-8671

2 Balikesir University, Department of Civil Engineering, Balıkesir, Turkey - tbirol@balikesir.edu.tr - https://orcid.org/0000-0003-2428-6202

3 Balikesir University, Department of Civil Engineering, Balıkesir, Turkey - kturker@balikesir.edu.tr - https://orcid.org/0000-0002-3106-4627

4 Balikesir University, Department of Civil Engineering, Balıkesir, Turkey - hasgul@balikesir.edu.tr - https://orcid.org/0000-0002-9358-3369

5 Dokuz Eylul University, Department of Civil Engineering, İzmir, Turkey - halit.yazici@deu.edu.tr - https://orcid.org/0000-0002-0921-9709

1. INTRODUCTION

Over the last two decades, the production of Ultra-High Performance Concrete (UHPC) has become possible with new developments in concrete technology. This concrete is produced with high density matrix, very low water/binder ratio and special treatments such as curing under heat/pressure. Though these types of special concretes possess high compressive strength, their behavior is more brittle [1-3]. In order to decrease brittleness and to ensure high amount of energy absorption and ductility as well as bearing capacity for these types of special concretes, steel fibers are added to the concrete mixture. This type of concrete is widely known as the Ultra-High Performance Fiber Reinforced Concrete (UHPFRC) [4]. The UHPFRC has various advantages over conventional concrete and fiber reinforced concrete such as higher durability, ductility and strength because of its low porosity, dense matrix, high tensile/compressive strength and ductile tensile behavior [5]. This kind of concrete responds very high durability through the high density and crack-bridging of steel fibers. Thus, this material is classified as the Ultra-High Performance Fiber Reinforced Concrete (UHPFRC) or High Performance Fiber Reinforced Cement Composite (HPFRCC).

The UHPFRC doesn't have a widespread use due to its difficult and high cost production. For this reason, low cost and easily producible UHPFRC studies (with ordinary raw materials, standard curing conditions and mixers) have gained momentum in the recent years and successful results have been achieved [4, 6-12]. Therefore, it has become possible and widespread to use the UHPFRC in conventional reinforced concrete construction.

Even though several studies were carried out, there is no authority or standard to classify the term "high performance". However, some conditions for this classification, such as the uni-axial compressive strength and pseudo strain-hardening under tension or bending, are expected to be improved in some way [13-16]. The pseudo strain-hardening response can be ensured with a good amount of fiber content. However, insufficient fiber volume fraction and/or low concrete compressive strength may lead to softening response under tension or bending types of loading [17].

Almost all fibrous concretes used commercially today involve the use of a single fiber type. Clearly, a given type of fiber can only be effective in a limited range of crack opening and deflection. In order to improve the performance of UHPFRC, one of the promising methods is to blend together two or more steel fiber types in a matrix since the micro and macro steel fibers play a role at two different levels depending on the length and diameter of fibers. In hybrid fiber reinforced concrete, the micro fibers improve the strength and stiffness in the pre-peak region since crack widths are still small. The macro fibers limit the formation of wide (major) cracks occurring at the point where a single crack widens due to crack localization. The micro fibers also improve pull-out response of the macro fibers and thereby produce composites with high strength and toughness [5, 18-21].

The inclusion of steel fibers at high dosages has potential disadvantages due to poor workability and increased cost. The cost of steel fiber of 1.0% by volume applied in the UHPFRC is generally higher than that of matrix. Hence, it is important to minimize the fiber amount without sacrificing the superior performance of UHPFRC [5]. Taking into account the cost/performance ratio for this kind of material, it is necessary to optimize its industrial use.

In recent studies regarding the impact of hybrid fiber use to mechanical properties of the UHPFRC, different sized steel fibers [5, 18-25] and usage of both steel and synthetic fibers [2, 26-32] were combined in the concrete mixtures. It can be summarized from these studies that hybrid fiber use leads to an increase in the energy absorption capacity and it improves the cracking response in comparison to mono fibers. Thus, new research on the impact of different configurations are needed in order for them to be used in the UHPFRC matrix.

The primary objective of this study is to investigate the flexural behavior of UHPFRC with hybrid steel fiber content and to compare it with the mono form. Another purpose of the study is to produce the UHPFRC under standard curing conditions and with standard mixers. In the hybrid mixtures, the high-strength micro steel fiber which is commonly used in UHPFRCs, and two types of macro steel fibers which have lower strength and cost (almost half of the micro fiber in cost), were used together. In the research study, various prismatic beam specimens, which have different fiber volume fractions in the mono as well as the hybrid forms, were produced and tested under the four-point loading in conformity with the ASTM standard C 1609 [33]. Test parameters including the first cracking load, cracking pattern, flexural strength, deflection capacity, toughness values and residual strength capacity were discussed on the mono and hybrid fiber specimens. In addition, the compressive strengths and elastic modulus (young's modulus) values of cubic and cylinder samples were determined for different fiber configurations.

2. EXPERIMENTAL STUDY

2.1. Material and Specimen Preparation

The cement (*C*) used in this study was Portland cement CEM I 42.5 R. However, two different types of supplementary cementitious materials were used, the names of which are well-known ground granulated blast-furnace slag (*GGBS*) and silica fume (*SF*). The chemical and physical properties of the *C*, *GGBS* and *SF* are presented in Table 1. Two sizes of quartz sand, the particle sizes in the range of 0 to 0.8 mm (*QS*1) and 1.0 to 3.0 mm (*QS*2), were chosen as aggregate. The gradings and cumulative curves for each aggregate and the total mixture are given in Figure 1. The specific gravities of 0-0.8 mm and 0-3 mm quartz sands were respectively 2.68 g/cm^3 and 2.66 g/cm^3. A polycarboxylate ether-based superplasticizer (*SP*) with the density of 1.08-1.14 kg/litre was used to ensure good workability. The final proportions for each fiber volume fraction and the fresh state properties of UHPFRC mixtures are summarized in Table 2.

In the study, two types of end-hooked steel fibers (aspect ratios: 30/0.55 and 60/0.75) in the macro mixtures and one type short straight steel fiber (aspect ratio: 13/0.16) in the micro mixtures were considered for the mono and hybrid forms. The brass coated high-strength steel having a smooth surface was used for the micro-sized fibers. However, the macro fibers have end-hooked geometry to improve the interfacial bond stress between the steel fiber and cementitious matrix. In addition, the macro fibers are cheaper and have longer bond length, but have lower tensile strength compared to the micro-sized fibers.

A standard pan mixer with a 90 litre capacity was used to prepare the test specimens. The *C*, *GGBS*, *SF* and *QS*s were mixed for about 3 minutes. Water and half of the *SP* were added into the mixture and mixed for another 5 minutes. Then the rest of *SP* was added and mixed

for additional 5 minutes. Later on, the fibers were dispersed carefully into the mixture and mixed until homogenously distributed.

Table 1 - Chemical composition of cementitious materials

Composition (%)	C	SF	GGBS
SiO_2	19.80	90-93	41.49
Al_2O_3	5.47	0.4-0.9	16.34
Fe_2O_3	3.46	1.0-2.0	0.61
CaO	64.44	0.2-0.7	29.26
MgO	1.30	0.9-1.3	7.68
SO_3	2.67	-	1.90
Na_2O	0.40	0.2-0.6	0.80
K_2O	0.67	1.0-1.3	1.10
Cl	0.012	-	0.01
Fe_2O_3	-	1.0-2.0	-
Specific surface (m^2/kg)	380	20000	-
Density (g/cm^3)	3.13	2.10	-

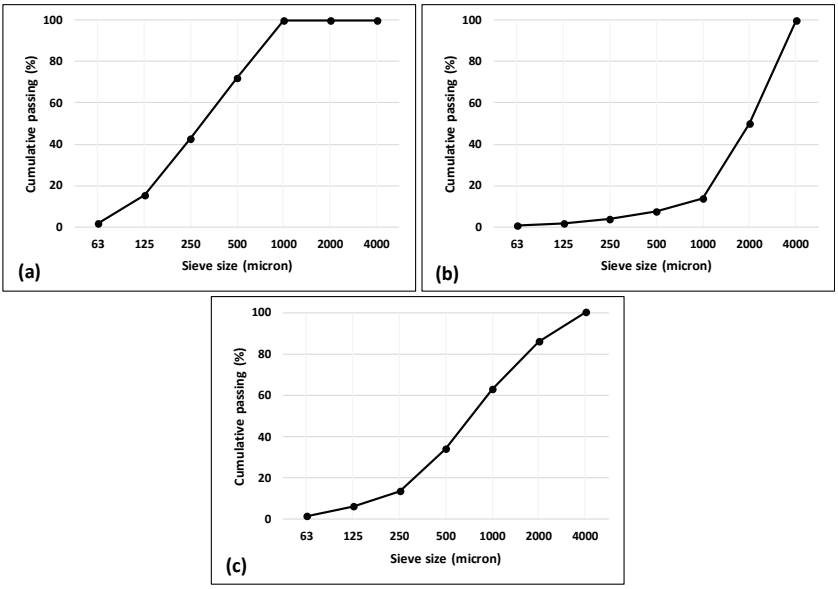

Fig. 1 - The grading and cumulative curve for the aggregates; a) QS1, b) QS2, c) mix

The prismatic beam specimens corresponding to total of 18 mixtures were produced to study the effect of different fiber contents. As summarized in Table 3, nine of the configurations

consist of the mono form while eight of them are in the hybrid form. The remaining one is the reference specimen without the steel fiber to see the contribution of the fiber content.

Table 2 - Mixture proportions of the UHPFRC by weight (kg/m³) and fresh state properties

	Fiber content	*C*	*SF*	*GGBS*	*QS1*	*QS2*	Water	*SP*	Slump flow (mm)	t_{500} (sn)
	Reference	690	138	276	542	542	199	17.25	900	2.1
Mono	13(1.0)	690	138	276	530	530	199	17.25	780	2.7
Mono	30(1.0)								805	3.1
Mono	60(1.0)								840	3.3
Mono	13(1.5)	690	138	276	525	525	199	17.25	760	3.2
Mono	30(1.5)								775	3.2
Mono	60(1.5)								800	3.5
Hybrid	13(0.5)30(1.0)	690	138	276	525	525	199	17.25	771	3.3
Hybrid	13(1.0)30(0.5)								767	3.2
Hybrid	13(0.5)60(1.0)								780	3.4
Hybrid	13(1.0)60(0.5)								773	3.2
Mono	13(2.0)	690	138	276	520	520	199	17.25	750	4.1
Mono	30(2.0)								755	3.9
Mono	60(2.0)								770	3.4
Hybrid	13(1.0)30(1.0)	690	138	276	520	520	199	17.25	755	3.9
Hybrid	13(1.5)30(0.5)								758	4.0
Hybrid	13(1.0)60(1.0)								751	3.8
Hybrid	13(1.5)60(0.5)								753	4.0

V_f: Fiber volume fraction, Water/binder= 0.18, Water/cement= 0.29

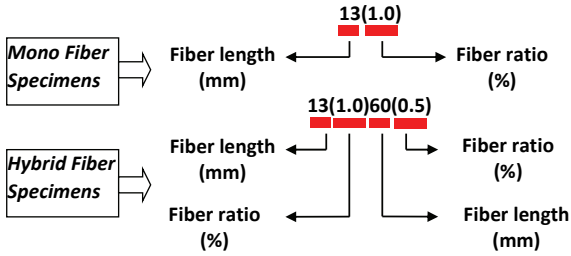

Fig. 2 - Specimen notations

The fiber volume fractions of 1.0, 1.5 and 2.0% were chosen to obtain deflection hardening behavior as well as ensure good workability. In the study, the specimen definitions were classified in terms of the considered fiber types and volume fractions. The notations of test

specimens indicating the mono and hybrid forms are shown in Figure 2. For example, 13(1.0) denotes the test specimen including the micro steel fiber of 13 mm with 1% by volume in the mono form, while the 13(1.0)60(0.5) shows the hybrid specimen containing the micro fiber of 13 mm (1% by volume) and the macro fiber of 60 mm (0.5% by volume).

For each mixture, six cubic samples with size of 100 mm, two cylinder samples with 100 mm diameter by 200 mm height as well as three prismatic beams with a square section of 100 mm x 100 mm and length of 400 mm were casted as shown in Figure 3a. The mixture was placed into the prismatic molds from one end to other by means of a plastic bucket. During the placement process, no vibration was conducted to prevent fiber gravitation. In the study, a more workable UHPFRC mixture was produced than those of presented in the previous studies [6-9]. As shown in Table 2, the slump flow value for the non-fiber mixture was measured as 900 mm. However, this value for the micro, macro and hybrid mixtures were measured in the range of 750 to 780 mm, 770 to 850 and 760 to 840 mm, respectively.

Table 3 - Fiber contents, compressive strengths and elastic modulus of the specimens

Fiber content	Specimen	Fiber volume content (%)			Compressive strength (MPa)	Elastic modulus (GPa)
		13/0.16	30/0.55	60/0.75		
Non-fiber	Reference	-	-	-	90	38
Mono fiber specimens	13(1.0)	1.0	-	-	120	42
	13(1.5)	1.5	-	-	134	45
	13(2.0)	2.0	-	-	132	42
	30(1.0)	-	1.0	-	117	45
	30(1.5)	-	1.5	-	121	42
	30(2.0)	-	2.0	-	114	41
	60(1.0)	-	-	1.0	114	40
	60(1.5)	-	-	1.5	121	42
	60(2.0)	-	-	2.0	119	44
Hybrid fiber specimens	13(0.5)30(1.0)	0.5	1.0	-	121	45
	13(1.0)30(0.5)	1.0	0.5	-	114	44
	13(1.0)30(1.0)	1.0	1.0	-	128	45
	13(1.5)30(0.5)	1.5	0.5	-	132	41
	13(0.5)60(1.0)	0.5	-	1.0	114	40
	13(1.0)60(0.5)	1.0	-	0.5	123	43
	13(1.0)60(1.0)	1.0	-	1.0	129	41
	13(1.5)60(0.5)	1.5	-	0.5	136	43

The slump-flow tests showed that the fiber content (amount and type) had a significant effect on the flow ability of UHPFRC (Table 2). As the fiber amount increases, the spread values decrease for all fiber types. For the mono form, the spread values obtained for the macro fibers were greater than the micro fiber use. Although there was no significant trend in the

hybrid form, the spread values showed a decreasing trend with increasing fiber amount. It was seen from the t_{500} values that the viscosity of concrete increased with respect to the mono form as a result of multiple fiber use in the mixture (Table 2).

After casting, the specimens were covered by plastic sheets and stored at room temperature. Twenty-four hours later, the specimens were taken out of their molds and stored in a water tank at approximately 20°C until the test day. All specimens were tested at 28 days.

For each prepared mixture, the cubic and cylinder samples were tested separately to measure the compressive strength and elastic modulus, respectively. The compression tests were conducted by a testing machine with a maximum load capacity of 3000kN. In addition, the values of elastic modulus were determined using a compressometer which measures the average compressive strain of two linear voltage differential transformers (LVDTs) as shown in Figure 3b. The average compressive strengths and elastic moduli corresponding to the non-fiber, mono and hybrid fiber specimens are given in Table 3.

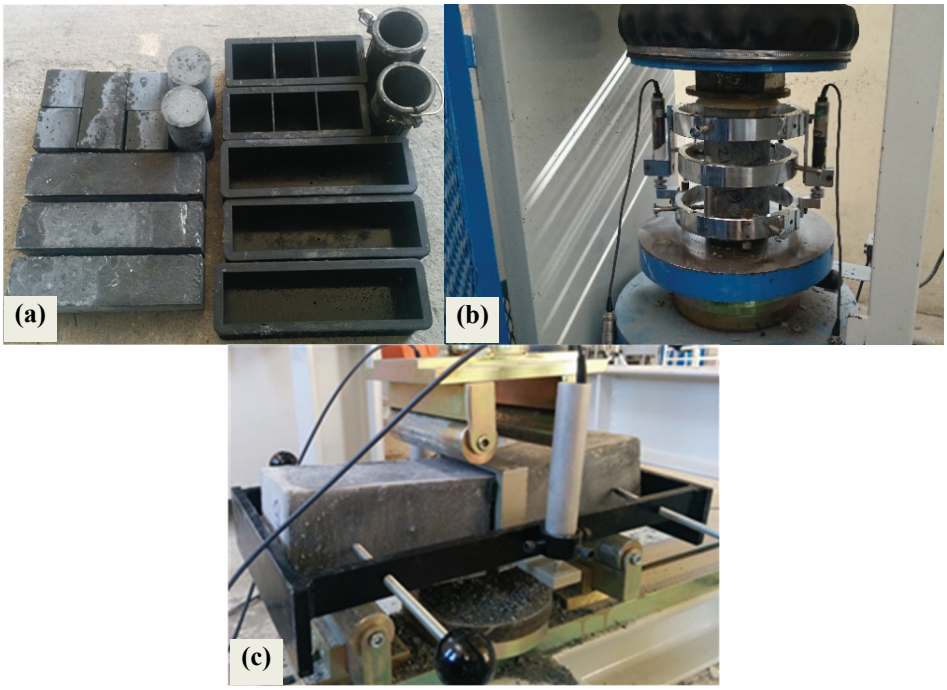

Fig. 3 - Test specimens and set-ups;
a) test specimens, b) compression test set-up and c) flexural test set-up

2.2.1. Flexural test

The flexural behavior of fiber reinforced concretes has two distinctive regions, which consist of the deflection hardening and softening behaviors depending on load carrying capacity after

first cracking [5]. Figure 4 illustrates a sample load-deflection curves denoting all calculation parameters. Referring to Figure 4, the peak load (P_p) is greater than the first-peak load (P_1) in the deflection hardening behavior whereas both the peak loads are at the same point for the softening behavior. The first-peak load is defined as the value of load corresponding to the first point on the load-deflection curve where the slope is zero. The peak load is defined as the maximum value obtained prior to reaching the end-point deflection on the load-deflection curve. Thus, the peak and first-peak strength values can be calculated by the formula (Equation 1) for modulus of rupture in ASTM C 1609 [33]:

$$f = \frac{PL}{bd^2} \tag{1}$$

where f denotes the strength, P is the load; b, d and L are the width, depth and length of specimen, respectively.

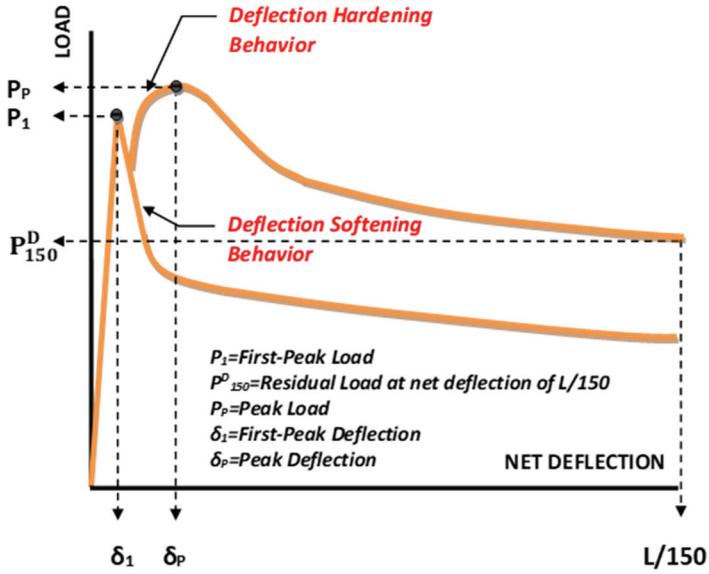

Fig 4 - Calculation parameters on a sample load-deflection curve [33]

The deflection limit of $L/150$ is based on calculation of the energy dissipation capacity (toughness) related to the total area under the load-deflection curve, as shown in Figure 4. The peak load deflection (δ_P) is the net deflection value, measured at the mid-span of beam specimen, corresponding to the peak load on the load-deflection curve.

The flexural tests were conducted under four-point loading on the simply supported beam specimens with a clear span of 300 mm, according to the ASTM C 1609 [33], as shown in Figure 3c. Three beams were considered to determine the flexural behavior of each mixture. The test was conducted on a servo hydraulic testing machine having a capacity of 200 kN. The test machine is controlled by displacement during the whole process to obtain the load

versus deflection behavior. The speed of applied displacement increments throughout the entire test program was 0.1 mm/min. The load was divided into two equal loads, providing a distance of 100 mm between them through a spreader beam. Later, the load was measured with a load cell which was placed between the cross head and spreader beam. To obtain the average mid-span deflection, two LVDTs were attached on the both sides of specimen with the help of a steel frame excluding the beam settlements at the supports. The applied loads and mid-span deflections were recorded through the data acquisition system during the test procedure. The detailed test procedure can be found in the ASTM C 1609.

In order to minimize the influence of non-uniform fiber distribution, the top or the bottom surface of the specimen was rotated to the side in order to take measures prior to the bending test. Note that all specimens showed uniform fiber distribution.

3. RESULTS

3.1. Compressive Strength and Elastic Modulus

Test results of average compressive strengths and elastic modulus values are presented in Table 3. Here, the compressive strength values were obtained from the cubic samples and the elastic moduli were obtained from the cylinder samples. The results showed that macro fiber use increased the compressive strength by an average of 31% compared to the non-fiber mixture. Similarly, use of micro and hybrid fiber increased the compressive strength by 43% and 39%, respectively. Regardless of the fiber content, it is apparent that the compressive strengths for both the mono and hybrid forms are much greater than that of the non-fiber mixture, as would be expected. It was also noted that use of micro fiber was more impactful to the relation between macro fibers and compressive strength. Although the compressive strength tends to increase as the volumetric fraction changes from 1.0% to 1.5%, when the fiber fraction increases further, such as from 1.5% to 2.0%, the compressive strength may decrease somewhat. But, this deduction for the hybrid fiber samples is distinctive since the average compressive strength showed increasing tendency when all amount of the fibers were considered (Table 3). The test results on cylinder samples also showed that the fiber content has no significant effect on the elastic modulus so that the average elastic modulus for all specimens containing the steel fiber were determined as about 42.6 GPa.

3.2. Flexural Behavior

In the study, three beam specimens corresponding to each fiber configuration were tested under the four-point loading and their load-midspan deflection behavior was obtained. The intermediate one among the three responses in terms of the flexural strength and toughness was chosen for the purpose of comparisons and evaluations [34]. The standard deviations related to these quantities for each fiber type considering three specimens and the characteristic values for the intermediate specimens are summarized in Table 4. For each volume fraction, the load versus midspan deflection responses corresponding to the selected specimens having the mono fiber forms are shown in Figures 5a-5c.

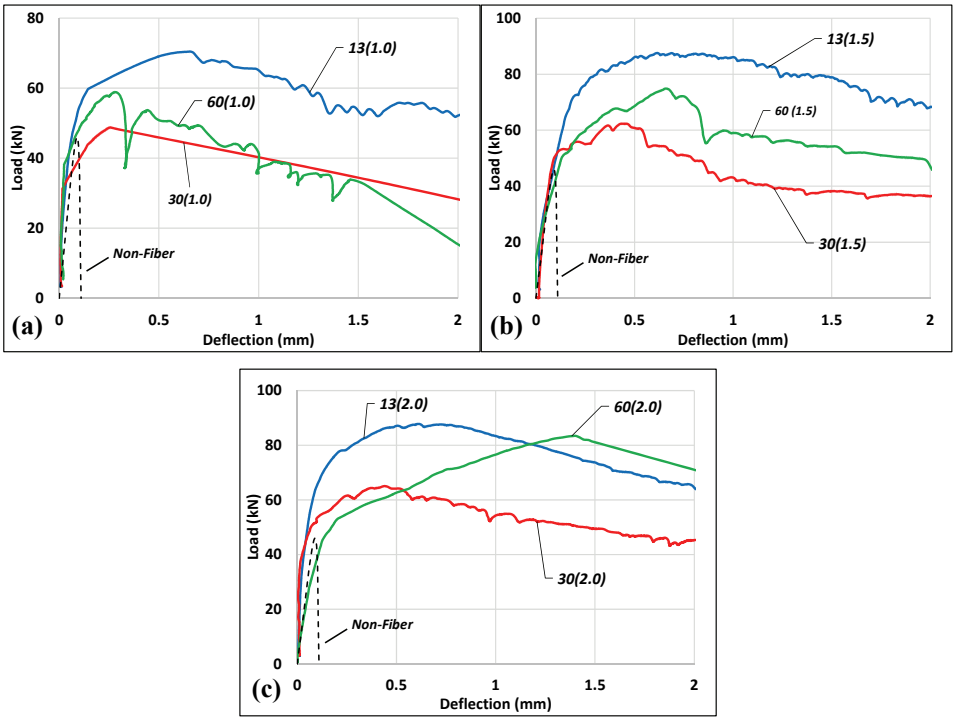

Fig. 5 - Load-deflection curves of UHPFRC specimens with mono steel fiber; a) 1.0% volumetric fraction, b) 1.5% volumetric fraction, c) 2.0% volumetric fraction

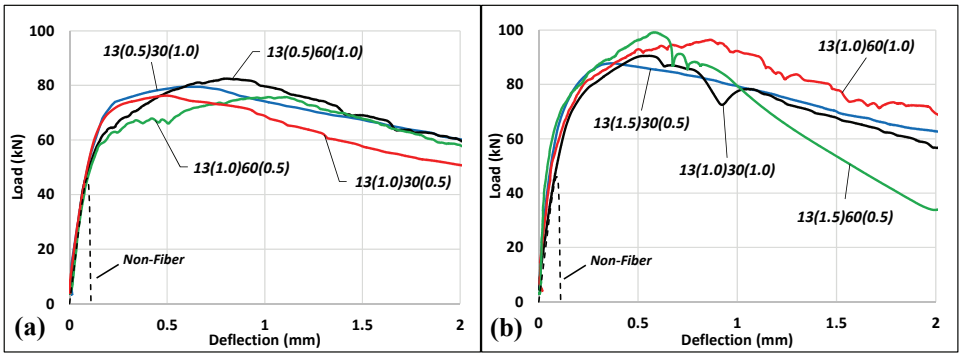

Fig. 6 - Load-deflection curves of UHPFRC specimens with hybrid steel fiber; a) 1.5% volumetric fraction, b) 2.0% volumetric fraction

It is apparent from Figures 5a-5c that use of mono fiber provided significant gain in strength and deflection hardening capacity. These parameters show an increasing trend when the volume fraction goes up from 1.0% to 1.5%. It was also noted that as the fiber amount

increases further, up to 2.0% by volume, the performances of specimens with micro fiber remains limited as shown in Figure 5a-5c. However, the test specimens with the macro fiber sustained their increasing trend.

As shown from the load-deflection responses with the hybrid fiber (Figures 6a-6b), a small increment in the fiber volume fraction from 1.5% to 2.0% may lead to an increase in the strength and toughness capacities of the specimens.

Table 4 - The parameters related to flexural strength of specimens

Notation	P_1 (kN)	P_P (kN)	δ_P (mm)	P^D_{150}/P_p	f_P (MPa)	T (kNmm)	Standard deviation for three responses	
							Std (f_P)	*Std* (T)
Reference	-	45.98	0.06	-	13.29	2.1	1.51	-
13(1.0)	15.8	70.47	0.66	0.74	21.14	122	0.27	6.03
13(1.5)	27.0	87.58	0.61	0.78	26.27	159	2.94	16.46
13(2.0)	26.8	87.81	0.61	0.73	26.34	148	2.80	17.62
30(1.0)	*	48.78	0.26	0.58	14.63	76	1.51	8.62
30(1.5)	25.0	62.33	0.46	0.58	18.70	93	1.57	3.51
30(2.0)	*	65.05	0.44	0.70	19.52	109	2.36	16.17
60(1.0)	*	58.88	0.28	0.26	17.66	85	0.83	2.52
60(1.5)	23.2	74.88	0.66	0.63	22.46	118	2.77	14.05
60(2.0)	28.0	83.45	1.40	0.85	25.04	138	2.82	15.87
13(0.5)30(1.0)	26.0	74.49	0.65	0.81	22.35	127	2.31	13.20
13(1.0)30(0.5)	24.8	76.24	0.50	0.67	22.87	127	0.79	17.35
13(1.0)30(1.0)	25.4	90.51	0.56	0.63	27.15	146	1.83	2.08
13(1.5)30(0.5)	23.5	87.78	0.37	0.71	26.33	179	1.89	15.10
13(0.5)60(1.0)	24.0	82.74	0.80	0.73	24.74	142	2.52	14.64
13(1.0)60(0.5)	25.5	75.72	1.02	0.77	22.72	133	2.76	17.90
13(1.0)60(1.0)	21.3	96.42	0.86	0.72	28.39	168	2.39	14.19
13(1.5)60(0.5)	*	99.15	0.58	0.34	29.75	163	2.09	17.79

*: Could not be determined

3.2.1. First Cracking Load and Cracking Pattern

The first cracking loads (P_1) related to the test specimens were determined from the load-deflection curves. In this way, the specific point where the initial stiffness of curve changes, was taken as the cracking point. It is interesting to note that whereas this point was directly captured for many specimens, some load-deflection curves did not show this point distinctly. The numerical results regarding to the first cracking loads are summarized in Table 4.

- The first cracking loads of specimens with micro fiber, as expected, were higher than those of the macro fiber specimens, because the crack widths were very small prior to the peak load.

- The cracking response of the hybrid specimens could differ depending on the amount of micro and macro fibers considered in the mixture. The hybrid specimens containing the macro fibers of 30 mm showed better performance than that of the 60 mm macro fibers, in terms of the first cracking load. The greatest value for this parameter was obtained when the steel fiber content was increased to 2.0% by volume.

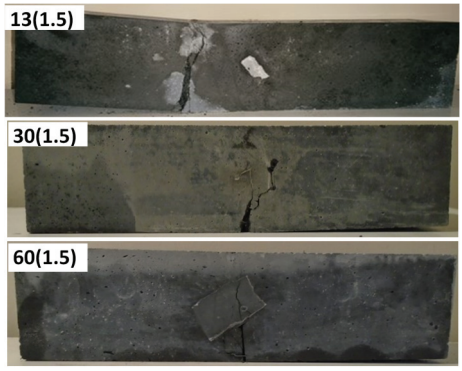

Fig. 7 - Cracking patterns of UHPFRC specimens with mono steel fiber

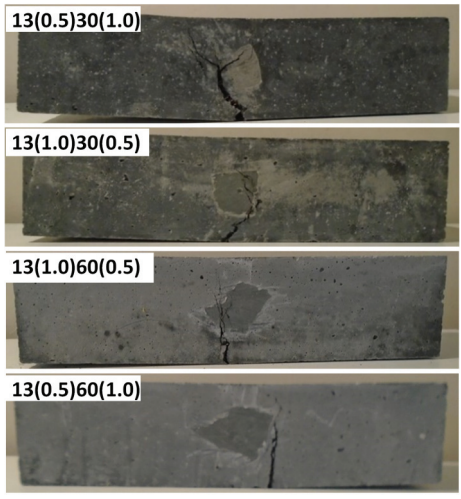

Fig. 8 - Cracking patterns of UHPFRC specimens with hybrid steel fiber

It is apparent that use of micro fiber is more successful in preventing crack formation compared to macro fibers. Similarly, as the volumetric ratio of micro fibers increases in the hybrid specimens, the first crack initiated at higher loads. It was also noted that an increase in the volume fraction governs the crack response due to the crack-bridging ability of steel fibers. After the first cracking point, a large number of closely-spaced micro cracks, which

are not easy to see with naked eyes until the peak load, formed at the mid-span region of specimens. In all UHPFRC specimens, a major crack initiated at the point where a single crack widened due to crack localization over the half of the span. Consequently, flexural failure occurred as a result of this crack. Regardless of mono or hybrid usage, this phenomenon is distinctive for conventional fibrous concretes and it was observed from this study that the fiber content has no specific effect on this behavior. In the study, the mono and hybrid specimens' failure patterns were given for only volume fraction of 1.5% in Figures 7 and 8, for sake of brevity.

3.2.2. Flexural Strength, Deflection Capacity, Toughness and Residual Load Ratio

For each test specimen, the flexural strength, toughness, peak load, as well as the deflection capacity at the peak load were determined from the load-deflection curves (Table 4). The importance of fiber type and amount on retaining load carrying capacity after the peak load was studied through the term "residual load ratio", which represents the residual capacity and strength loss on a load-deflection relationship. This ratio was calculated by dividing P^{D}_{150} to P_p and was presented for all test beams in Table 4.

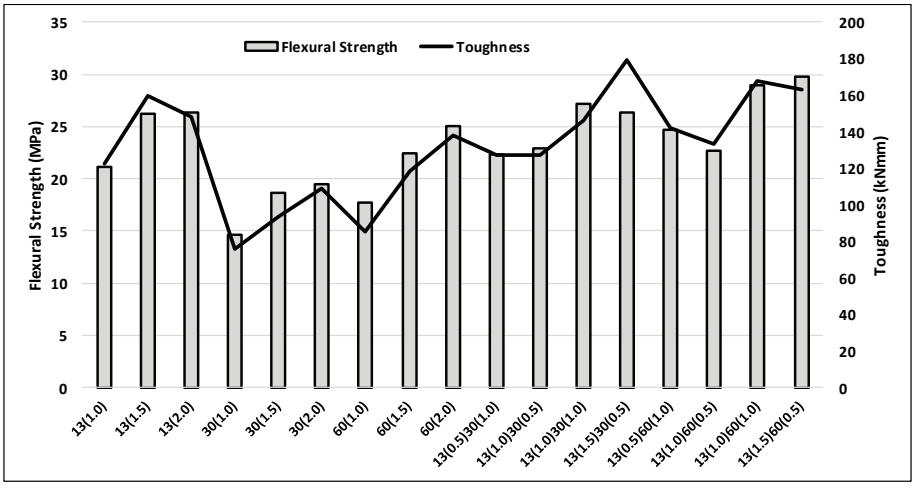

Fig. 9 - Comparison of the flexural strength and toughness performances of specimens

Table 5 - Statistical results for each volumetric fiber ratio

V_f (%)	Flexural strength			Toughness		
	μ (MPa)	*Std*	*CoV*	μ (kNmm)	*Std*	*CoV*
1.0	17.81	3.26	0.18	81	6.67	0.08
1.5	22.87	2.34	0.10	129	15.24	0.12
2.0	26.15	3.34	0.13	150	23.11	0.15

The toughness values for all specimens were calculated using the total area under the related load-deflection curve. The variations of flexural strength and toughness values with the fiber contents are shown in Figure 9. The mean (μ), standard deviation (*Std*) and coefficient of variation (*CoV*) were also calculated for each volume fraction (Table 5).

After conducting a series of tests, the performances related to flexural strength and toughness are discussed as follows:

- Comparing the flexural strengths of the mono and hybrid specimens to the non-fiber specimen, use of micro and macro fiber increased the strength by a range of 59% to %98 and 10% to 88%, respectively. It was shown, however, that hybrid fiber use increased the strength by up to 124% depending on the fiber content.
- The toughness performances of the test specimens showed a great variety. While the toughness values of the micro fiber specimens increased by a range of 58 to 76 times compared to the non-fiber form, these changes were smaller for the macro fiber specimens (ranged from 36 to 66 times). It can be noted that use of hybrid fiber use increased these ratios by 60 to 85 times.
- The best performance among the test specimens with the mono fiber was obtained when 2.0% micro fiber was included in the UHPFRC mixture. However, the best performance from the point of macro fiber use was obtained for the steel fiber of 60 mm. But the lowermost performance was obtained for the specimen containing the 30 mm macro fiber with 1.0% by volume.
- The test results showed that the best performance for the hybrid fiber specimens was obtained when the volume fraction of 2.0% was used. Among those, the specimens having the macro fiber of 60 mm showed, in general, better performance.
- When the hybrid fiber specimens were compared to those with macro fibers in the mono form, apparent improvements were seen on the flexural strength and toughness for all fiber contents.
- The specimens containing 1.5% micro fiber showed better performance compared to the hybrid specimens with the same content. In contrast to this behavior, the hybrid fiber specimens (especially those containing macro fibers of 60 mm) with 2.0% fiber content showed better performance compared to the micro fiber specimens.

Consequently, inclusion of micro fibers in the UHPFRC mixture resulted in better performance than the macro fibers, in terms of the flexural strength and toughness of the specimens. It was also observed that even higher values can be obtained by using hybrid fibers compared to using micro and macro fibers in the mono form.

Since first-cracking occurred at small load values, the deflection capacities of the specimens are same with the ultimate deflections on the hardening region after the cracking load. Referring to Table 4, when the performances of the specimens are evaluated in terms of their deflection capacities, the following discussions can be made.

- The best deflection capacity among the test specimens with the mono fiber was obtained when the macro steel fiber of 60 mm was used with the volume fraction of

2.0%. On the other hand, the lowermost performance was obtained for the mono specimens containing 60 mm macro steel fibers of 1.0% by volume.

- The hybrid specimens containing the 60 mm macro fiber showed considerably better performance than those with 30 mm, in terms of the deflection capacity.

In general, use of micro fiber appears to be better at increasing the deflection capacity. It was also noted that the deflection capacity improved as the fiber length in the hybrid specimens increases. This result was also well-supported by the experimental study of Ye et al. [35].

When the ultimate deflection of $L/150$ was reached, an evident amount of strength loss could be seen on the load-deflection curve. Here, the strength loss can be expressed using the term residual load ratio. A high level of this ratio denotes small amount of strength loss for the related specimen. It also means there is a substantial capacity beyond the deflection of $L/150$. The residual load behavior of specimens having different steel fiber contents are discussed as follows:

- While the best performance in terms of the residual capacity was achieved for the 60 mm macro fiber with 2.0%, the specimens containing the 13 mm micro fiber showed more stable behavior after the peak load for all volume fractions. At the same time, the lowermost performance was obtained for the specimens containing the 60 mm macro fiber of 1.0% by volume.
- The hybrid fiber specimens having 60 mm macro fiber demonstrated much better performance than the specimens with 30 mm. However, while the hybrid fiber specimens containing 60 mm macro fiber showed better performance than that of the mono form of 60 mm fibers of 1.5% by volume, they didn't show this improvement for the volume fraction of 2.0%.

4. CONCLUSIONS

In the presented research paper, the flexural behavior of Ultra-High Performance Fiber Reinforced Concrete (UHPFRC) with hybrid steel fibers was investigated experimentally. Prismatic beam specimens containing mono and hybrid steel fibers were produced and tested under four-point loading in accordance with the ASTM standard C 1609. The parameters, which directly define the flexural behavior, were compared and the performances of different fiber contents were discussed. In addition, the effects of fiber content on the compressive strength and elastic modulus were evaluated. The test results with respect to the UHPFRC specimens are summarized follow:

- Regardless of mono or hybrid form, the compressive strengths of all UHPFRC specimens are much greater than that of the non-fiber specimen. It was noted that use of micro fiber is more impactful than macro fibers in relation to compressive strength. The test results also indicate that the use of different fiber types has no specific effect on the elastic modulus.
- The first cracking loads of the specimens with micro fiber were obtained as higher values in the mono fiber specimens. However, the cracking response of hybrid specimens could differ depending on the fiber contents of micro and macro fibers.

- The best flexural performance among the test specimens was obtained for the hybrid specimens having a steel fiber of 2.0% by volume. The use of hybrid fiber in the mixture significantly improved the flexural performance of UHPFRC matrix relative to use of macro fiber. This is because the macro fibers can enhance the post-peak behavior and ductility while micro fibers improve the flexural strength and stiffness of concrete. It is important to note that the hybrid specimens including longer macro fibers showed better flexural performance. Therefore, the macro fiber of 60 mm provided better performance compared to that of the 30 mm.
- Regardless of the fiber amount, use of micro fiber exhibited a more stable behavior after the peak load. The best performance in terms of the residual load capacity was achieved for the macro fiber of 60 mm with 2.0% by volume in mono form. It should be noted that the hybrid specimens having the 60 mm macro fiber showed much better performance than the hybrid specimens with 30 mm macro fiber.
- As a result of the use of raw materials such as *SF* and *GGBS*, it is possible to produce UHPFRC with relatively low cement content and without the need of either special treatments or mixers. The experimental outcomes indicate that the fiber content had a significant effect on the flow ability of UHPFRC. As the fiber amount increases, the spread values decrease for all fiber types. As a result of the multiple fiber use in the mixture, the viscosity of concrete is higher than compared to fiber use in mono form. It can be deduced from the test results that the produced UHPFRC matrix is highly workable and suitable for cast in place reinforced concrete members.

Acknowledgements

The authors thank to the BEKSA-DRAMIX and the BASF companies due to their contributions in supplying materials to the study.

Symbols

b : *Width of specimen*

CoV : *Coefficient of variation*

d : *Depth of specimen*

f : *Strength*

f_P : *Flexural strength*

L : *Span length*

P : *Load*

P_p : *The peak load*

P_1 : *The first-peak load* (*cracking load*)

P^D_{150} : *The residual load at net deflection of L/150*

Std *: Standard deviation*

T *: Toughness*

t_{500} *: Measure time to the first touches 500 mm diameter mark*

V_f *: Fiber volume fraction*

δ_1 *: Net deflection at the first-peak load*

δ_P *: Net deflection at the peak load*

μ *: Mean*

References

[1] Brandt, A. M., Fibre Reinforced Cement-Based (FRC) Composites after Over 40 Years of Development in Building and Civil Engineering. Composite Structures, 86 1–3, 3-9, 2008.

[2] Banthia, N., Nandakumar, N., Crack Growth Resistance Hybrid Fiber Reinforced Cement Composites. Cement & Concrete Composites, 25, 1, 3-9, 2003.

[3] Won, J. P., Hong, B. T., Choi, T. J., Lee, S. J., Kang, J. W., Flexural Behaviour of Amorphous Micro-Steel Fibre-Reinforced Cement Composites. Composite Structures, 94, 4, 1443-1449, 2012.

[4] Wille, K., Naaman, A. E., El-Tawil, S., Parra-Montesinos, G. J., Ultra-High Performance Concrete and Fiber Reinforced Concrete: Achieving Strength and Ductility without Heat Curing. Materials and Structures, 45, 3, 309-324, 2012.

[5] Kim, D. J., Park, S. H., Ryu, G. S., Koh, K. T., Comparative Flexural Behavior of Hybrid Ultra High Performance Fiber Reinforced Concrete with Different Macro Fibers. Construction and Building Materials, 25, 11, 4144-4155, 2011.

[6] Yazıcı, H., The Effect of Curing Conditions on Compressive Strength of Ultra High Strength Concrete with High Volume Mineral Admixtures. Building and Environment, 42, 5, 2083-2089, 2007.

[7] Yazıcı, H., Yiğiter, H., Karabulut, A. Ş., Baradan, B., Utilization of Fly Ash and Ground Granulated Blast Furnace Slag as an Alternative Silica Source in Reactive Powder Concrete. Fuel, 87, 12, 2401-2407, 2008.

[8] Yazıcı, H., Yardımcı, M. Y., Aydın, S., Karabulut, A. S., Mechanical Properties of Reactive Powder Concrete Containing Mineral Admixtures under Different Curing Regimes. Construction and Building Materials, 23, 3, 1223-1231, 2009.

[9] Yazıcı, H., Yardımcı, M. Y., Yiğiter, H., Aydın, S., Türkel, S., Mechanical Properties of Reactive Powder Concrete Containing High Volumes of Ground Granulated Blast Furnace Slag. Cement and Concrete Composites, 32, 8, 639-648, 2010.

[10] Wang, C., Yang, C., Liu, F., Wan, C., Pu, X., Preparation of Ultra-High Performance Concrete with Common Technology and Materials. Cement and Concrete Composites, 34, 4, 538-544, 2012.

[11] Yang, S. L., Millard, S. G., Soutsos, M. N., Barnett, S. J., Le, T. T., Influence of Aggregate and Curing Regime on the Mechanical Properties of Ultra-High Performance Fibre Reinforced Concrete (UHPFRC). Construction and Building Materials, 23, 6, 2291-2298, 2009.

[12] Wille, K., Naaman, A. E., Parra-Montesinos, G. J., Ultra-High Performance Concrete with Compressive Strength Exceeding 150 MPa (22 ksi): A Simpler Way. ACI Materials Journal, 108, 1, 46-54, 2011.

[13] Fehling. E., Schmidt, M., Walraven, J., Leutbecher, T., Frönlich, S., Ultra-High Performance Concrete UHPC: Fundamentals, Design, Examples, Beton-Kalender. Wilhelm Ernst & Sohn, 2014.

[14] AFGC: Recommendation: Ultra High Performance Fibre-Reinforced Concretes, Revised ed. Association Française de Génie Civil, Service D'études Techniques Des Routes et Autoroutes, 2013.

[15] JSCE: Recommendations for Design and Construction of High Performance Fiber Reinforced Cement Composites with Multiple Fine Cracks (HPFRCC), Concrete Engineering Series 82, Japan Society of Civil Engineers, 2008.

[16] JSCE: Recommendations for Design and Construction of Ultra-High Strength Fiber Reinforced Concrete Structures (Draft), JSCE Guidelines for Concrete No. 9, Japan Society of Civil Engineers, 2006.

[17] Russell, H. G., Graybeal, B. A., Ultra-High Performance Concrete: A State-of-the-Art Report for the Bridge Community, FHWA-HRT-13-060, U.S. Department of Transportation, 2013.

[18] Wille. K., Kim, D. J., Naaman, A. E., Strain-Hardening UHP-FRC with Low Fiber Contents. Materials and Structures, 44, 3, 583-598, 2011.

[19] Banthia, N., Sappakittipakorn, M., Toughness Enhancement in Steel Fiber Reinforced Concrete through Fiber Hybridization. Cement and Concrete Research, 37, 9, 1366-1372, 2007.

[20] Rossi, P., Antonio, A., Parant, E., Fakhri, P., Bending and Compressive Behaviors of a New Cement Composite. Cement and Concrete Research, 35, 1, 27-33, 2005.

[21] Rossi, P., High Performance Multimodal Fibre Reinforced Cement Composite (HPMFRCC): The LCPC Experience. ACI Materials Journal, 94, 6, 478-483, 1997.

[22] Rambo, D. A. S., Silva, F. D. A., Filho, R. D. T., Mechanical Behavior of Hybrid Steel-Fiber Self-Consolidating Concrete: Materials and Structural Aspects. Materials and Design, 54, 2-42, 2014.

[23] Sorelli, L. G., Meda, A., Plizzari, G. A., Bending and Uniaxial Tensile Tests on Concrete Reinforced with Hybrid Steel Fibers. Journal of Material in Civil Engineering, 17, 5, 519-527, 2005.

[24] Sahmaran, M., Yaman, I. O., Hybrid Fiber Reinforced Self-Compacting Concrete with a High-Volume Coarse Fly Ash. Construction and Building Materials, 21, 1, 150-156, 2007.

[25] Akcay, B., Tasdemir, M. A., Mechanical Behaviour and Fibre Dispersion of Hybrid Steel Fibre Reinforced Self-Compacting Concrete. Construction and Building Materials, 28, 1, 287-293, 2012.

[26] Banthia, N., Gupta, R., Hybrid Fiber Reinforced Concrete (HyFRC): Fiber Synergy. Materials and Structures, 37, 10, 707-716, 2004.

[27] Nehdi, M., Ladanchuk, J. D., Fiber Synergy in Fiber-Reinforced Self-Consolidating Concrete. ACI Materials Journal, 101, 6, 508-517, 2004.

[28] Chen, Y., Qiao, P., Crack Growth Resistance of Hybrid Fiber-Reinforced Cement Matrix Composites, Journal of Aerospace Engineering. Special Issue: Mechanics of Advanced Materials and Structures, 24, 2, 154-161, 2011.

[29] Ahmed, S. F. U., Maalej, M., Paramasivam, P., Flexural Responses of Hybrid Steel-Polyethylene Fiber Reinforced Cement Composites Containing High Volume Fly Ash. Construction and Building Materials, 21, 5, 1088-1097, 2007.

[30] Yao, W., Li, J., Wu, K., Mechanical Properties of Hybrid Fiber-Reinforced Concrete at Low Fiber Volume Fraction. Cement and Concrete Research, 33, 1, 27-30, 2003.

[31] Sivakumar, A., Santhanam, M., Mechanical Properties of High Strength Concrete Reinforced with Metallic and Non-Metallic Fibres. Cement and Concrete Composites, 29, 8, 603-608, 2007.

[32] Dawood, E. T., Ramli, M., Mechanical Properties of High Strength Flowing Concrete with Hybrid Fibers. Construction and Building Materials, 28, 1, 193-200, 2012.

[33] ASTM C 1609 / C 1609M-05: Structural Test Method for Flexural Performance of Fiber Reinforced Concrete (Using Beam with Third Point Loading), ASTM International, West Conshohocken, PA, 2006.

[34] Birol, T., Investigation of Flexural Behavior of Reinforced Concrete Beams with Ultra High Performance Fiber Reinforced Concrete, PhD Thesis (in Turkish), Balikesir University, Turkey, 2016.

[35] Ye, Y., Hu, S., Daio, B., Yang, S., Liu, Z., Mechanical Behavior of Ultra-High Performance Concrete Reinforced with Hybrid Different Shapes of Steel Fiber, 12th COTA International Conference of Transportation Professionals: Multimodal Transportation Systems - Convenient, Safe, Cost-Effective, Efficient, CICTP 2012, American Society of Civil Engineering, Pages 3017-3028, Beijing, China, 2012.

Teknik Dergi, 2020 10399-10411, Paper 596

Evaluation of the Effect of Glass Granule Size on Water Damage Performance of Asphalt Mixtures

Erol İSKENDER[1]
Aytuna SAYIN[2]
Atakan AKSOY[3]
Cansu İSKENDER[4]

ABSTRACT

Economic growth and the increase in the population trigger consumption and increase the amount of waste produced. One of the resulting wastes is glass and using of these large amount of glass waste materials by environmental methods is seen as an important issue. On the other hand, there are difficulties due to the decrease of natural resources in the supply of aggregates used in asphalt pavements. In this study, the use of waste glass instead of natural aggregates in asphalt pavements was investigated in terms of water damage. In addition to base bitumen, hydrated lime modified and SBS modified bitumen were used in experimental studies. The waste glass was added in two different sizes (as filler materials and 2 mm sized fine aggregate) and three addition ratios (20%, 30% and 40%) instead of basalt aggregates. The asphalt mix samples produced in optimum bitumen contents were evaluated for water damage by AASHTO T 283 method. Asphalt mixture with 20% glass filler showed the highest water damage resistance. Among the options where the glass aggregate size was chosen as 2 mm, the highest water damage resistance was realized at addition rate of 30%. Both hydrated lime and SBS polymer were effective in improving water damage resistance. However, the highest tensile strength ratio was obtained with hydrated lime. The optimum bitumen contents of the mixtures with glass aggregates produced with both base and modified bitumen were decreased compared to that produced entirely with basalt aggregate. According to the test results, it is understood that the filler materials produced from waste glasses can be used instead of natural aggregate filler.

Keywords: Waste glass, glass granule asphalt pavements, water damage, indirect tensile strength ratios, SBS polymer, hydrated lime.

Note:

- This paper has been received on January 2, 2019 and accepted for publication by the Editorial Board on May 30, 2019.
- Discussions on this paper will be accepted by January 31, 2021.

- https://dx.doi.org/10.18400/tekderg.504698

1 Karadeniz Technical University, Civil Engineering Department, Trabzon, Turkey - eiskender@ktu.edu.tr https://orcid.org/0000-0001-7934-839X

2 General Directorate of Highways, Tenth Regional Directorate, Trabzon, Turkey - asayin22@hotmail.com https://orcid.org/0000-0002-2442-5324

3 Karadeniz Technical University, Civil Engineering Department, Trabzon, Turkey - aaksoy@ktu.edu.tr https://orcid.org/0000-0001-5232-6465

4 Karadeniz Technical University, Civil Engineering Dep., Trabzon, Turkey - cansuiskender3@gmail.com https://orcid.org/0000-0003-2856-4409

1. INTRODUCTION

Since aggregate constitutes a large portion of the asphalt mix, comprehensive understanding of the engineering properties of recycled aggregate can provide tremendous benefits in terms of environmental protection and efficient use of resources. Recognizing this fact, considering the recovered aggregate or mixture, such as reclaimed asphalt pavement (RAP), recycled construction aggregate (RCA), recycled glass, etc., the reported work and research on their use have increased throughout the world in the last two decades [1].

Large quantities of waste are produced with rapid economic growth and ever-increasing consumption. Among these is the waste glass material being an important part. The glass material is non-metallic and inorganic, neither burnable nor decomposable, which can be difficult to recover. The performance of the asphalt concrete in which a part of the crushed fine aggregate is replaced by the crushed glass material has been examined. Glass materials are fragile and silicon rich, therefore the basic technical indices of glass-asphalt concrete are the resistance to water and strength [2].

Glassphalt is basically the same as conventional hot mix asphalt but it contains grounded crushed glass instead of stone aggregate (basalt, limestone, etc.). Glass aggregate of 3/8-inch and finer grade is recommended for the surface layer [3].

The amount and size of the added glass cullet in the aggregate mixture affects the mechanical properties of the asphalt mixture. Increasing the amount of glass cullet reduces permanent deformation of asphalt samples. For upper layer, behavior of glassphalt may be satisfactory for quantity of glass up to 15% [2]. Adding broken glass particles up to 15% to the aggregate mixture improves the fatigue behavior of the asphalt mixture and increases the stiffness modulus. But when the glass aggregate ratio exceeds 15%, reduction occurs [4, 5]. Skid resistance, resilient modulus and moisture sensitivity of asphalt mixture containing crushed glass aggregate were evaluated. The fine aggregates, up to 15% of the total aggregate content, were replaced with glass particles in three different gradations. It was found that the crushed glass particles improved skid resistance by up to 20% [6].

The size of the glass aggregate also affects the performance of the asphalt mixture. The maximum size of the glass aggregate is generally recommended as 4.75 mm [4, 5, 7-10]. Some researchers suggest that 2.36 mm maximum glass aggregate size and 10% utilization rate are more appropriate [11].

In a study on the dynamic characteristics of glassphalts, four percent of hydrated lime was used as antistripping agent. Stiffness modulus of glassphalt mixtures increased with respect to conventional asphalt-mix. In addition, 3–5% hydrated lime was used as an anti-stripping agent and it was found that a glassphalt mixture containing hydrated lime has a greater stiffness modulus than normal specimens [12]. In another study, the effect of hydrated lime on the rutting, water damage and stability properties of the glassphalt mixtures was investigated. Hydrated lime was added to both bitumen and aggregate mixture. Glassphalt mixture with hydrated lime showed higher water damage and rutting resistance. Moreover, the stability values of the samples increased [13].

In a study in the literature, among the materials used in the tests, heavy duty bitumen (AH-70) and SBS modified asphalt, limestone aggregate and crushed recycled glasses were used. The Marshall test was used to investigate the effect of the optimum asphalt content, volume

properties and asphalt concrete strength when several different types of crushed glass were added. The test data obtained from the Modified Lottman test, the freeze-thawing test and the submerged wheel tracking test show that glass-asphalt concrete is more resistant to water damage than normal asphalt concrete. Properties can be improved by using liquid anti-stripping agents or hydrated lime additive. The high temperature stability and fatigue performance of the glass-asphalt concrete were also tested and the results were satisfactory. The research has shown that it is possible to recycle and use waste glass in asphalt concrete. The satisfactory performance of the upper asphalt coating layers can be achieved with a dosage of 10-15% by weight. Larger quantities can induce stripping problems and make the upholstery susceptible to water damage. 25% or more of the glass contribution can only be applied to the middle or lower layer [2].

In the literature, it is recommended that the maximum glass aggregate size should be chosen as 4.75 mm and the use of larger glass particle sizes should be avoided. The results of water immersed rutting tests show that the dynamic stability of samples with a maximum glass particle size of 9.5 mm is lower than that of samples with a maximum size of 4.75 mm. Also, there is not much more surface area in the 9.5 mm blend. For this reason, the maximum size of 9.5 mm is not suitable for use in asphalt mixtures and the work adopts a maximum size of 4.75 mm [14].

The use of primary aggregate in a road asphalt mixture layer or aggregate asphalt mixture is seen as a waste of a limited natural resource. Recycled glass can be considered as valuable alternative aggregate resources for asphalt mixture production. The purpose of this work is to evaluate the use of waste glass in asphalt mixtures as secondary aggregates according to Marshall Specifications. The study is based on the combination of glass with six dimensions (1/2, 3/8, No. 4, No. 8, No. 50 and No. 200) and two contents (50% and 100%) according to the weight of each piece. Secondly, it is used as additive materials containing three times (1, 2 and 4%) total mixture weight of glass and two dimensions of glass (No. 50 and No. 200). The engineering properties of the control and glass mixtures (stability, flow, volume density and percentage of voids in the total mixture) were evaluated by the Marshall Test. The study results show that Marshall Stability for glass fiber is higher than the control mixture when glass gradation (No. 8 and No. 200) are used as secondary aggregates in the asphalt mix, respectively [15].

Through effective marketing trials, the material is generally sold between U.S. $1.00 to $2.00 per ton for glass waste versus $5.00 to $7.00 per ton for conventional control aggregate. The most successful and predominant use is in the manufacture of asphalt, commonly referred to as “glassphalt”. Based on the customer, asphalt plants throughout the Northeast and other areas of the USA routinely blend the natural aggregate with up to 10% processed glass for making asphalt mixtures. The amount of glass is limited to 10% in order to avoid water damage (i.e. the separation of the glass component from the binders). This application also requires the proper sizing of the glass aggregate, but most importantly, the quantities of glass aggregate required for asphalt producers to continually incorporate the material into their product are often prohibitive [16].

Glass recycling rate in Turkey compared with Western European countries is still quite low. Glass unlike all other materials can be converted endlessly and does not affect the recycling process. The quality of the final product is not affected in a negative way. Glass waste, especially glass packaging, is recycled and recycled into glass as raw material, contributing

not only to the economy but also to the environment as it reduces energy use and greenhouse gas emissions significantly. The volume of recycled glass reached 141 thousand tons in 2015 from 67 thousand tons per annum [17]. Glass packaging recycling rates of European countries are quite high. 94.18% in Switzerland, 93.76% in Luxemburg, and 92.94% in Sweden, giving the highest return-on-rates. The average of EU-27 countries reaches to 70.28% value and unfortunately Turkey is one of the countries located at the bottom of the list with 25.81% with low performance [18].

The aim of this research is to investigate the performance of glass admixtures of different sizes in asphalt mixtures using basalt aggregates. Glass was used at different additive ratios. The glass admixture in different proportions was used with different sizes, hydrated lime and SBS polymer options. For selected multi-additive alternatives, the possibility of using recycled glass as aggregate is examined. Combined performances were questioned, especially in terms of water damage, under specified parameters.

2. MATERIALS AND METHOD

2.1. Materials

Aggregates were obtained by crushing rocks supplied from the basalt quarry in Trabzon (in Turkey). The general physical properties of basalt aggregates were presented in Table 1.

Table 1 - Engineering properties of basalt aggregates

Properties	Test Method	Value
Specific gravity (coarse agg.)	ASTM C 127	
Bulk		2.684
Apparent		2.744
Specific gravity (fine agg.)	ASTM C 128	
Bulk		2.656
Apparent		2.754
Specific gravity (filler)		2.821
Los Angeles abrasion (%)	ASTM C-131	12
Flakiness (%)	BS 812 (Part 105)	14
Stripping resistance (no additive) (%)	ASTM D-1664	35-40
Water absorption (%)	ASTM C-127	0.81
Soundness in $NaSO_4$ (%)	ASTM C-88	0.92
Plasticity index for sandy aggregate	TS 1900	non- plastic

In the study, 50/70 penetration grade bitumen obtained from Tüpraş Kırıkkale refinery was used. Some properties of used bitumen were given in Table 2.

Table 2 - Properties of used base bitumen

Test	Test Method	Value
Specific gravity (25°C)	ASTM D-70	1.025
Softening point (°C)	TS EN 1427	50
Flash point (Cleveland)	TS EN ISO 2592	240
Penetration (25°C)	TS EN 1426	63
Ductility (25°C)	ASTM D-113	100+

Dense graded aggregate combination (Type-1) was used in accordance with the Turkish Highways Technical Specification [19]. The maximum aggregate size was selected as 19 mm. Aggregate gradation was given in Figure 1.

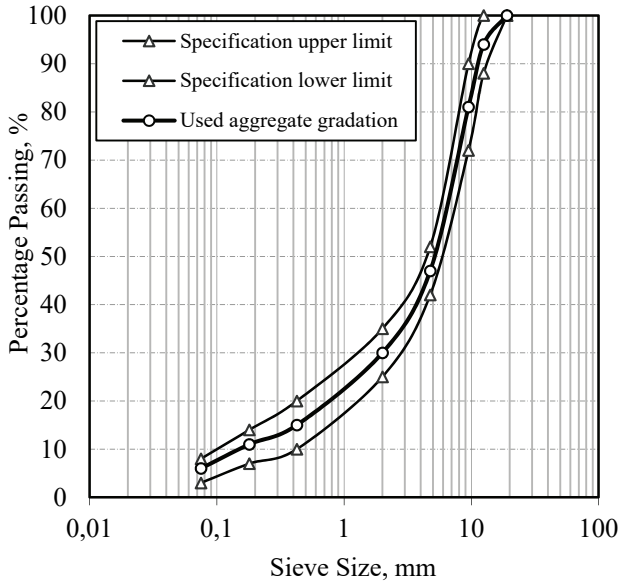

Figure 1 - Selected dense aggregate gradation chart

In the work, waste glass, which is the production residue of glass processing factories, is used as aggregate substituted for basalt aggregates. The waste glasses are in colorless form and consists of a mixture of tempered and construction glasses. The glasses were sieved from standard ASTM sieves after crushed in a mini crusher in the laboratory. Two different sized glass aggregate were used substituted for basalt aggregate. Glass aggregates, at sizes less than 0.075 mm (filler size) and between 2 mm and 0.425 mm, were used at 20%, 30% and 40% instead of basalt aggregate. Main oxide analysis of glass aggregates was done and results are shown in Table 3.

Table 3 - Chemical analysis test results of waste glasses particles [20]

Components	Formula	Value (%)
Silicium dioxide	SiO_2	70.4
Aluminum oxide	Al_2O_3	0.11
Titanium dioxide	TiO_2	0.086
Ferrous oxide	Fe_2O_3	0.205
Magnesium oxide	MgO	5.03
Calcium oxide	CaO	7.01
Sodium oxide	Na_2O	12.95
Potassium oxide	K_2O	0.51
Sulfur trioxide	SO_3	0.23

In addition to base bitumen, SBS (Kraton D1101) and hydrated lime (SKK 80-T) modified bitumen were also used. Chemical properties of hydrated lime illustrated in Table 4. Hydrated lime (HL) and SBS addition ratios in bitumen were selected as 2% and 5%, respectively. Modified bitumen were prepared with high shear mixer. The modification was carried out at a temperature of 160°C for 30 minutes at a stirring speed of 4500 rpm.

Table 4 - Chemical properties of used hydrated lime [20].

Chemical properties	Test standard	Value
Total CaO (%)	EN 459-2	84.66
Active $Ca(OH)_2$ (%)	TS 32	82.23
MgO (%)	EN 459-2	4.05
Total CaO+MgO (%)	TS	89.17
Ignition loss (%)	EN 459	23.17
Acid-insoluble (%)	TS 32	1.39
R_2O_3 (%)	TS 32	0.44
SO_3 (%)	EN 459	1.51
CO_2 (%)	EN 459	3.77
Density (kg/m^3)	EN 459	473

2.2. Mixture Design and Sample Production

Dense graded asphalt concrete design was done with the Marshall Design method (ASTM D 1559). Optimum bitumen contents for conventional and modified bitumen were determined separately. The optimum bitumen content was taken as the percentage of bitumen corresponding to 4% air voids and designated as 5.30%, 5.63% and 5.42% for base bitumen,

hydrate lime modified bitumen and SBS modified bitumen, respectively. According to bitumen - glass aggregate ratio combinations optimum bitumen ratios were determined and illustrated in Table 5.

Table 5 - Optimum bitumen contents of asphalt mixtures with glass aggregates

	Basalt aggregate	Glass filler substituted for basalt filler			Glass aggregate (0.475-2.0 mm) substitute for basalt		
	100%	20%	30%	40%	20%	30%	40%
Control bitumen	5.30	5.21	5.15	5.14	5.24	5.19	5.17
HL modified bitumen	5.63	5.51	5.48	5.44	5.56	5.51	5.50
SBS modified bitumen	5.42	5.35	5.29	5.27	5.37	5.33	5.30

2.3. Method

The glass admixtures were added to the aggregate mix substituted for the basalt aggregate of its size. Glass wastes were broken and used in place of fillers and basalt aggregates in the range of 0.425 -2.0 mm. Dense graded asphalt concrete mixtures with base bitumen, hydrated lime modified bitumen and SBS modified bitumen were produced and the resistance to water damage was evaluated by AASHTO T283 method.

Samples used for the AASHTO T283 method are divided into two groups, unconditioned and conditioned. The samples in conditioned group are saturated with water between 70% and 80% with a vacuum pycnometer. Samples that reach more saturation are deemed deformed and are not used in subsequent tests. The samples are then tightly covered with a plastic film and placed in a plastic bag containing 10±5 ml of water. Saturated samples are kept frozen at -18±3°C for minimum 16 hours. The samples, which have completed the freezing process, are placed in a water bath at 60±1°C for 24±? hours without waiting. After water bath, plastic bag and film are removed. Conditioned samples are placed in a water bath at 25±0.5°C for 2h±10 min. Samples removed from the water bath are tested by indirect tensile strength method. Samples in unconditioned group are tested after the water bath at 25±0.5°C for 2h±10 min directly. During the test, the maximum compressive strength is recorded in the test device. Using the recorded values and sample sizes, the tensile strengths are calculated by Equation 1 [21].

$$S_t = (2000 \cdot P)/(\pi \cdot t \cdot D) \quad (1)$$

Where:

S_t: tensile strength, kPa

P: maximum load, N

t: specimen thickness, mm

D: specimen diameter, mm

In order to quantify the loss of strength due to water and freeze-thaw, the averages of the indirect tensile strengths of the samples in each group are taken and proportioned as shown in Equation 2.

$$ITSR = S_2/S_1 \quad (2)$$

Where:

ITSR: indirect tensile strength ratio

S_1: average tensile strength ratio of the unconditioned subset, kPa

S_2: average tensile strength ratio of the conditioned subset, kPa

The ITSR value and the resistance of the mixture to water damage are directly proportional. Usually 0.80 is considered the limit value. Asphalt mixtures with ITSR value lower than 0.80 are considered to be unresistant to water damage while higher ones are considered to be resistant [22].

3. TEST RESULTS AND EVALUATIONS

Indirect tensile strength tests were performed on Marshall samples produced with base and modified bitumen according to AASHTO T283 method. Indirect tensile strength (ITS) values obtained from the tests and the calculated indirect tensile strength ratio (ITSR) values of mixtures are illustrated in Figure 2 to Figure 5.

Particular attention was paid to the subject of identity in the production of all asphalt mixture briquettes with and without glass additive. For this purpose, samples with a difference between their practical densities greater than 20‰ were not used and new samples were produced. The briquettes produced with the same mixtures type gave consistent indirect tensile strength values among themselves.

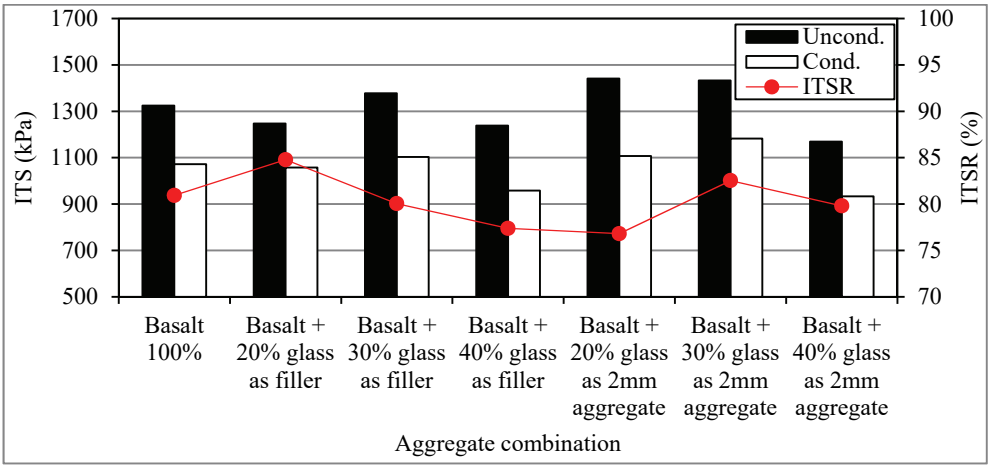

Figure 2 - Average ITS and ITSR values of control mixtures

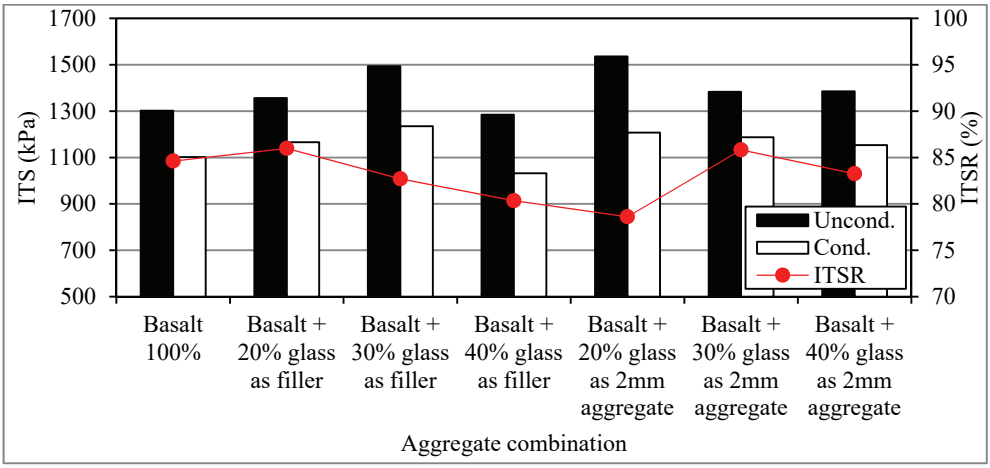

Figure 3 - Average ITS and ITSR values of SBS modified mixtures

Crushed glass particles were used as aggregate substituted for both filler and 2 mm fine aggregate in asphalt mixture. In addition, hydrated lime (HL) and SBS additives were chosen as additional performance enhancers. In the control mixtures (without HL and SBS), it is seen from Figure 2 that there is a decrease in tensile strength values in all mixtures with glass particles added 40%. However, with the reduction of glass aggregate ratio (except for 20% glass filler) ITS values of unconditioned samples have increased. In SBS- and HL-modified mixtures (Figure 3 and Figure 4), only 40% glass filler substitutes gave lower tensile strength values than those without any glass aggregates. In all other options, higher indirect tensile strengths were obtained. ITS values of the conditioned samples decreased significantly.

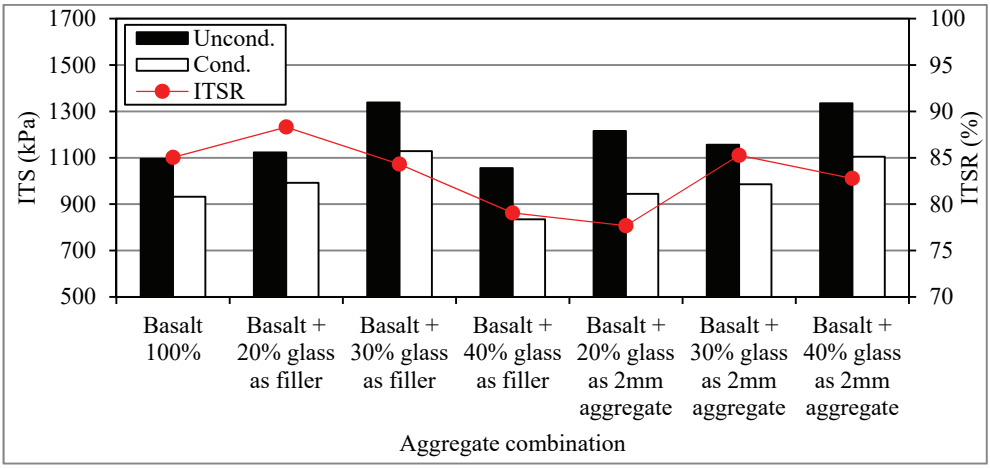

Figure 4 - Average ITS and ITSR values of HL modified mixtures

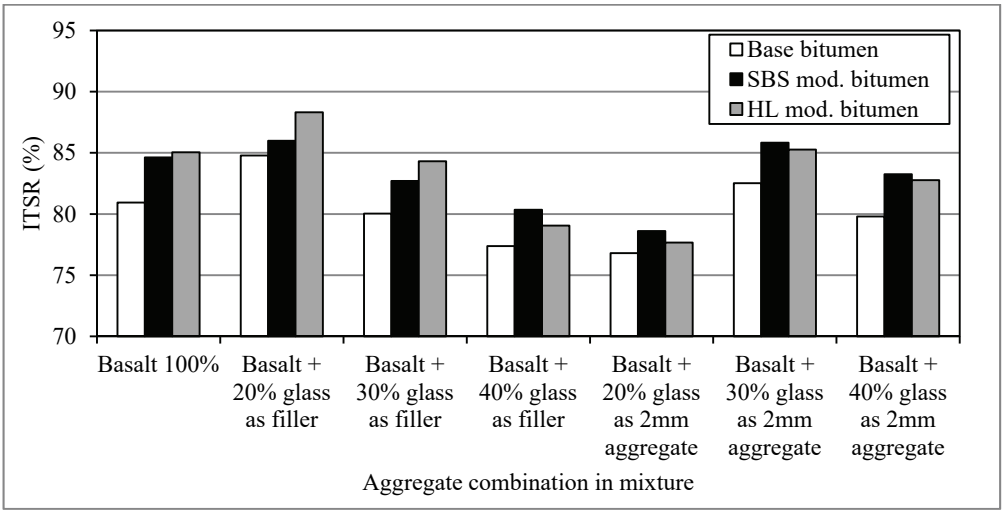

Figure 5 - Relationship between crushed glass size - ratio and water damage

As shown in Figure 5, indirect tensile strength ratios (ITSR) of both control mixtures and mixtures including glass aggregates were increased by SBS and HL modification. When 20% glass filler were used instead of basalt filler, higher water resistance was obtained compared with the control mixture. When the ratio of glass filler in the aggregate increases, the resistance to water damage decreases. When 2 mm-sized glass aggregates are added, the best results are obtained with a participation rate of 30%.

Ongoing studies have demonstrated that optimum mixture performance can best be obtained when 10% to 15% crushed glass is used as a fine aggregate substitute in asphalt mixes for road pavements. The major concern is the lack of absorption of bitumen by glass and the hydrophilic surface properties of glass that contribute to the water damage of glassphalt pavements. There is a potential to substitute depleting natural aggregates with crushed glass in asphalt mixes. This is based on the finding that asphalt mixtures with crushed glass could outperform conventional dense-graded mixtures in terms of permanent deformation, and they have a comparable fatigue resistance at low strains. The higher stiffness behavior exhibited by the glass mix at 20°C and 40°C determines that this mix can provide better resistance to permanent deformation than most conventional medium continuously-graded asphalt mixes. It is important to state that these conclusions pertain only to the crushed glass evaluated in this study and the specified design aggregate grading used, and cannot be transferred to any other crushed glass from different sources. Yet, these conclusions are based only on the properties of the mixes as determined in the laboratory [23].

The use of glass tends to reduce the VMA and air voids in Marshall Specimens; therefore, optimum asphalt binder content will also be decreased. Neither resilient modulus nor indirect tensile strengths are adversely affected by the addition of glass up to 15 percent. Although both wet strength and retained tensile strength ratios were unaffected by the percentage of glass, some separation at the asphalt glass interface was observed. A maximum of 15 percent crushed recycled glass should be allowed (100 percent passing a 9.5 mm sieve and a

maximum of 6 percent passing a 75 μm sieve) in hot mix asphalt mixes. There is little monetary incentive to use recycled glass at the present time because the cost of glass varies considerably [24].

In this study, the effect of glass granule size on water damage (stripping) is evaluated in asphalt pavements. The glass granules were used in two different sizes (filler and 2 mm sizes) and three different contents (20%, 30%, 40%). The basalt aggregate was selected as coarse, fine and filler material. Both conventional control mixtures and SBS polymer and hydrated lime modified blends were tested with these alternatives. Indirect tensile strength test was applied to both dry briquettes and conditioned briquettes with the specified water damage conditioning system. In terms of water damage, the glass granule additive is in better interaction with the SBS polymer than the hydrated lime. For control mixtures, SBS polymer and hydrated lime likewise increase resistance to water damage. If glass granules are used as filler material, 20% ratio is a suitable choice because control and modified mixtures show higher resistance to water damage at this rate of use. In 20% glass filler granule, SBS and hydrated lime options, the resistance to water damage is synergistically increased compared with the control mixtures. The 2 mm glass granule size has negligible effects on all mixtures on water damage. In terms of water damage, if glass granules are used as fillers, both modified mixtures give higher water resistance. It is more reasonable to use filler size in blends of glass granules. The indirect tensile test shows the load-spreading capacity of the mixtures. When the conditional indirect tensile strength values are considered together with the interpretation of water damage, 20% of glass granule is considered suitable as filler. In this respect, it can be evaluated that waste glass can be used as a performance enhancer in asphalt mixtures. The mixture is judged to provide a higher homogeneity. When the filler material is lacking, this can be done with glass granules. Glass filler is also performs as anti-stripping agents. In addition, glass filler can be successfully used in blends of polymer and hydrated lime. Even if the aggregate is entirely selected as a basalt aggregate, the granular glass is tested to be successful in terms of water damage. Although basalt aggregates are generally prone to water damage (stripping), the glass granule has a performance enhancing effect. It is also contemplated that the use of lime at the point of manufacturing process of glass, this content has an anti-stripping additive effect at this point. In asphalt mixtures, the waste glass can be used at the point of recycling in terms of environmental sustainable approaches.

4. CONCLUSIONS

In this study asphalt mixtures using waste glass are examined in different gradations and SBS polymer and hydrated lime admixtures have also been tried. It is possible to reach the following results. In view of stripping, the glass granule additive is in better interaction with the SBS polymer than the hydrated lime. If glass granules are used as filler material, 20% ratio is a suitable choice. In 20% glass filler granule, SBS and hydrated lime options, the resistance to stripping is synergistically increased compared with conventional mixes. The 2 mm glass granule size has negligible effect on all mixtures against water damage. It is more reasonable to use filler size in blends of glass granules. Waste glass can be used as a performance enhancer in asphalt mixtures. According to these results, glass filler could be considered among anti-stripping agents in hot mix asphalt.

Symbols

AH-70 : Heavy duty bitumen

CR : Crumb rubber

HL : Hydrated lime

ITS : Indirect tensile strength

ITSR : Indirect tensile strength ratio

RAP : Reclaimed asphalt pavement

RCA : Recycled construction aggregate

SBS : Styrene-butadiene-styrene

VMA : Voids in the mineral aggregate

[1] Tahmoorian F., Samali B., Tam W.Y., Yeaman J., Evaluation of Mechanical Properties of Recycled Material for Utilization in Asphalt Mixtures, Applied Sciences, 7, 763, 2017.

[2] Wu S., Yang W., Xue Y., Preparation and Properties of Glass-asphalt Concrete, Key Laboratory for Silicate Materials Science and Engineering of Ministry of Education, Wuhan University of Technology, Wuhan 430070, P.R China, 2004.

[3] Clean Washington Center, CWC. Best practices in glass recycling, 2005.

[4] Shafabakhsh, G.H., Sajed, Y., 2014. Investigation of dynamic behavior of hot mix asphalt containing waste materials, case study: glass-cullet. Case Studies in Construction Materials 1, 96–103, 2014.

[5] Arabani, M., 2011. Effect of glass-cullet on the improvement of the dynamic behaviour of asphalt concrete. Construction and Building Materials, 25 (3), 1181-1185, 2011.

[6] Afkhamy Meybodi, P., Khani Sanij, H., Hosseini, S.H., Olazar, M., Effect of Crushed Glass on Skid Resistance, Moisture Sensitivity and Resilient Modulus of Hot Mix Asphalt Arabian Journal for Science and Engineering, 44(5), 4575–4585, 2019.

[7] Su, N. and Chen, J.S., Engineering Properties of Asphalt Concrete Made with Recycled Glass, Resources Conservation and Recycling, 35(101), 259-274, 2002.

[8] Huang, Y., Bird, R.N., Heidrich, O., A review of the use of recycled solid waste materials in asphalt pavements, Resources, Conservation and Recycling 52, 58–73, 2007.

[9] Behbahani, H., Ziari, H., Kamboozia, N., Khaki, A.M. ve Mirabdolazimi, S.M., Evaluation of Performance and Moisture Sensitivity of Glasphalt Mixtures Modified with Nanotechnology Zycosoil as an Anti-Stripping Additive, Construction and Building Materials, 78, 60-68, 2015.

[10] Issa, Y., Effect of Adding Crushed Glass to Asphalt Mix, Archives of Civil Engineering, 62, 2, 2016.

[11] Salem, Z.T.A., Khedawi, T.S., Baker, M. B., ve Abendeh, R., Effect of Waste Glass on Properties of Asphalt Concrete Mixtures, Jordan Journal of Civil Engineering, 11 (1), 117-131, 2017.

[12] Arabani, M., Mirabdolazimi, S. M. Evaluation of the effect of the use of waste glass cullet in increasing the lifetime of HMA. In: International congress on civil engineering, Iran, Shiraz University, 2009.

[13] Liao, Y., Wu, H., Yi, L. The enhancement effect of hydrated lime on glassphalt concrete. Applied Mechanics and Materials, 670-671, 423-427, 2014.

[14] Marti, M.M., Mielke, P.E.A., Synthesis of Asphalt Recycling in Minnesota, Minnesota Local Road Research Board, Synthesis Report 2002-32, 2002.

[15] Jasim, A.A., By Using Waste Glass as Secondary Aggregates in Asphalt Mixtures, International Journal of Advanced Research 2, 41-46, 2014.

[16] Meyer, C., Egosi, N., Andela, C., Concrete with Waste Glass as Aggregate, Recycling and Re-use of Glass Cullet", Dhir, Dyer and Limbachiya, editors, Proceedings of the International Symposium Concrete Technology Unit of ASCE and University of Dundee, March 19-20, 2001.

[17] A summary of the Sectorial Agenda, bi_ozet.com, (ŞİŞECAM) and (EBRD) will skip partnership with Turkey in glass recycling sector editorbiozet, June 28, 2016.

[18] Turkey Glass and Glass Products Industry Assembly Industry Report, Turkey Union of Chambers and Commodity Exchanges / www.tobb.org.tr, ISBN :978-605-137-299-02012, 2012.

[19] Turkish Highways Technical Specification, General Directorate of Turkish Highways, Technical Research Department, Ankara, Turkey, 2013.

[20] İskender, C., Effect of Glass Aggregate Size and Aggregate Gradation on Asphalt Pavement Performance, Master Thesis, Karadeniz Technical University, Institute of Natural Sciences, Trabzon, Turkey, 2017.

[21] Standard method of test for resistance of compacted asphalt mixtures to moisture-induced damage, AASHTOT283, American Association of State Highway and Transportation Officials, Washington, D.C., USA, 2014.

[22] Liang, R.Y., Resistance of Compacted Bituminous Mixture to Moisture Induced Damage for Superpave, Department of Civil Engineering, University of Akron, Akron, 2008.

[23] Anochie-Boateng, J.K, George, T.B., Exploring Waste Glass in Hot-Mix Asphalt, Roads & Bridges, IMIESA April, 31-34, 2017.

[24] Kandhal, P.S., Waste Materials in Hot Mix Asphalt - An Overview, National Center for Asphalt Technology, NCAT Report No. 92-6, December 1992.

Teknik Dergi, 2020 10413-10439, Paper 597

Experimental Investigation of Using Sandwich Panels as Infill Plate in a Steel Plate Shear Wall

Said DUSAK[1]
Cem YALÇIN[2]
Ahmet Necati YELGIN[3]

ABSTRACT

A total of five steel frame specimens, one bare and four infilled, were designed with thin-walled steel sheets and corrugated sandwich infill panels in order to increase their load and energy dissipation capacity. For this experimental study, single-story, single-bay steel frames of nominally-pinned beam-to-column connections were prepared with a scale ratio of 1:3. A quasi-static cyclic loading pattern was applied to the control bare and infilled steel frames, and their behavior was investigated both experimentally and analytically using SAP2000 and ABAQUS finite element software. First, five identical bare steel frame specimens were prepared and one of them was tested as a control specimen, and its rigidity and cyclic behavior was determined experimentally. Then, two sandwich panel specimens were prepared by connecting sandwich panels in the second and third bare steel frames using appropriate connections. The fourth specimen had only a single steel plate infill. Finally, the fifth specimen was prepared by removing the polyurethane material from inside the sandwich panel and only steel plates were attached to both faces of the frame. This way, it was possible to compare the effect of the polyurethane material inside the sandwich panel and the corrugated steel plate on the overall system behavior. In all specimens, the infill plates were fastened to the frame connection profiles using self-drilling screws and the responses of the specimens were compared in terms of their maximum load capacity, initial stiffness, ductility and energy dissipation capacity values under cyclic loading. The experimental and analytical investigations showed that, similarly to steel plate infills, the specimens with sandwich panels also behaved in a ductile manner with relatively lower load and energy dissipation capacities. Results of the strip model and the finite element model analyses were then compared with the experimental results and they were both found to be in good agreement.

Keywords: Steel plate shear wall, infill steel frame, sandwich panel, composite panel shear wall, cyclic loading, energy dissipation.

Note:
- This paper has been received on April 29, 2019 and accepted for publication by the Editorial Board on September 18, 2019.
- Discussions on this paper will be accepted by January 31, 2021.

• https://dx.doi.org/10.18400/tekderg.559036

1 Sakarya University, Institute of Natural Sciences, Sakarya, Turkey - sdusak@gmail.com - https://orcid.org/0000-0002-6903-1695

2 Bogazici University, Department of Civil Engineering, Istanbul, Turkey -yalcince@boun.edu.tr - https://orcid.org/0000-0003-3142-8125

3 Sakarya University, Department of Civil Engineering, Sakarya, Turkey - ayelgin@sakarya.edu.tr - https://orcid.org/0000-0002-1879-1459

1. INTRODUCTION

Steel plate shear walls have been the subject of many analytical and experimental studies over the past years [1-3], while many of these studies developed models with single infill plates [4, 5]. In order to increase the energy dissipation capacity of steel frames subjected to lateral loads, steel plate shear walls were constructed by attaching infill panels with different geometric and material properties inside the steel frame, directly or through the use of fish plates [6]. The first studies involved design of plates that were thick enough to withstand shear strength [7]. Later, studies were conducted with out-of-plane buckling of plates under lateral loadings in the form of tension strips to transfer the shear loads. Thus, thinner plates started to be used and they were allowed to buckle. A theoretical strip model was developed, defining the formation of tensile fields as plates buckle prior to yielding, while continuing to transfer lateral loads [8, 9]. Many studies have been conducted in the placement of thin vs. thick infill plates inside steel plate shear walls [10,11], the addition of stiffeners to the steel plate [12], the use of different types of frame connections [13,14], the differences in material characteristics and yield strengths [15], the introduction of perforations of different forms to certain areas on the plate so that it could absorb more energy [16], the use of corrugated steel infill plates [17], adding steel plate shear walls inside reinforced concrete and composite frames [18, 19], comparing behavior of braced frames and steel plate shear walls [20], and turning steel plates into composite panels with the addition of reinforced concrete partitions [21]. In addition, numerical and experimental studies have been conducted to rigid, semi-rigid and pinned beam-to-column connection designs [22, 23]. There have also been studies in which the infill plates were connected to the frame elements via beams and columns, or via beams only [24]. These studies demonstrated that different steel plate shear walls increased ductile behavior, energy dissipation capacity, maximum load capacity and the initial stiffness of steel plate shear walls. Berman and Bruneau [25] reported that the addition of steel plates to frames increased the energy dissipation capacity and ductility, and also provided additional shear strength.

2. OBJECTIVE AND RESEARCH RATIONALE

The present study aims to transform partition walls into steel plate shear walls without the need for an additional lateral load-resisting system. The objective is to propose an appropriate design to connect sandwich panel partition walls mounted in existing steel frames, thus providing a supplementary lateral load resisting system and strength to existing buildings. Single-story, single-bay specimens with dimensions having approximately a ratio of 1:3, when compared to a typical full-scale building frame, were prepared for the present study by connecting various types of infill panels to the frame's beams and columns, representing an intermediate floor of a multi-story building. In addition to the bare frame, three types of infill panels were designed with two sandwich panel specimens and one specimen with single plate of matching thickness, while the other one had steel plates on both sides of the sandwich panel without the polyurethane material. The behaviors of these specimens under cyclic loading were examined experimentally and analytically, and the results were compared in terms of initial stiffness, ductility and maximum load and energy dissipation capacity.

3. DESIGN OF SPECIMENS AND TEST SETUP

A single-story, single-bay, steel frame with a nominally-pinned beam-to-column connection, was used as a control bare frame (BF) specimen. The SP1 and SP2 specimens were prepared using sandwich panels as infill plates in the frame. The CLA specimen was prepared by removing the polyurethane material inside the sandwich panel. Finally, the TL specimen was prepared using a single steel plate with matching CLA's plate thickness. The steel frames of the control specimen BF and other specimens had the same characteristics such as dimensions, connection types, cross-sections and materials with the exception of the plates or panels placed inside the frame. Their physical and technical characteristics are presented in Table 1, where "*t*" represents the plate thickness. To investigate the effect of infill plates, cross-sections were selected so that the plasticization of frame elements before reaching yield values would be prevented. HEA 260 cross-sections were used for the frame columns and HEA 240 cross-sections for the beams. Specimens SP1, SP2, CLA and TL had similar frontal views, as shown in Figure 1, but had different cross-sections, as shown in Figure 2.

Table 1 - Specimen Properties

Specimen No.	Specimen Name	Panel/Plate Thickness	Infill Property
1	Bare Frame (BF)	–	–
2 and 5	Sandwich Panel (SP1/SP2)	*t*=100mm/ 0.5mm+0.5mm	0.5mm Steel Plate+ 99 mm Polyurethane+ 0.5mm Steel Plate
3	Two-Faced Discrete Steel Plate(CLA)	*t*=0.5mm+0.5mm	0.5mm Steel Plate + 99mm Gap + 0.5mm Steel Plate
4	Single Steel Plate (TL)	*t*=1.0mm	1.0mm Steel Plate

In order to minimize the contribution of the infill plates to the frame as much as possible, a nominally-pinned beam-to-column connection was designed. Since all frame specimens are identical, their rigidity would have equal contribution to all infilled specimens, Thus, the augmented capacities of infilled frames could easily be compared with each other, including the control bare frame specimen. Figure 3 provides details of the beam-to-column connections, where the beams are connected to the columns with six M16 bolts, via double angles from the beam web only. The maximum moment capacity of the joint region and the corresponding maximum shear stress acting on each bolt were calculated, and accordingly, six 10.9 class bolts were selected to join beam web to double angles. Especially, this type of connection having a relatively low moment capacity was selected to connect beam and column elements with these bolts in order to make sure that the beam-to-column connection acts as a nominally-pinned joint.

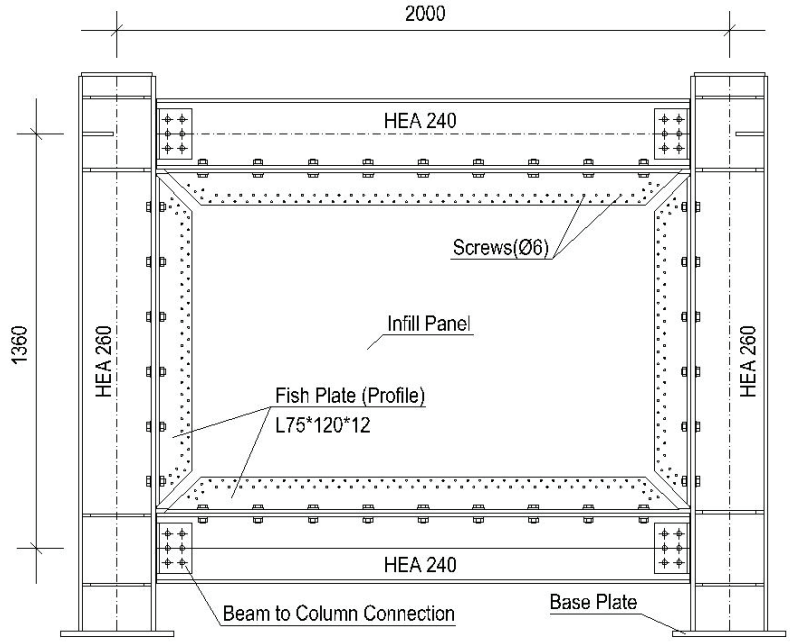

Figure 1 - Details of specimen SP1, SP2, CLA and TL (all dimensions are in mm)

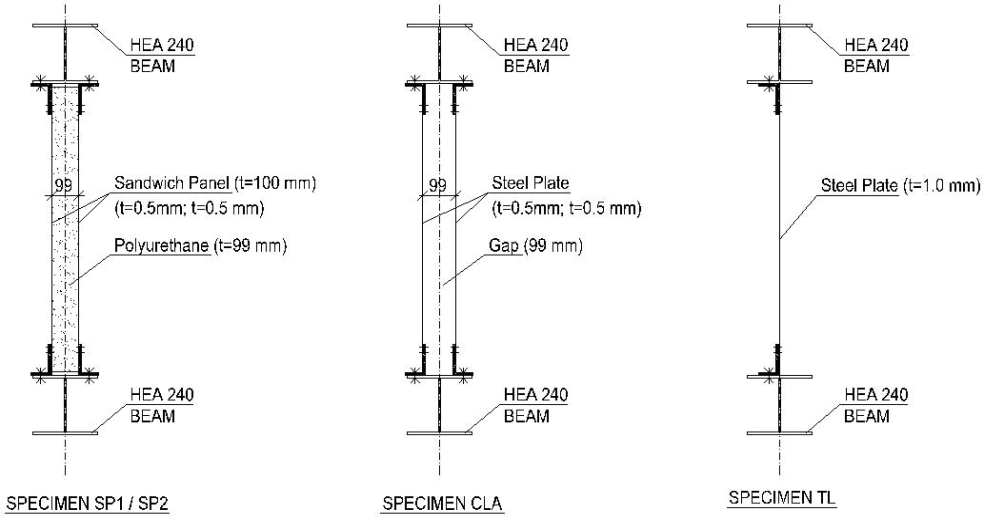

Figure 2 - Sections of infill panel/plate of each specimen

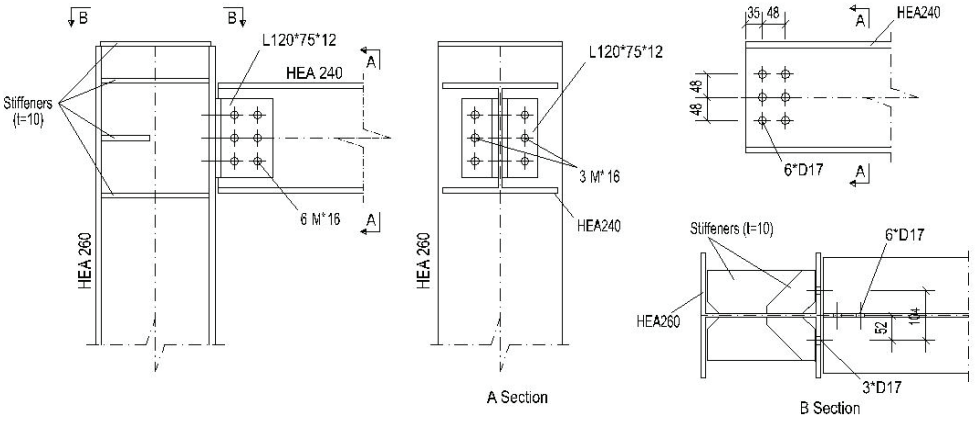

Figure 3 - Beam-to-column connection detail of frame (all dimensions are in mm)

The plates, on the other hand, were connected to the frame via a structural angle section attached to the frame, using self-drilling screws. In the literature, plates were usually connected via a fish plate welded to the frame, whereas in the present study, the connections were prepared with M16 bolts at 180mm center-to-center spacing along the short edge of the L120x75x12 structural steel angle. The connections were located along two lines for the two-face specimens of SP1, SP2 and CLA, and along a single line in the TL specimen, as shown in Figure 4. This connection type would allow easy replacement of plates when there is a need for change of any infill panel at extreme deformations via only the connection bolts. As welded connections may result in local heat-related deformations in thin plates, and because they do not require the preparation of holes prior to connection, the use of self-drilling screws was preferred. This fact was also mentioned by Vatansever and Yardimci [24] as an alternative method of connection. Also, an analytical model for screw connections is developed by Vatansever and Berman [26] as well. The aforementioned study reports that plate-to-frame connections made with self-drilling screws provided sufficient performance [23]. For that reason, 6-mm-diameter self-drilling screws having 310 MPa of yield capacity were preferred in this study. A total of 300 of these screws were used at two rows staggered with 40 mm centers in order to achieve a uniform load distribution, as shown in Figure 4. The infill plate connection design was carried out according to maximum expected tensile force acting on the strip model. Self-drilling screw diameter and its tensile capacity were calculated prior to the experiment.

Clevises were used to connect the test specimens to the plates, which in turn were fastened to the reinforced concrete foundation with anchors. The reinforced concrete foundation was fixed to the laboratory's strong floor with twelve 50-mm-diameter anchor bolts. The laboratory had a reaction wall with a capacity of 2000kN and an actuator with a capacity of 1000kN. The attachment holes in the reaction wall at 300mm centers played a key role in determining the size of the specimens. Figure 5 shows the experimental setup, while Figure 6 shows the steel plate shear wall specimens with sandwich panel and single steel plate.

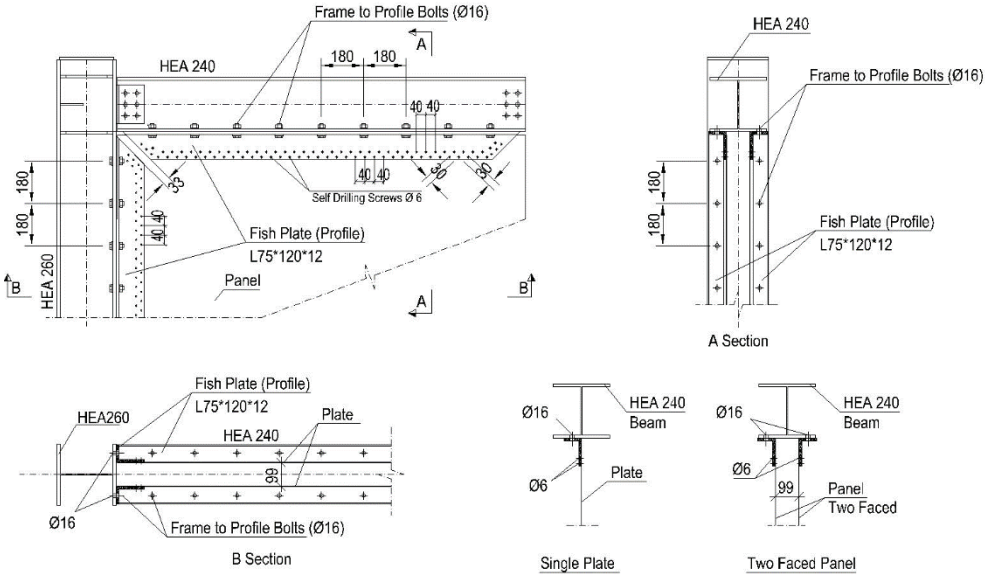

Figure 4 - Infill plate/panel to frame connection detail (all dimensions are in mm)

To prevent out-of-plane deformations during testing, four lateral bracings with steel rollers at the ends of the front and rear faces were used, aligned with the central axis of the upper beam. Friction was minimized by cleaning the rough surface of the beam, applying grease and attaching rollers to provide free movement along the direction of loading.

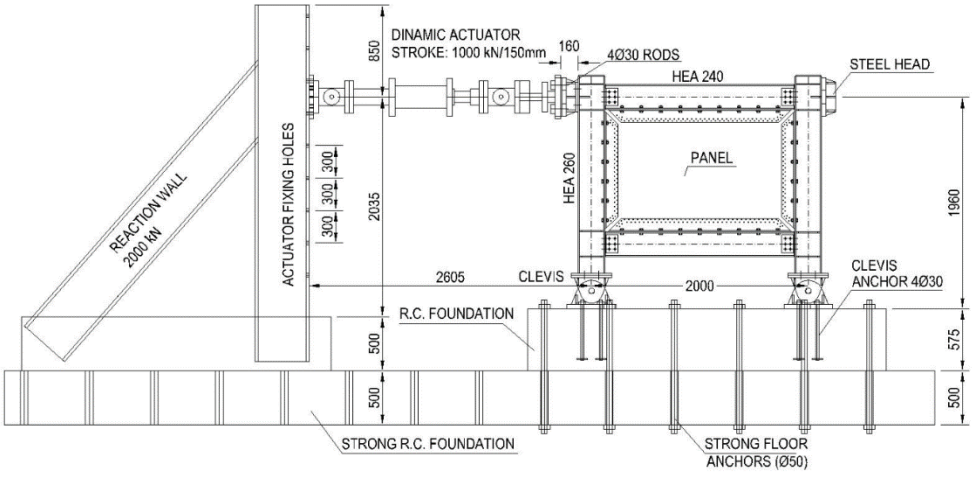

Figure 5 - Test Setup (all dimensions are in mm)

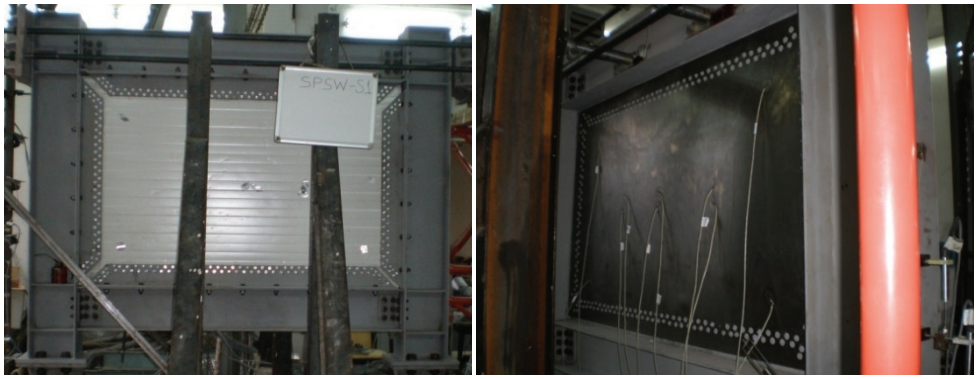

Figure 6 - Sandwich panel shear wall (SP1) and steel plate shear wall (TL) specimens

4. MATERIAL TEST RESULTS

Tension tests were conducted on coupons taken from the infill plates of the specimens. Their results are shown in Tables 2 and 3. The cross-section of the sandwich panel used as the infill plate is shown in Figure 7. A steel grade of S275 was used for the frame profiles; S235 grade steel was used for connection plates, infill plates and sandwich panel's steel plates; and grade 10.9 was used for the frame connection bolts. The material characteristics obtained during the coupon test were used in the preparation of the computer models.

Table 2 - Sandwich panel steel plate coupon test results

Specimen No.	**1**	**2**	**3**	**Mean**	**Standard Deviation**
Thickness (mm)	0.50	0.50	0.50	–	–
Width (mm)	25.00	25.00	25.00		
Yield Stress (MPa)	369	334	290	331.0	39.3
Ultimate Stress (MPa)	416	373	416	401.6	24.9

Table 3 - Single steel plate coupon test results

Specimen No.	**4**	**5**	**6**	**Mean**	**Standard Deviation**
Thickness (mm)	1.00	1.00	1.00		
Width (mm)	25.00	25.00	25.00		
Yield Stress (MPa)	349	302	349	333.5	27.2
Ultimate Stress (MPa)	392	430	408	410.1	18.7

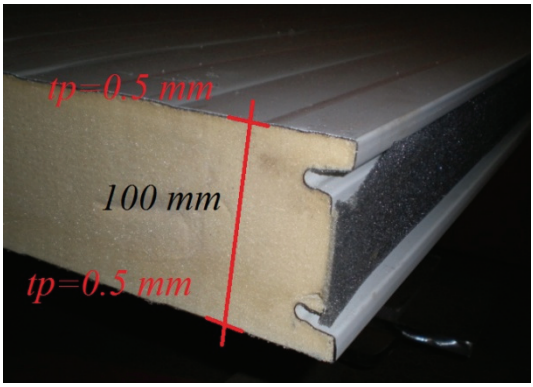

Figure 7 - Sandwich Panel Section

5. ANALYTICAL MODELING

Finite element models of the specimens were prepared using the ABAQUS standard software package [27], and the strip model was prepared using SAP2000 structural analysis software [28]. As the strip model turns into diagonal strips and transfers the load when a lateral load is applied along the plane of each plate, these strips were defined as pin-ended members that could only bear axial tension loads. The angles of inclination of the plates were calculated using the method given in Equation 1, with the plates being defined and analyzed as strip members with an inclination of 46° [8]. The cross-section of each tension strip was defined to be equal to the plate thickness multiplied by the width of the tension field. The computer models were prepared to identify the material qualities and cross-sections of the specimens prior to the experiments, and the obtained experimental results were used to confirm the computer models.

$$\tan^4\alpha = \frac{1 + \frac{t_p L}{2A_c}}{1 + t_p h\left(\frac{1}{A_b} + \frac{h^3}{360 I_c L}\right)} \quad (1)$$

α : Strip inclination angle
t_p : Plate thickness
L : Specimen width
A_c : Column section area
h : Specimen height
A_b : Beam section area
I_c : Column inertia moment

The beam-to-column connection of the bare frame was defined in the strip model and also in the finite element model, where the model parameters were calibrated based on test results. In ABAQUS modeling, structural angles in beam-to-column connections were also modeled

using shell elements and the bolts were defined as fastener elements. At their joining grid, 3 displacement degrees of freedom were defined. In the SAP2000 model, beam-to-column connection regions were modelled according to selected connection type where rotation capacities were calculated from moment capacities and they were defined at the beam end regions. Finally, for the nominally-pinned connection region of the angles, where beams and column elements are connected, their yielding moment capacity was calculated. This value was observed to be around 2.5% of the plastic moment capacity of the beam. The steel plate and sandwich panel shear wall specimens were modeled with the addition of the infill plates. Although the presence of the polyurethane material was not taken into account in the modeling process, the difference in terms of initial stiffness between model and test results clearly showed the contribution of polyurethane material. A total of 11 parallel tension strips were defined in the strip model, with tensile fields measuring 200mm wide, as shown in Figure 8. The graphs obtained following the analysis of the strip model for the steel plate shear wall and the analysis of the bare frame are given in Figure 9. With regards to the frame elements in the finite element model, an S4R shell element was used to define the thin and thick plates, and an S8R5 shell element was used to define thin plates only. The SP1, SP2 and CLA specimens were defined as two-faced 0.5mm steel plates, with 100mm of gap in between. The coupon test material parameters were used in modeling. The first buckling mode obtained via analysis of the finite element model, which is given in Figure 10, and the buckling mode of the same specimen with $+1\delta_y$ displacement during the experiment is given in Figure 11.

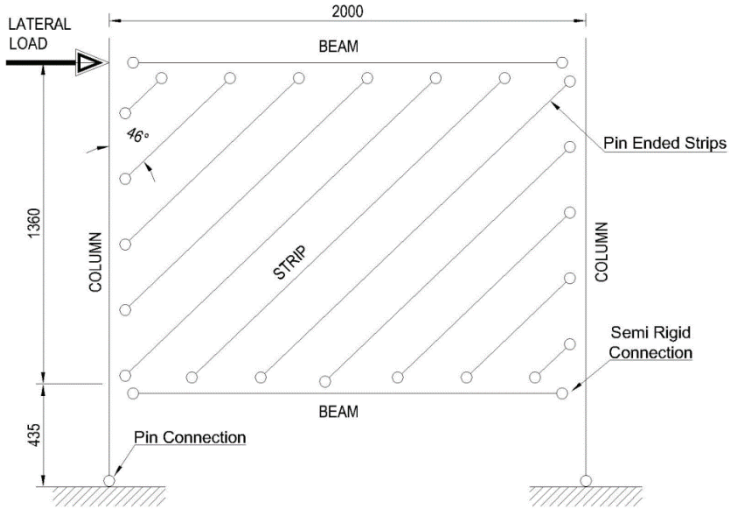

Figure 8 - Strip model of Specimens (all dimensions are in mm)

After the third cycle, the load was observed to decrease with the crushing of the holes within the web region of the beam in the beam-to-column connections. At the stage where yielding of the connections have started after 0.68% drift, the loads continued to increase steadily due to contact of the lower and upper flanges of the beams to the adjoining columns. The model, on the other hand, also predicted a rapid increase in loading as the gap in between is defined on the basis of the size of the experimental specimen.

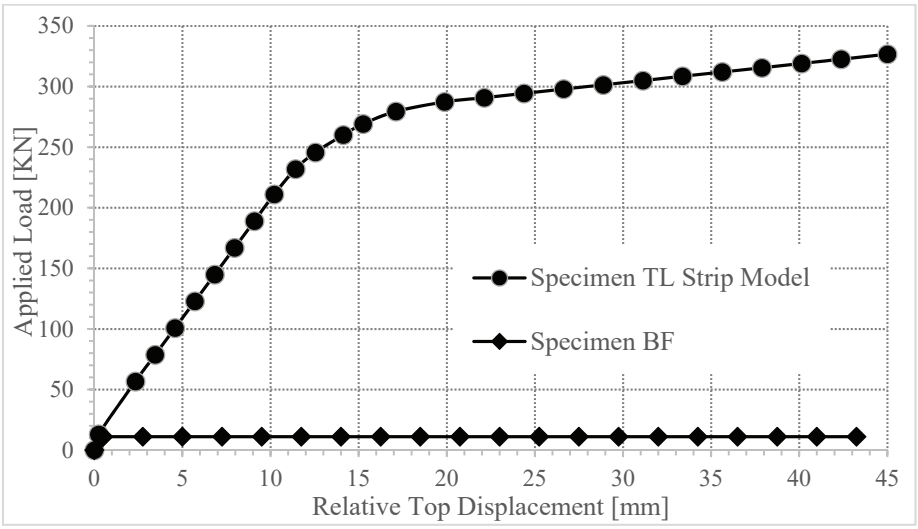

Figure 9 - Steel plate shear wall's strip model and bare frame load displacement curves

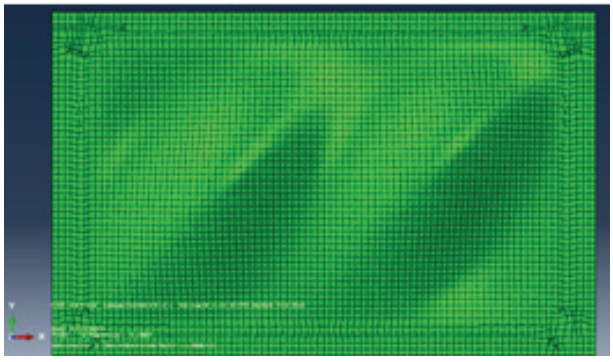

Figure 10 - Finite element model infill plate 1st mode shape

Figure 11 - Specimen TL infill plate at $1\delta_y$ displacement mode shape

The load displacement curves for the bare frame, obtained from experimental loading and FEM analysis are shown in Figure 12. Bare frame models were calibrated using experimental results, and the modeling of the sandwich panel and steel plate shear wall specimens were completed. In ABAQUS, the structural system, including all connections, were modeled using shell elements. Since bolt holes were not defined in the overall model, the section at these regions were reduced to simulate the real sectional dimensions. In the SAP2000 model, the lateral load levels on the bare frame were checked against the experimental results and it was made sure that the surrounding frame system was modelled correctly. Then, according to rotation values obtained at the joint regions, the strip model was prepared. The load-displacement curves obtained FEM analysis are given in Figure 13. The behavior of the specimen that represented the plates on either side of the sandwich panel was very similar to the behavior of the steel plate shear wall specimen.

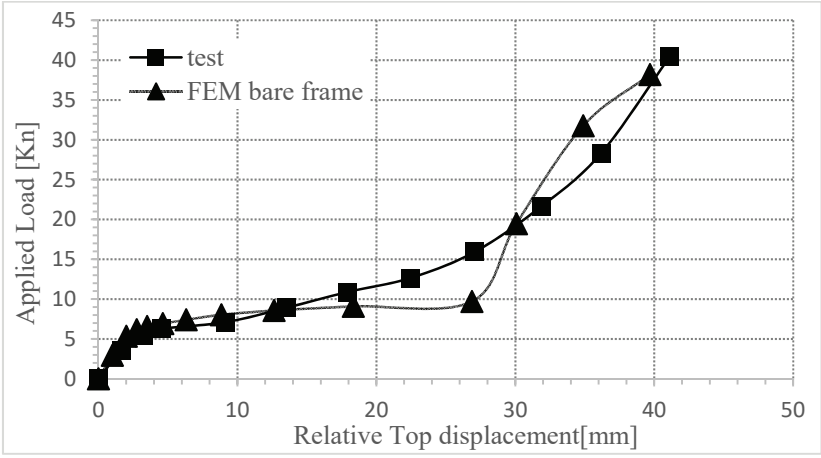

Figure 12 - Bare frame (BF) experimental and finite element analysis load displacement curves

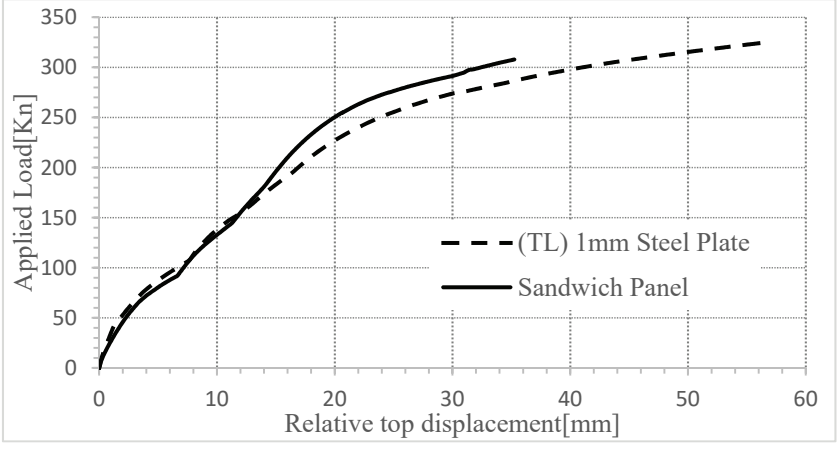

Figure 13 - Steel plate (TL) and sandwich panel shear wall (SP1/SP2) finite element model analysis load displacement curves

6. EXPERIMENTAL RESULTS

The experimental results are presented herein with a discussion of the observations made during the experiments and the obtained data. Quasi-static cyclic loading was applied as per the ATC-24 [29] specifications via 1000kN actuator with a stroke capacity of 150mm push and pull directions. Displacement transducers were placed on the axis of the frame's upper beam, and at the points shown in Figure 14, so that displacements could be measured from desired points for all specimens.

Strain-gauges were mounted at critical sections so that yielding of plates could be monitored. For each plate, 10 strain gauges of 3% elongation capacity were used as shown in Figure 14. Unlike the plates, beams and columns elements were observed to be within the elastic range, as expected. At maximum load levels, strain values ranged between 0.0040 and 0.0080, where yielding started around at a strain level of 0.0015.

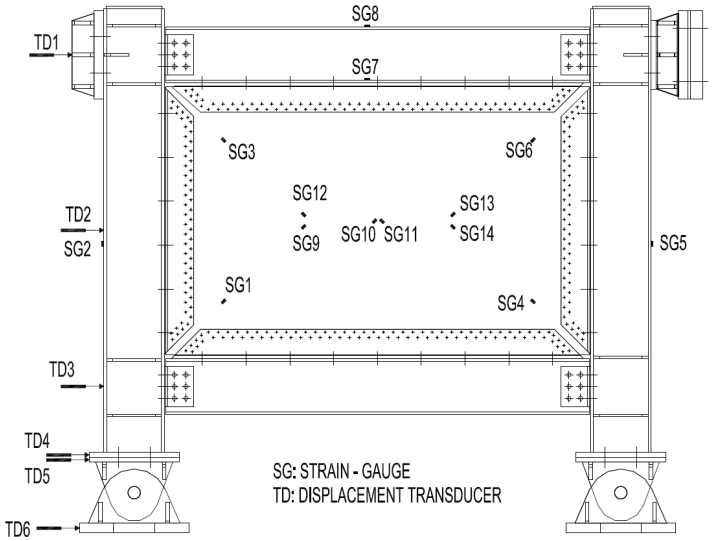

Figure14 - Displacement transducers and strain-gauges arrangement

The displacement transducers placed on beam axes made it possible to determine the storey drifts. A displacement-controlled load was applied prior to and after yielding of the test specimen. The displacement value that corresponding to Q_y, the yielding load of the system, was denoted as δ_y. The cyclic loading steps were increased in multiples of δ_y. 1/3 of the δ_y was applied in the first step, 2/3 of the δ_y was applied in the second step, one δ_y was applied in the third step, and after that, load increased in multiples of δ_y. A total of three cyclic loadings were applied per displacement step, and one cyclic loading for the bare frame. According to the loading protocol, corresponding yield displacements and drifts were obtained and tabulated in Table 4. The load increments, which were described above, were applied to the specimens using a cyclic loading protocol, as shown in Figure 15.

Table 4 - Cyclic displacement histories of specimens

Displacement Steps	Number of Cycles	Cumulative Num. of Cycles	Relative Disp. Ratio to δ_y (Δ/δ_y)	Relative Disp. [mm]	Top Disp. [mm]	Drift (%)
Specimen BF	-	-	-	-	-	-
1	1	1	0.34	1.71	1.95	0.13
2	1	2	0.67	3.29	4.03	0.24
3	1	3	1	4.81	6.02	0.35
4	1	4	2	9.29	12.03	0.68
5	1	5	3	13.74	18.00	1.01
6	1	6	4	17.68	23.46	1.30
7	1	7	5	21.71	28.97	1.60
8	1	8	6	26.13	34.91	1.92
9	1	9	7	30.45	40.84	2.24
Specimen SP1	-	-	-	-	-	-
1	3	3	0.34	1.52	2.17	0.11
2	3	6	0.67	2.66	3.80	0.20
3	3	9	1	4.35	6.22	0.32
4	3	12	2	8.50	12.14	0.62
5	3	15	3	12.61	18.01	0.93
6	3	18	4	16.53	23.62	1.22
7	3	21	5	21.36	30.51	1.57
8	3	24	6	24.83	35.47	1.83
9	3	27	7	28.77	41.10	2.12
10	3	30	8	32.25	46.08	2.37
11	3	33	9	36.88	52.69	2.71
12	2	35	10	42.11	60.16	3.10
Specimen TL	-	-	-	-	-	-
1	3	3	0.34	1.45	1.99	0.11
2	3	6	0.67	2.94	4.03	0.22
3	3	9	1	4.41	6.04	0.32
4	3	12	2	8.78	12.03	0.65
5	3	15	3	13.19	18.07	0.97
6	3	18	4	17.58	24.08	1.29
7	3	21	5	21.99	30.13	1.62
8	3	24	6	26.28	36.00	1.93
9	3	27	7	30.90	42.33	2.27
10	3	30	8	35.15	48.15	2.58
11	3	33	9	39.36	53.92	2.89
12	3	36	10	43.58	59.70	3.20
13	3	39	11	48.07	65.84	3.53
14	3	42	12	53.68	73.54	3.95
15	3	45	13	56.95	78.01	4.19

Note: Cyclic displacement histories of specimens SP2 and CLA are similar to specimen SP1

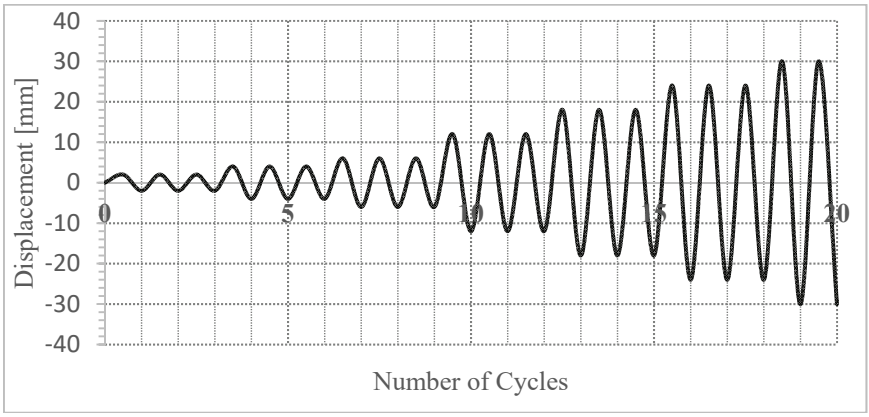

Figure 15 - Cyclic loading in accordance with the ATC 24 (1992) Protocol

6.1. BF Bare Frame Specimen

The cyclic hysteresis curves for the BF bare frame specimen are given in Figure 16, compared with the calibrated curve of the FEM. The frame showed elastic behavior during the first cycle, and plastic behavior started from the second cycle onward, which had a drift of 0.24%. The initial stiffness of the frame was found to be 2.501 kN/mm. When the drift was increased to $\pm 1\delta_y$ (0.35% drift), the cyclical curve covered a wider area than the previous cycles. At 0.68% drift, the beam web in the beam-to-column connections started to deform at bolt holes, giving rise to the yield marks shown in Figure 17.

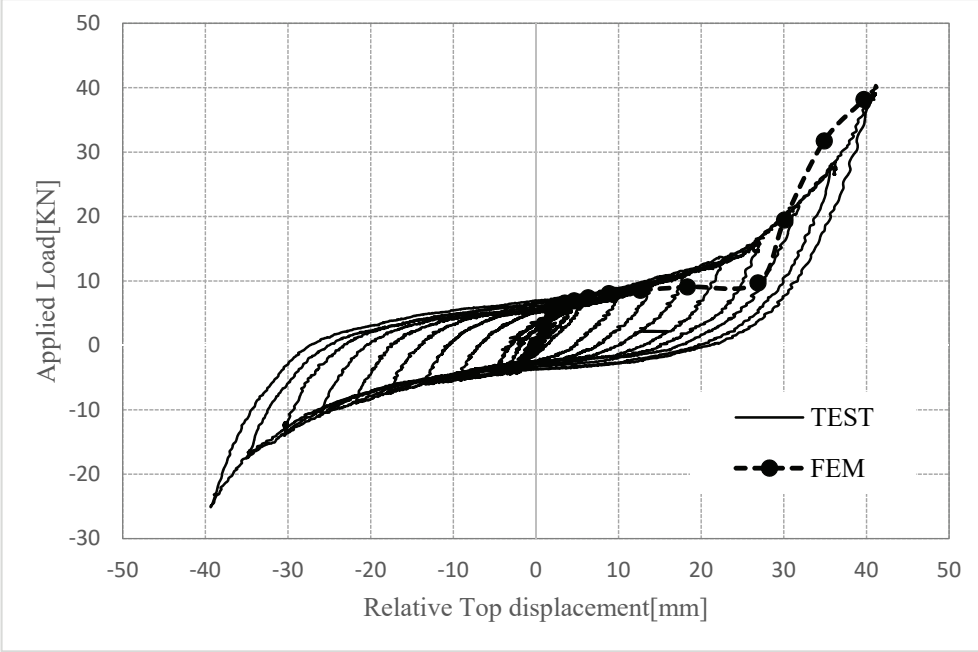

Figure 16 - Hysteresis loops and finite element analysis curve of Specimen BF

From -2δ_y and +3δ_y displacements onward, the beam flanges in the beam-to-column connection started to transfer the moment while in contact with the column, as shown in Figure 18, resulting gradual and significant increase in the force. Figure 19 shows the envelope curves for the first four displacement cycles in the push direction and the first five displacement cycles in the pull direction. With regards to the situation in which the beam flanges did not come into contact with the column, the yield load of the bare frame was measured to be between 10kN to 15kN. After 7δ_y and 2.24% drift level, the connection became fully plastic, but the load continued to increase because of contact. The experiment was ended after identifying the yield load of the connection as 10kN to 15kN. The difference between push and pull load levels at similar displacements are due possible settling of bolts within their tolerance area, and also, small movements along transverse axis despite the rigidly-mounted out-of-plane frame to prevent such movements. No deformation was observed in the specimen other than yielding of the connections.

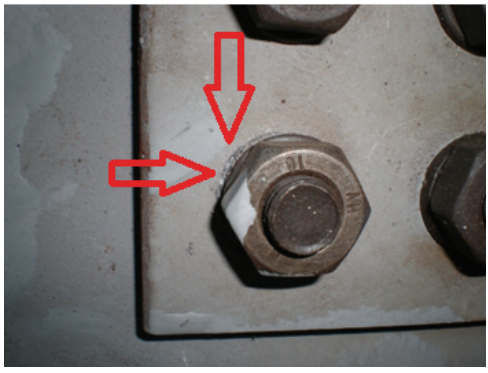

Figure 17 - Crushing of the connection on the web of the beam

Figure 18 - Beam flange in the connection coming into contact with the column

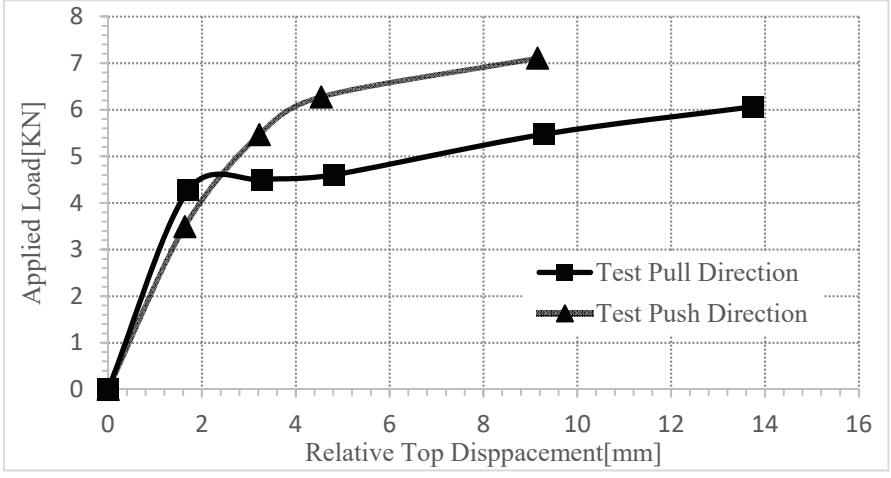

Figure 19 - Load displacement curves showing the effect of the nominally-pinned beam-to-column connection of the bare frame (BF) specimen

6.2. SP1 and SP2 Sandwich Panel Shear Wall Specimens

Specimens SP1 and SP2 had similar characteristics and showed similar behavior. Thus, only the SP1 specimen is discussed in this subsection. The cyclic hysteresis curve of specimen SP1 is given in Figure 20. The specimen displayed an elastic behavior during the first nine cycles, at which point the light corrugated plates of the sandwich panel started flattening and buckling. When the specimen was loaded to $+2\delta_y$ (0.62% drift), the post-elastic behavior was clearly visible on the graph. This drift could be referred to as the yield drift, and a base shear of 152.35kN was measured at this drift level. An approximately 5mm-wide buckling formed on both sides of the plate, in the form of a tension strip. At this point, the steel plates on the front and rear faces of the sandwich panel separated from the polyurethane infill, and became

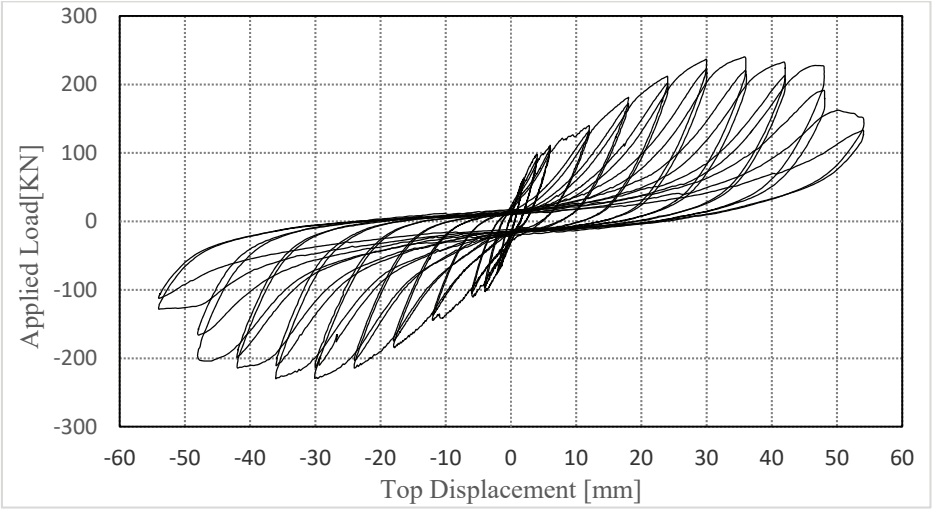

Figure 20 - Hysteresis loops of Specimen SP1

Figure 21 - Overview of the SP1specimen at $+4\delta_y$ displacement step

Figure 22 - SP1 Specimen, Plate was torn and completely separated from panel at $9\delta_y$

two separate steel plates. Buckling was observed during +4δ_y (1.22% drift) as shown in Figure 21, where screw holes of the infill-plate to the fish-plate connection were crushed. During the second cycles of loading, the load was observed to decrease by 5%–15%. For the next four displacement steps, the load values were close to each other, but the buckling wave size increased significantly. During the first cycle at +7δ_y (2.12% drift), a base shear of 249.75kN was measured, representing the highest maximum load value in this experiment. Out-of-plane buckling in the form of a plastic elongation of the plates, exceeded 50mm. At +9δ_y (2.71% drift), the lateral load decreased to 156.30kN, corresponding to 63% of the maximum load. As the connections of the plates were torn apart from their connections and were no longer usable (Figure 22–23), and no more load increment was observed at this point. Thus, the experiment was ended. The experimental specimen displayed a very ductile behavior during all cyclic loading cycles.

(a) (b)

Figure 23 - SP1 Specimen 9δ_y; Plate crushed and torn around the screws at the plate-to-frame connection; (a) front, (b) rear

6.3. Specimen CLA with Two Separate Plates

The cyclic behavior of the specimen is given in Figure 24. As the plates were thin and the polyurethane material was removed, the plate was unable to remain flat prior to loading. As a result, from the first cycles onward, tension fields formed in consequent displacements and the load values were obtained much less than prior test specimens (SP1 and SP2). A lateral load value of 104.61kN was obtained at +2δ_y (0.57% drift), and buckling fields formed on both sides of the plate. Compared to specimen SP1, the polyurethane material in the sandwich panel was observed to create a compression zone within the frame and increased the shear stiffness of the frame, in the first cycles up to +4δ_y. From this point onward, the CLA specimen behaved in a similar manner to the sandwich panel specimen as the polyurethane material in the SP1 specimen was completely crushed. The overview of the specimen at -7δ_y (2.07% drift) is given in Figure 25, showing 20 to 30mm tearing with a close to 45° angle, perpendicular from the screw holes on the lower side of the plate-to-frame connection to the tension field (Figure 26). A maximum lateral load of 263.04kN was obtained during the first cycle at +8δ_y (2.37% drift). At +9δ_y (2.66%), the load remained stable in the push direction, but decreased by 11% in the pull direction, which was compatible with the larger size of the

tearing on the left-hand side of the specimen compared to those on the right-hand side. On the front side, a 60mm-long tearing formed at the plate connections. The out-of-plane buckling wave lengths of the plates exceeded 60mm. In the third cycle of the -10δ_y (2.96% drift), the load decreased to 139.38kN, representing 62% of the previous value, and large deformations were observed on the plates and in plate-to-frame connections, at which point the experiment was ended. Two or three tension fields were formed in the first cycles, but during later cycles, seven more noticeable tension fields were formed. In the last displacement step, the infill plate on the rear was completely torn from the net cross-section area (Figure 27).

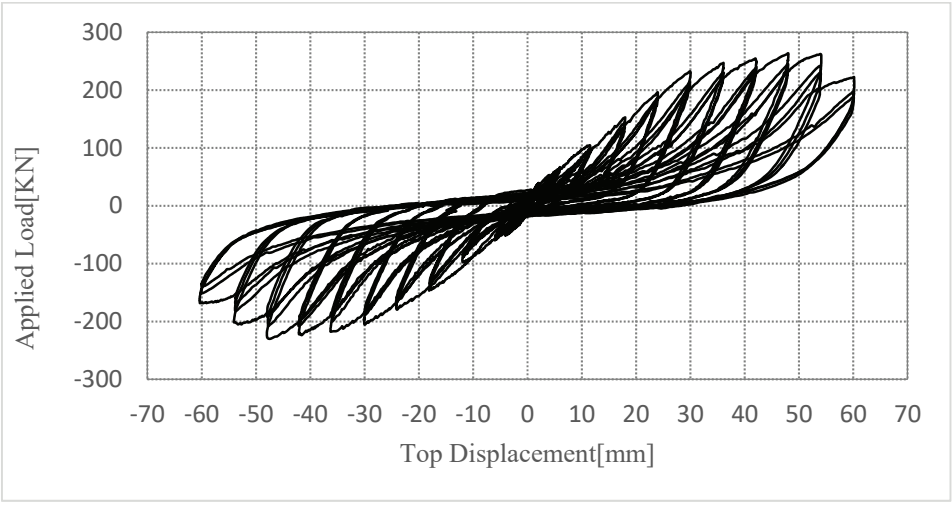

Figure 24 - Hysteresis loops of Specimen CLA

Figure 25 - Overview of the specimen at the -7δ_y(42.00 mm) displacement step.

Figure 26 - $7\delta_y$; front side plate-to-frame connections on the left, torn from the screw edges

Figure 27 - $10\delta_y$; rear side plate-to-frame connections, lower edge, torn from the screw edges

6.4. Specimen TL with a Single Plate

The cyclic behavior of this specimen is given in Figure 28. Since the infill plate was thick, the initial out-of-plane deformation became smaller and the specimen was observed to be more stable under the applied loading. Thus, almost similar load levels were recorded in the push and pull directions. Linear elastic behavior was observed up to $+2\delta_y$ (0.65% drift) and buckling marks with a height of 5mm were formed. At $+5\delta_y$ (1.62% drift), a base shear of 253.19kN was obtained. This value was closer to the maximum load values of the other specimens, and was obtained at a lower displacement value and with an insignificant non-linear deformation.

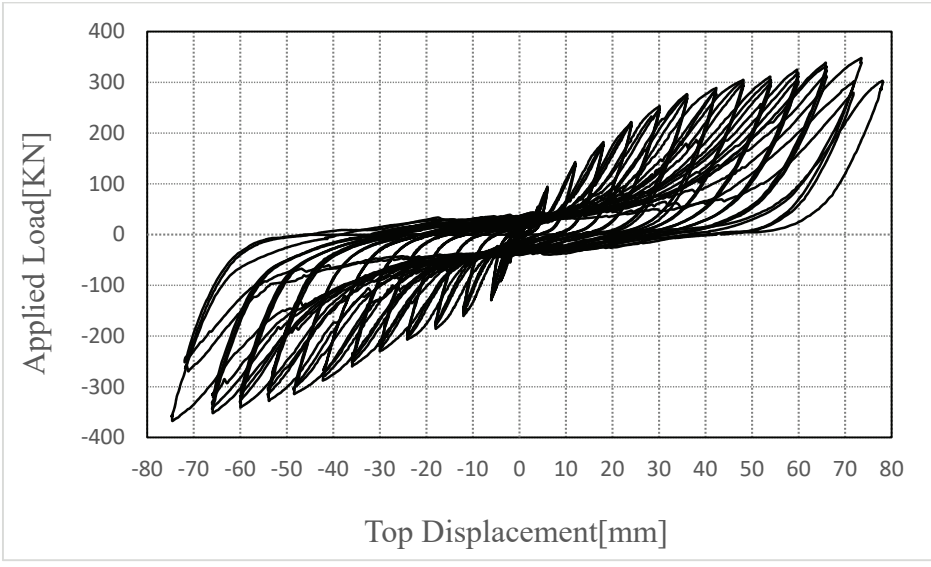

Figure 28 - Hysteresis loops of Specimen TL

During the second cycles of loading, a decrease of 1% to 3% was observed at all steps, followed by a decline close to 5% during the third cycle. This showed that there was less plastic deformation as the plate became thicker. At $+11\delta_y$ (3.53% drift), tearing that formed during the previous displacement level became much larger, forming a 40mm-long tearing with an angle of almost 45°, while the load continued to increase (Figure 29). At $+12\delta_y$ (3.95% drift), base shears of 347.41kN in the push direction, and 367.52kN in the pull direction were recorded, representing the maximum load for this specimen. No tearing were formed in the net area of the plate connection screws, and with the repeated buckling of the plate, the tearing to the corners of the plates with an angle of about 45° reached a length of 150mm (Figure 30). The overview of the specimen in this displacement step, for the pull direction, is given in Figure 31.

Figure 29 - 40 mm tear on the lower left corner of the rear side of Specimen TL, in displacement step $+11\delta_y$(65.84 mm)

Figure - 30 Tears formed to the lower right corner of Specimen TL, on plate-to-frame connections, in the $+13\delta_y$(78.01 mm)

Figure 31 - Overview of the front side of the specimen TL at the $-12\delta_y$(73.54 mm) displacement step.

During the first half cycle of the 43rd cycle, $+13\delta_y$ (4.19% drift), the load value for a half cycle decreased to 302.90kN. The setup to prevent out-of-plane movement of the specimen rubbed against the beam web, preventing loading, and there was a decrease in the pull direction to 68% of the maximum load capacity due to the tearing that formed on the corners. Thus, the experiment was ended at this stage, given the potential danger.

7. COMPARISON OF RESULTS AND DISCUSSION

The load and displacement relationships obtained from the experiments, as well as the maximum load capacity, stiffness and the amount of dissipated energy calculated on the basis of experimental results, were compared to evaluate the relative strengths and weaknesses of the specimens. Comparative load and displacement curves obtained from the experiments are given in Figure 32. Table 5 lists the load values recorded at various drift levels for all specimens. Table 6 presents the ratios of the maximum load values for all specimens to the maximum load values obtained for the bare frame. In addition, the bare frame lost its maximum load capacity from very early values onward and started to act like a pin connection. Table 7 was created to allow a comparison with Specimen SP2, which had the lowest maximum load capacity. This shows that the maximum load capacity of the single-plate specimen TL is about 45% higher than the other specimens of thin plates with two sides, whereas sandwich panels, with appropriate connections, resulted a very high lateral load resisting capacity compared to the bare frame, and it can therefore be used as an efficient lateral load resisting system.

Table 5 - Load Values Classified by Drift (kN)

Drift [%]	BF	SP1	CLA	TL	SP2
0.25	4.51	116.04	60.37	67.02	107.78
0.50	4.99	142.72	95.41	118.89	131.58
0.75	5.59	164.57	132.00	153.09	161.68
1.00	6.05	189.84	168.98	185.64	192.12
1.25	7.23	215.98	204.28	215.66	216.61
1.50	8.53	234.57	233.55	241.48	236.95
1.75	9.99	238.08	245.24	263.10	239.59
2.00	11.79	244.82	252.69	279.06	240.02
2.25	14.26	245.74	259.72	287.75	-
2.50	-	-	262.68	300.27	-
3.00	-	-	-	315.65	-
3.50	-	-	-	337.21	-
4.00	-	-	-	344.67	-

The initial stiffness values of the test specimens were calculated from the pre-yield points of the cyclic graph envelope curves recorded during loading. To examine the effect of adding an infill plate, and the use of different types of infill plates, Table 8 shows the mean stiffness values for the push and pull directions, and compares their ratios to the stiffness value of the bare frame specimen.

Table 6 - Maximum load capacities of specimens in the push direction, and their ratios to the bare frame

Test No.	Specimen Mark	Maximum Load [kN]	Ratio Definition	Ratio
1	BF	8.89	BF/BF	1.0
2	SP1	249.75	SP1/BF	28.1
3	CLA	263.04	CLA/BF	29.6
4	TL	347.42	TL/BF	39.1
5	SP2	240.22	SP2/BF	27.0

Table 7 - Comparison of the Maximum Load Capacities of the Steel Plate Shear Walls

Test No.	Specimen Mark	Maximum Load [kN]	Ratio Definition	Ratio
2	SP1	249.75	SP1/SP2	1.04
3	CLA	263.04	CLA/SP2	1.10
4	TL	347.42	TL/SP2	1.45
5	SP2	240.22	SP2/SP2	1.00

Table 8 - Comparing Stiffness Values of the Experimental Specimens

Test No.	Specimen Mark	Initial Stiffness[KN/mm]	Ratio Definition	Ratio
1	BF	2.32	BF/BF	1.00
2	SP1	48.76	SP1/BF	21.02
3	CLA	27.91	CLA/BF	12.03
4	TL	32.59	TL/BF	14.05
5	SP2	52.40	SP2/BF	22.59

Specimens SP1 and SP2 had significantly higher initial stiffness values than the other specimens. As the steel plates on both sides of the 100mm-thick sandwich panel turned into tension strips and the polyurethane material between 0.5mm thin steel plates was compressed and started to act as a compression zone, an increase in stiffness was observed in the first cycles. The sandwich panel specimens were observed to have average stiffness values that were 65% higher than those of other steel plate shear wall specimens. The infill plate contributed to stiffness in all specimens, while the use of sandwich panels provides additional initial stiffness, resulting in behavior similar to the composite plate shear walls during early

cycles. The steel plate shear wall and sandwich panel shear wall specimens had initial stiffness values that are 12 to 22 times, respectively, that of the initial stiffness of the bare frame with nominally-pinned beam-to-column connections. Even though two-sided specimens had the same total plate thickness, crushing and tearing of cross-sections were observed around the infill plate-to-fish plate connection holes of the thin plates with smaller displacements. Until the end of the experiment, no net cross-section area tearing was formed around the screw holes of the single-plate specimen TL, which had a thickness of 1.0mm, matching the total thickness of the plates on both sides of the sandwich panel. The yielding of the plates took the form of tearing to the plate corners as a result of repeated loading. This difference between the two-sided specimen and the single-plate specimen, with matching total plate thicknesses, could be attributed to the lack of uniform distribution of the load in practice, even though in theory the load should have been distributed equally.

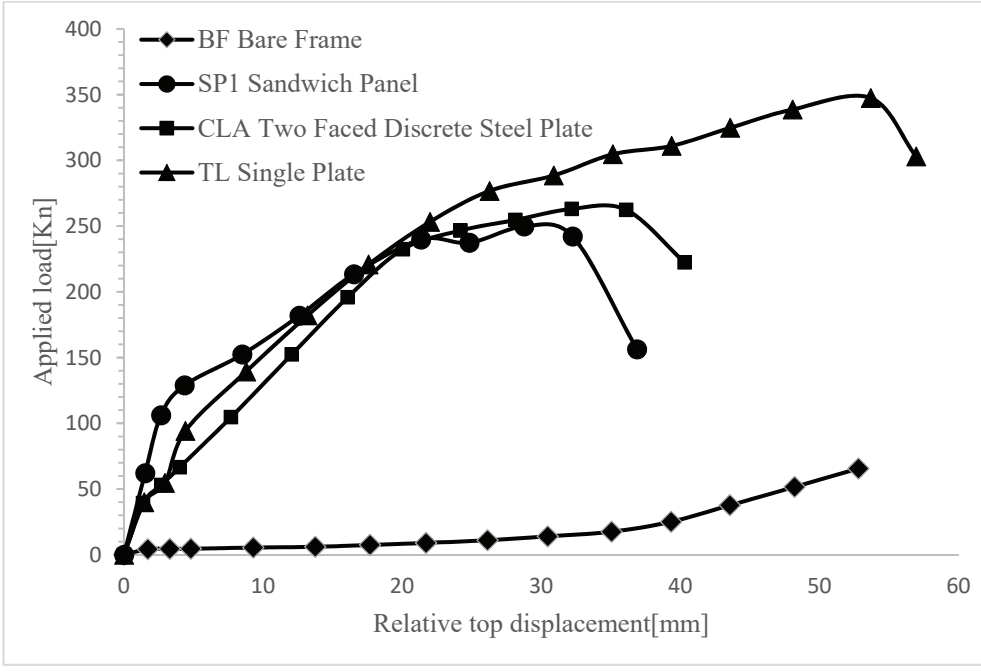

Figure 32 - Comparing the experimental load-displacement curves of specimens

Energy dissipation amounts were used to compare and evaluate the test results. Dissipated energy was calculated as the area encompassed by the load displacement curve for every cycle. At 2.5% drift, Specimen SP1 dissipated an energy 15 times more than that of the bare frame, while Specimen CLA dissipated 18 times more energy and Specimen TL dissipated 19 times more energy. Based on drift ratios of each specimen, the cumulative energy amounts summed up over the first cycles are given in Figure 33. This shows that the sandwich panel used as an infill wall inside the frame dissipated a very high amount of energy, approximating the behavior of the steel plate shear wall specimen, and by simply making an appropriate connection, this method could turn the frame, with little additional cost, into a worthy lateral load resisting system. The sandwich panel shear wall that was designed by attaching the steel

plates on both sides of the sandwich panel to the frame using screws was observed to display ductile behavior under cyclic loading, similar to the steel plate shear wall with a single plate. When the plate yields, it can be removed from the connecting structural elements and new infill plates can be installed easily, as shown in Figure 34. At the end of the test, round bolt holes took the shape of elliptical indicating ductile behavior. No excessive visible damage such as shearing or bending of bolts were observed. It is noteworthy to say that in case there is a need for replacement of panels, the angles should be removed and replaced with the new ones. The orientation angle of the tension field was observed to be 49° in the sandwich panel specimens and 47° in the single-plate specimen, and was calculated to be 46° using Equation 1.

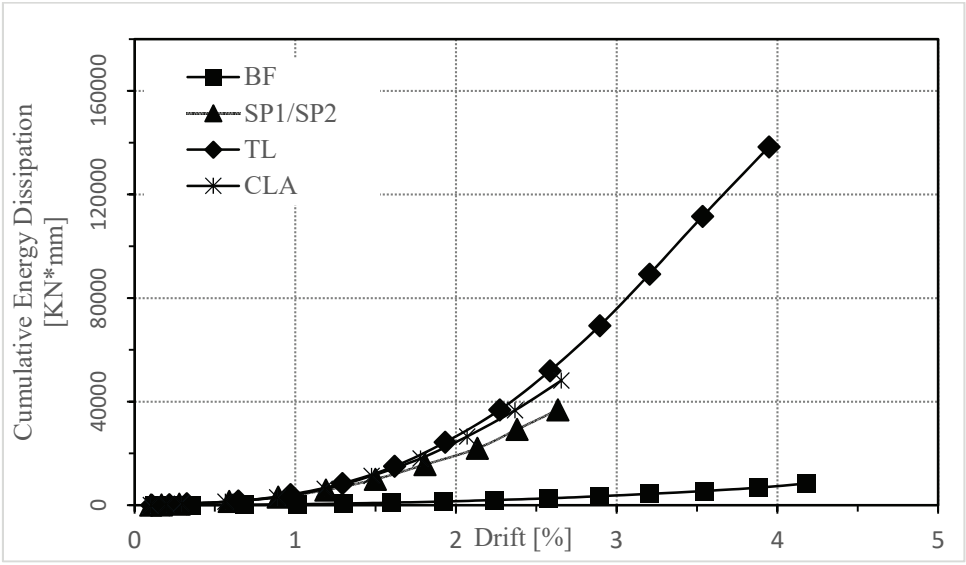

Figure 33 – Comparison of the cumulative energy amounts dissipated

Figure 34 - When the plate yields, removing infill plates from the connecting structural elements can be easily performed

8. CONCLUSIONS

This study aimed to increase the strength, stiffness and energy dissipation capacity of a bare frames by attaching sandwich panels used as partition walls with an appropriate connection design, and thus making them behave similar to steel plate shear walls. To this end, a bare frame specimen, two sandwich panel specimens, a specimen with the polyurethane material removed from sandwich panel, and a single-plate specimen of matching thickness were prepared. Quasi-static loads were applied following ATC 24 [29] guidelines.

To be able to observe the effect of the infill plate clearly, a nominally-pinned beam-to-column connection was preferred, in which the beam web is attached to the column with two angle brackets, which are used frequently in design of steel constructions. A nominally-pinned connection was preferred in order to focus on the behavior of the infill plates only.

The polyurethane material inside the steel plates in the form of sandwich panel behaved like a compression zone, resulting in a significant increase in stiffness in the first cycles, when compared to the other specimens. Also compared to the other specimens, the polyurethane material absorbs the buckling sound of the steel plates during the first cycles.

In order to achieve a ductile behavior, the aim was to make the plate yield, rather than tearing it at the connection region to the frame. The reason why single plate (1.00mm) specimen's load and energy dissipation capacities were higher, compared to the two-faced (0.5mm + 0.5mm) plate specimen, was its thickness. While the SP1, SP2 and CLA specimens yielded or formed a mechanism due to tearing of plate around the screw connection region, the TL specimen dissipated energy under cyclic loading until the yielding load was attained.

The experimental results showed that a sandwich panel used as a partition wall inside a frame is able to dissipate a very high amount of energy, approximating the behavior of a steel plate shear wall specimen, contributing significantly to lateral load resistance and stiffness values, as long as it is attached to the frame with an appropriate connection design on both sides. This method can turn partition walls into a sound lateral load resisting system, with little additional cost. In addition, the light corrugated plate structure of the sandwich panels increases ductility.

The angles attaching the plate to the frame with bolts can be removed after significant damage after an earthquake. It is possible to conduct analyses using a strip model, as similar tension field formations were observed in both the steel plate and the sandwich panel shear wall specimens; however, further study is needed on the methods of analysis that would take the contribution of the polyurethane material into account.

Finally, specimens SP1 and SP2 were observed to be less effective than specimen TL, especially in terms of their dissipated energies.

Acknowledgements

The authors would like to thank to the staff of Boğazici University's Structural and Materials laboratories, where the experimental study was conducted. Also, special thanks go to Arcelor Mittal RZK for donating all the steel sections and Cağla Engineering for constructing specimens for the experimental study. Finally, authors would like to thank to Sakarya University Scientific Research Projects Unit for its financial support with the Project Number 2007-50-02-022.

References

[1] Mimura, H. and Akiyama, H. (1977). "Load-deflection relationship of earthquake resistant steel shear walls with a developed diagonal tension field." Trans., Arch. Inst. Of Japan, Tokyo, Japan, 109-114.

[2] Agelidis, N. and Mansell, D. S. (1982). "Seismic steel plate cores in tall buildings." Civil Engineering Transactions of the Institution of Engineers, Australia, CE24 (1), 11-18.

[3] Rezai, M. (1999). "Seismic behavior of steel plate shear walls by shake table testing." PhD Thesis, University of British Columbia, Vancouver, Canada.

[4] Yamada, M. (1992). "Steel panel encased R.C. composite shear walls." Proceedings of the ASCE Engineering Foundation Conference on Composite Construction in Steel and Concrete II, pp. 899-912.

[5] Caccese, V., Elgaaly, M. and Chen, R. (1993). "Experimental study of thin steel-plate shear walls under cyclic loading." Journal of Structural Engineering, 119, 0573-0587.

[6] Sabouri-Ghomi, S. and Roberts, T. M. (1991). "Nonlinear dynamic analysis of thin steel plate shear walls." Computers & Structures, 39, 121-127.

[7] Takahashi, Y., Takemoto, Y., Takeda, T. and Takagi, M. (1973). "Experimental study on thin steel shear walls and particular bracings under alternative horizontal load." IABSE Symposium, On Resistance and Ultimate Deformability of Structure Acted on by Well-Defined Repeated Loads, Lisbon, Portugal, 185-191.

[8] Timler, P. A. and Kulak, G. L. (1983). "Experimental study of steel plate shear walls." Structural Engineering Report, 114, University of Alberta, Edmonton, Alta, Canada.

[9] Tromposch, E. W. and Kulak, G. L. (1987). "Cyclic and static behavior of thin panel steel plate shear walls." Structural Engineering Report, 145, University of Alberta, Edmonton, Alta, Canada.

[10] Driver, R. (1997). "Seismic behavior of steel plate shear walls." PhD Thesis, University of Alberta, Edmonton, Canada.

[11] Behbahanifard, M. R. (2003). "Cyclic behavior of unstiffened steel plate shear walls." PhD Thesis, University of Alberta, Edmonton, Canada.

[12] Alinia, M.M. and Shirazi, R.S. (2009), "On the design of stiffeners in steel plate shear walls." Journal of Constructional Steel Research 65 (2009) 2069-2077.

[13] Xue, M. and Lu, L. W. (1994). "Interaction of infilled steel shear wall panels with surrounding frame members." Proc. Struct. Stability Res. Council Annu. Tech. Session, Bethlehem, Pa., 339-354.

[14] Purba, R. and Bruneau, M. (2015), "Experimental investigation of steel plate shear walls with in-span plastification along horizontal boundary elements." Engineering Structures, 97, 68–79.

[15] Formisano, A. and Lombardi, L. (2018). "Low yield metals and perforated steel shear walls for seismic protection of existing RC buildings." Cogent Engineering, 5(1), 1525813.

[16] Alavi, E. and Nateghi, F. (2013), "Experimental study on diagonally stiffened steel plate shear walls with central perforation." Journal of Constructional Steel Research 89, 9–20.

[17] Eom, T., Park, H., Lee, C., Kim, J. and Chang, I. (2009), "Behavior of Double Skin Composite Wall Subjected to In-Plane Cyclic Loading." Journal of Structural Engineering, 1239-1249.

[18] Aoyama, H. and Yamamoto, Y. (1984), "Aseismic strengthening of existing RC buildings by steel panel shear walls with rims." Transactions of the Japan Concrete Institute, 6: 733-740.

[19] Astaneh-Asl, A. and Zhao, Q. (2002). "Cyclic behavior of shear wall systems." Proceedings, Annual Stability Conference, Structural Stability Research Council, April, Seattle.

[20] Berman, J., Celik, O. C. and Bruneau, M. (2005). "Comparing hysteretic behavior of light-gauge steel plate shear walls and braced frames." Engineering Structures, 27, 475-485.

[21] Dey, S., Bhowmick, A.K. (2016), "Seismic performance of composite plate shear walls." Structures 6, 59–72.

[22] Vatansever, C. (2008). "Cyclic behavior of thin steel plate shear walls with semi-rigid beam-to-column connections." PhD Thesis, Istanbul Technical University, Institute of Science, Istanbul, Turkiye.

[23] Choi, I. and Park, H. (2009), "Steel plate shear walls with various ınfill plate designs." Journal of Structural Engineering, 0733-9445(2009)135:7(785).

[24] Vatansever, C. and Yardimci, N. (2011), "Experimental investigation of thin steel plate shear walls with different infill-to-boundary frame connections." Steel and Composite Structures, Vol. 11, No. 3, 251-271.

[25] Berman, J. and Bruneau, M. (2005). "Experimental investigation of light-gauge steel plate shear walls." Journal of Structural Engineering, 131 (2), 259-267.

[26] Vatansever C. and Berman J.W., (2015), "Analytical investigation of thin steel plate shear walls with screwed infill plate." Steel and Composite Structures, 19 (5), 1145-1165.

[27] Hibbit, Karlsson, Sorenson, Inc., (HKS), "ABAQUS/Standard Theory Manual." Student Edition 6.13. Pawtucket, R.I.

[28] SAP2000, "Structural Analysis Program, Computers and Structures." Inc., Berkeley, California, USA.

[29] ATC-24, (1992). "Guidelines for cyclic seismic testing of components of steel structures." Applied Technology Council, California.

TEKNİK DERGİ MANUSCRIPT DRAFTING RULES

1. The whole manuscript (text, charts, equations, drawings etc.) should be arranged in Word and submitted in ready to print format. The article should be typed on A4 (210 x 297 mm) size paper using 10 pt (main title 15 pt) Times New Roman font, single spacing. Margins should be 40 mm on the left and right sides and 52.5 mm at the top and bottom of the page.
2. Including drawings and tables, articles should not exceed 25 pages, technical notes 6 pages.
3. Your contributed manuscript must be sent over the DergiPark system. (http://dergipark.gov.tr/tekderg)
4. The text must be written in a clear and understandable language, conform to the grammar rules. Third singular person and passive tense must be used, and no inverted sentences should be contained.
5. Title must be short (10 words maximum) and clear, and reflect the content of the paper.
6. Sections should be arranged as: (i) abstract and keywords, (ii) title, abstract and keywords in the other language, (iii) main text, (iv) symbols, (v) acknowledgements (if required) and (vi) references.
7. Both abstracts should briefly describe the object, scope, method and conclusions of the work and should not exceed 100 words. If necessary, abstracts may be re-written without consulting the author. At least three keywords must be given. Titles, abstracts and keywords must be fitted in the first page leaving ten line space at the bottom of the first page and the main text must start in the second page.
8. Section and sub-section titles must be numbered complying with the standard TS1212.
9. Symbols must conform to the international rules; each symbol must be defined where it appears first, additionally, a list of symbols must be given in alphabetic order (first Latin, then Greek alphabets) at the end of the text (before References).
10. Equations must be numbered and these numbers must be shown in brackets at the end of the line.
11. Tables, drawings and photographs must be placed inside the text, each one should have a number and title and titles should be written above the tables and below the drawings and photographs.
12. Only SI units must be used in the manuscripts.
13. Quotes must be given in inverted commas and the source must be indicated with a reference number.
14. Acknowledgement must be short and mention the people/ institutions contributed or assisted the study.
15. References must be numbered (in brackets) in the text referring to the reference list arranged in the order of appearance in the text. References must include the following information:

    If the reference is an article: Author's surname, his/her initials, other authors, full title of the article, name of the journal, volume, issue, starting and ending pages, year of publication.

    Example : Naghdi, P. M., Kalnins, A., On Vibrations of Elastic Spherical Shells. J. Appl. Mech., 29, 65-72, 1962.

    If the reference is a book: Author's surname, his/her initials, other authors, title of the book, volume number, editor if available, place of publication, year of publication.

    Example : Kraus. H., Thin Elastic Shells, New York. Wiley, 1967.

    If the reference is a conference paper: Author's surname, his/her initials, other authors, title of the paper, title of the conference, location and year.

    If the source is a thesis: Author's surname, his/her initials, thesis title, level, university, year.

    If the source is a report: Author's surname, his/her initials, other authors, title of the report, type, number, institution it is submitted to, publication place, year.
16. Discussions to an article published in Teknik Dergi should not exceed two pages, must briefly express the addressed points, must criticize the content, not the author and must be written in a polite language. Authors' closing remarks must also follow the above rules.
17. A separate note should accompany the manuscript. The note should include, (i) authors' names, business and home addresses and phone numbers, (ii) brief resumes of the authors and (iii) a statement "I declare in honesty that this article is the product of a genuinely original study and that a similar version of the article has not been previously published anywhere else" signed by all authors.
18. Copyright has to be transferred to UCTEA Turkish Chamber of Civil Engineers. The standard copyright form signed by the authorised author should therefore be submitted together with the manuscript.

CONTENTS

ISSN: 1300-3453